Ultrafast Dynamics of Biologically Active Chromophores and their Building Blocks in Aqueous Solution

Kate Robertson

A dissertation submitted in partial fulfillment

of the requirements for the degree of

Doctor of Philosophy

of

University College London.

Department of Chemistry

University College London

October 10, 2024

I, Kate Robertson, confirm that the work presented in this thesis is my own. Where information has been derived from other sources, I confirm that this has been indicated in the work.

Abstract

Understanding photochemical dynamics of biomolecules and their building blocks in aqueous environments is crucial for advancing our comprehension of biological processes such as photooxidation and luminescence. This understanding is essential not only for unraveling fundamental mechanisms but also for the rational design of new biotechnologies. This thesis presents studies of the excited state dynamics of molecules relevant to biology, providing insights that could aid fundamental understanding and practical applications. The first results are presented in Chapter 3 which presents an investigation of the photooxidation dynamics of phenolate, a molecular motif found in many biochromophores. Photooxidation is integral to a range of biological processes, such as the photocycle of photoactive proteins, yet the mechanism of electron emission in phenolate, had been disputed. The work described in Chapter 3 combined femtosecond transient absorption spectroscopy (TAS), with liquid-microjet photoelectron spectroscopy and high-level quantum chemistry calculations to unravel the wavelength dependant photooxidation dynamics of phenolate. Then, Chapter 4 presents a study of methyl substituted phenolates. TAS was combined with time-correlated single photon counting (TCSPC) experiments and high-level quantum chemistry calculations to understand the implications of systematic modifications to phenolate by substitution on the photooxidation mechanism. Chapter 5, then presents the first time-resolved photoelectron spectroscopy (TRPES) data recorded on the UCL liquid microjet spectrometer. This study focuses on aqueous phenolate following $1 + 1$ resonance-enhanced photodetachment. The behavior observed in these experiments was compared to the corresponding transient absorption data from Chapter 3 and and our preliminary results

hint at faster electronic relaxation dynamics for molecules near a water-vacuum interface compared to those in bulk water. Finally, Chapter 6 presents an investigation of the photoluminescence dynamics of the small molecule that lies at the heart of firefly bioluminescent (oxyluciferin). This work focused on two model bioluminescent emitters, oxyluciferin and infraoxyluciferin, studying their excited state dynamics using TAS to understand why infraluciferin is a less efficient emitter than oxyluciferin. Infraoxyluciferin is an analogue of oxyluciferin with a red-shifted emission. Bioluminescent probes have applications in *in vivo* imaging in medicine. To design new bioluminescent probes for deeper tissue imaging, the emission maximum of these molecules needs to be red-shifted further and made brighter. By improving our detailed understanding of the electronic relaxation of the molecular unit central to firefly bioluminescence and comparing it to the less efficient but red-shifted infraoxyluciferin, we aim to design new, more efficient tools for bioluminescent imaging.

Impact Statement

Chromophores are small, essential molecules found at the heart of photoactive proteins. They play a vital role in nature, and upon absorbing ultraviolet (UV) light, they can transfer this energy into a physical response. These biologically relevant molecules are of great interest due to their applications in bioimaging of cells and as photovoltaic materials. The environment of the chromophore plays an essential role in the biological response, as the surrounding photoactive protein amplifies the structural changes of the chromophore after the absorption of UV light. The intricate interactions between the chromophore and the protein are essential for driving these biological processes. The study of chromophores and their building blocks is essential for understanding their photostability and for aiding in the design of new systems that could have applications in bioimaging. Conducting these studies in aqueous solutions is crucial because water is the primary medium in which biological processes occur, thus mimicking their natural environment. Additionally, studying chromophores in water can reveal how solvation impacts their electronic structure and dynamics. The work presented in this thesis contributes to the study of the dynamics of phenolate, substituted phenolates, and model bioluminescent emitters, all in aqueous solution. Most of the work described focuses on using transient absorption spectroscopy (TAS) to unravel the excited state dynamics of the three systems mentioned, contributing to fundamental understanding while also aiding efforts to design new bioluminescent probes for *in vivo* imaging in medicine. One chapter describes the development of the capability for using time-resolved liquid-jet photoelectron spectroscopy, a complementary spectroscopic technique, and its application in the study of the dynamics of phenolate in aqueous solution. The

results are compared with those obtained from TAS experiments, aiming to understand the differences observed between dynamics in bulk solution and those closer to the surface. The study contributes to a more fundamental understanding of how chromophores behave in different environments.

Acknowledgements

First, I would like to thank my supervisor, Prof. Helen Fielding, for her support and guidance over the past three years. Thank you for all the encouragement and for helping me grow in confidence during my time at UCL. I have thoroughly enjoyed being a member of your group, and I could not have asked for a better supervisor. I would also like to thank you for all the effort you put in to reading the draft of this thesis and providing timely and helpful feedback. Next, I would like to thank the past and present members of the Fielding group. I've had the privilege of working with many wonderful scientists and have made some amazing friends along the way. Thank you, Dr. Johanna Rademacher, for reading chapters of this thesis, providing valuable feedback, and engaging in helpful discussions during the writing process. I also appreciate all the late evenings and weekends you spent in the lab helping me record data. Thank you, Edoardo Simonetti, for your invaluable assistance in the lab and for staying late to help me collect data. All your help has been greatly appreciated, and I thoroughly enjoyed working on the liquid-jet with you. Thank you, Sufiyan Khan, for reading a chapter of this thesis and providing very helpful feedback, as well as for your all your assistance in the lab. I would also like to thank you for all the weekends you kindly came in to help me. I would like to again thank Johanna, Edoardo, and Sufiyan for being such supportive and wonderful friends. I would also like to thank Dr. David Bacon for all his help in the lab and for assisting me in getting my experiments to work. Thank you to Dr. Rhea Kumar for sharing your expertise and knowledge. I will always be grateful for everything you taught me. I would also like to thank William Fortune, Dr. Joseph Broughton, Dr. Omri Tau, and Dr. Michael Scholz for all your help and guidance when I first started my

PhD. I would also like to thank my wonderful friends and family, especially Mum and Dad, for all your support and encouragement. Finally, I want to thank Ross for your love, support, and encouragement.

Declaration

UCL Research Paper Declaration Form: referencing the doctoral candidate's own published work(s)

1. **For a research manuscript that has already been published** (if not yet published, please skip to section 2)**:**

   (a) **What is the title of the manuscript?** Wavelength Dependant Mechanism of Phenolate Photooxidation

   (b) **Please include a link to or doi for the work:** DOI https://doi.org/10.1039/D3SC00016H

   (c) **Where was the work published?** Chemical Science

   (d) **Who published the work?** Royal Society of Chemistry

   (e) **When was the work published?** 20/02/2023

   (f) **List the manuscript's authors in the order they appear on the publication:** Kate Robertson, William G. Fortune, Julia A. Davies, Anton N. Boichenko, Michael S. Scholz, Omri Tau, Anastasia V. Bochenkova, and Helen H. Fielding

   (g) **Was the work peer reviewd?** Yes

   (h) **Have you retained the copyright?** Yes

   (i) **Was an earlier form of the manuscript uploaded to a preprint server (e.g. medRxiv)? If 'Yes', please give a link or doi** No
   If 'No', please seek permission from the relevant publisher and check the box next to the below statement:

☒ *I acknowledge permission of the publisher named under 1d to include in this thesis portions of the publication named as included in 1c.*

2. **For a research manuscript prepared for publication but that has not yet been published** (if already published, please skip to section 3)**:**

   (a) **What is the current title of the manuscript?**

   (b) **Has the manuscript been uploaded to a preprint server 'e.g. medRxiv'?**
   If 'Yes', please please give a link or doi:

   (c) **Where is the work intended to be published?**

   (d) **List the manuscript's authors in the intended authorship order:**

   (e) **Stage of publication:**

3. **For multi-authored work, please give a statement of contribution covering all authors** (if single-author, please skip to section 4)**:** The project was conceived and supervised by Helen Fielding The TAS data were recorded by Julia Davies, with assistance from Kate Robertson, and processed, analysed and interpreted by Kate Robertson, with contributions from Julia Davies and Michael Scholz. The PES data were recorded by William Fortune, with assistance from Omri Tau., and processed, analysed and interpreted by Willaim Fortune, with assistance from Michael Scholz. Calculations were undertaken and interpreted by Anton Boichenko and Anastasia Bochenkova. The manuscript was written by Kate Robertson and Helen Fielding with contributions from Anastasia Bochenkova, William Fortune, Michael Scholz and Julia Davies. All authors read and approved the final version of the manuscript.

4. **In which chapter(s) of your thesis can this material be found?** Chapter 3 and 4

e-Signatures confirming that the information above is accurate (this form should be co-signed by the supervisor/ senior author unless this is not appropriate,

e.g. if the paper was a single-author work)**:**

Candidate:

Date: 06/09/2024

Supervisor/Senior Author signature (where appropriate)**:**

Date: 06/09/2024

Contents

Chapter 1

Introduction

1.1 Motivation

Chromophores are molecules found in nature that efficiently convert photon energy into physical responses, and they play a crucial role in several well-known processes such as photosynthesis, vitamin D production, and vision [1–5]. A chromophore is a small molecule central to photoactive proteins. In response to photon absorption, the chromophore undergoes subtle structural changes, which are then amplified by the surrounding protein. This process is crucial in various biological functions. For instance, retinal, the chromophore in the rhodopsin protein, plays a key role in vision by initiating the phototransduction cascade. Similarly, *para*-coumaric acid, the chromophore at the core of the photoactive yellow protein, is responsible for negative phototaxis in plants, guiding their movement away from light sources [6, 7]. These examples highlight the intricate interplay between chromophores and their protein environments in driving essential biological processes. The work presented in this thesis focuses on the photodynamics of phenolate and oxyluciferin. The first system phenolate, is a common molecular motif found in several biologically significant molecules, including the photoactive yellow protein, the green fluorescent protein, and tyrosine [8–12]. The second system oxyluciferin, is the molecule that lies at the heart of firefly bioluminescence. Bioluminescence, the phenomenon where living organisms produce visible light from chemical energy, is particularly notable for its high quantum yield ($\Phi = 0.41$) [13]. This high quantum yield makes

bioluminescent imaging advantageous over other techniques, as it does not require an external light source, thereby eliminating background counts and resulting in a much higher signal-to-noise ratio. To investigate the dynamics of these biologically relevant systems in the condensed phase, two complementary experimental techniques have been employed: transient absorption spectroscopy (TAS) and liquid microjet photoelectron spectroscopy (LJ-PES).

1.2 Photophysics of Organic Anions

To understand the photophysics of an organic anion we must explore how the molecule interacts with light, specifically ultraviolet (UV) radiation for the molecular systems that are the focus of the work described in this thesis. In simple terms, the molecule will be promoted from its ground electronic singlet state (S_0), *via* the absorption of a photon, to a higher lying singlet state (S_n). Following photoexcitation, the nuclei may no longer be in their equilibrium positions and will therefore move. In the excited state the molecule can redistribute its energy *via* a variety of radiative and non-radiative processes and eventually the population will relax back to the ground electronic state. Figure 1.2.1 summarises the various radiative and non-radiative processes for an isolated typical neutral molecule in the gas-phase.

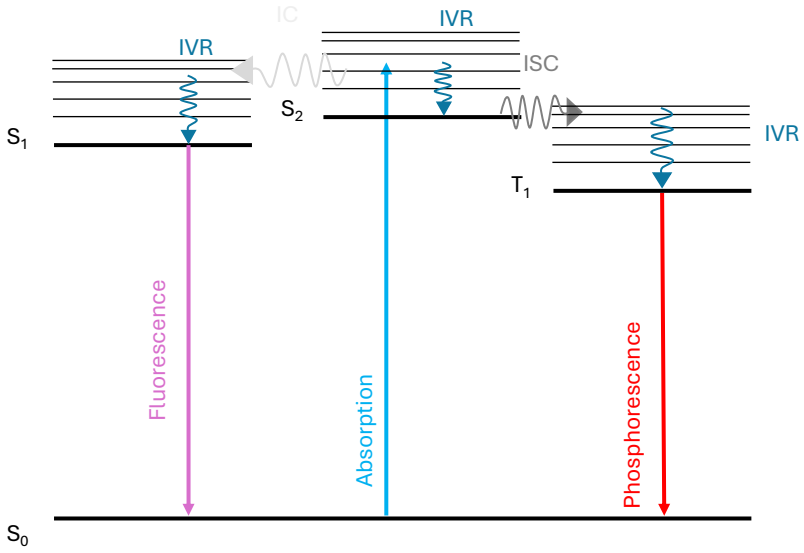

Figure 1.2.1: Jablonski diagram used to illustrate the possible radiative and non-radiative relaxation processes the can occur after the absorption of a photon. Diagram includes intramolecular vibrational redistribution (IVR) of energy, internal conversion (IC), intersystem crossing (ISC), fluorescence and phosphorescence.

Absorption occurs on a timescale of approximately $\sim 10^{-15}$ s, leading to the promotion of the population from the S_0 to S_2 by a photon, see Figure 1.2.1. This process is several orders of magnitude faster than nuclear motion and is, therefore, often considered to be effectively instantaneous. The assumption that nuclear and electronic motions of a molecule can be considered separately due to the significant difference in their timescales is known as the Born-Oppenheimer approximation [14–16]. Following absorption, the molecule may possess excess vibrational energy. Coupling between the vibrational modes can lead to intramolecular vibrational redistribution (IVR), the non-radiative process which typically occurs on the timescale of 1-100 ps. The dissipation of excess vibrational energy from $S_n(v = n)$ to the lowest vibrational mode $S_n(v = 0)$ can then be followed by fluorescence, which is the relaxation of the population from the excited singlet state S_n back to the electronic ground state S_0 through the emission of a photon. Fluorescence, a

radiative process, typically occurs on a tens of picosecond to nanosecond timescale. There is often competition between ultrafast non-radiative and radiative processes. For example, through internal conversion (IC), the excited-state population can relax from an higher singlet state to a lower one. This process is usually significantly faster than fluorescence, occurring on a few femtosecond to few picosecond timescale. Another competing process is intersystem crossing (ISC) from S_n to a triplet state, which is non-radiative. ISC occurs on a 100 ps to several microsecond timescale, and depends on the strength of spin-orbit coupling. Spin-orbit coupling is the interaction between the magnetic fields produced by the orbital-angular momentum and spin of an electron. The triplet state can decay radiativly back to the ground electronic state *via* phosphorescence, emitting a photon in the process. This occurs on a relatively slow microsecond to second timescale.

Studying photochemical dynamics in the condensed-phase introduces an additional layer of complexity. The solvent environment can influence the photochemical behaviour of the solute through properties such as polarity, viscosity, and explicit solute-solvent interactions on the microscopic level [17]. Studying photoactive chromophores in solution is essential for understanding their photochemistry in a more natural environment. An isolated gas-phase environment does not accurately resemble the condition experienced by chromophores in nature. Although, gas-phase studies serve as a useful initial model, they can be built upon by increasing complexity with solvation. Solvation effects can be classified into two groups: specific and non specific interactions. Specific interactions include phenomena such as hydrogen bonding or hydrophobic effects, while non-specific interactions encompass van der Waals and Coulombic forces.[18, 19]. Upon dissolving a chromophore, its electronic properties are altered due to the changing solvent environment, which can lead to structural changes [20]. The surrounding solute structure also changes shape. The introduction of a solvent can impact the ground and excited electronic states of a chromophore, leading to changes in band positions, intensities, and widths in the electronic absorption spectrum. These are

static (equilibrium) solvent effects. Dynamical solvation effects can be observed *via* ultrafast spectroscopy. Figure 1.2.2 displays a schematic diagram for a emissive chromophore. In this example, the solvent molecules reorganise (both spatially and orientationally) to stabilise the chromophore, a process that occurs slower than the charge redistribution within the chromophore itself.

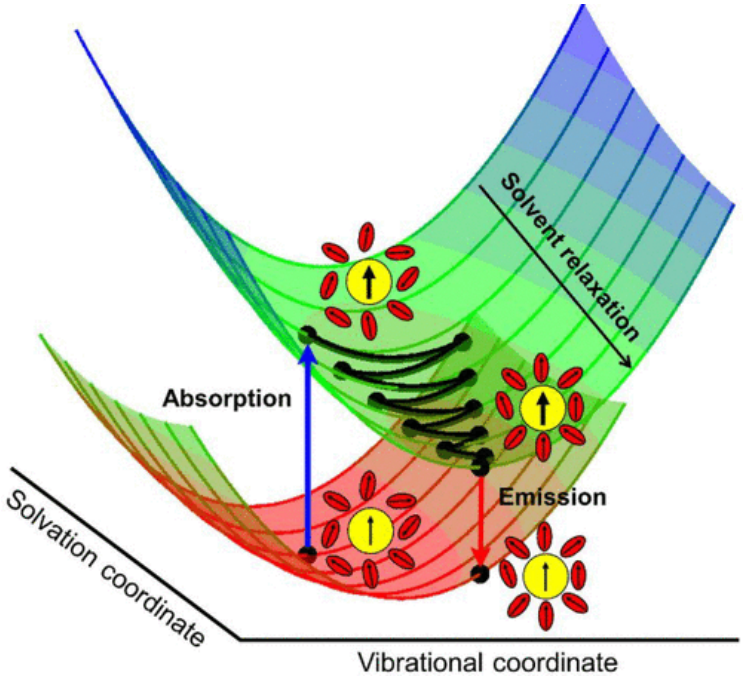

Figure 1.2.2: Schematic diagram of the potential energy surfaces involving some example solvation dynamics. Reprinted (adapted) with permission from [17]. Copyright 2021 American Chemical Society.

In solution, the relative energies of the ground and excited singlet states of anions are lower compared to the gas phase, with respect to the detachment threshold. The anions are stabilised by hydrogen bonding from the surrounding water molecules in the solvent, so the vertical detachment energies (VDE) in solution are usually much greater than those of isolated anions. Additionally, it is also possible to observed solvent dynamics following photoexcitation [21]. In the gas-phase organic molecular anions have typical detachment energies of around 7 eV, whereas the difference in stabilisation energy between the closed shell anion and neutral radical is large and makes detachment energies around 3 eV in aqueous solution. For example, in the case of phenolate the VDE in aqueous solution is 7.1 $\pm$ 0.11 eV [22] while in

the gas-phase it is 2.26 $\pm$ 0.03 eV [23]. The aqueous environment also allows for the formation of solvated electrons ($e^-_{(aq)}$). In water the solvated electron was first discovered in 1962 by Hart and Boag [24]. The solvated electron is the most basic of solvated anion and can be generated in water by direct solvent ionisation or photodetachment of anionic solutes [25]. Understanding the dynamics of the solvated electron is vital as light induced radiolysis is an fundamental reaction in biology and chemistry. The dynamics have been studied by both liquid microjet photoelectron spectroscopy and transient absorption spectroscopy [26–29].

1.3 Ultrafast Spectroscopy

Ultrafast spectroscopy is a field that utilised laser pulses with extremely short temporal resolution, ranging from femtoseconds to attoseconds, to investigate photoinduced dynamics in various molecular systems and materials [30]. The short laser pulses provide the temporal resolution necessary to observe photodynamics on very short timescales, while the specific type of spectroscopic probe used determines the detection method.Ti:sapphire and Ytterbium lasers are commonly chosen systems for generating these ultrafast laser pulses. In this thesis, a Ti:sapphire laser system was used, which is discussed in greater detail in Chapter 2.

1.4 Pump-probe Spectroscopy

The pump-probe method is used in a wide-range of time-resolved spectroscopic techniques, including transient absorption spectroscopy and photoelectron spectroscopy - both of which are used for the work described in this thesis. This method involves two laser pulses, known as the pump and probe pulses. These pulses are overlapped in space and time-zero is said to be when pump and probe are temporally overlapped. The pump pulse excites the sample, with its photon energy tuned to the electronic state of interest. Following this excitation, the probe pulse, which arrives at varying time delays after the pump pulse, interacts with the sample to provide spectroscopic information. By selecting an appropriate spectroscopic method, such as transient absorption or photoelectron spectroscopy, specific changes in the sample can be detected and monitored over time.

Different pump-probe techniques are tailored to suit specific applications and provide unique insights into molecular dynamics. For instance, in photoelectron spectroscopy, the probe pulse ionises the sample, creating a photoelectron whose kinetic energy can be measured. This technique is particularly suited for investigating the electronic structure of molecules and understanding the dynamics of excited states, offering a direct view of the potential energy surfaces. In contrast, transient absorption spectroscopy typically employs a broadband white light probe to track the dynamics by monitoring absorption signatures over time. This method is ideal for following the evolution of electronic states, energy transfer processes, and chemical reactions in real-time, providing a broad overview of the photophysical and photochemical processes at play.

1.5 Transient Absorption Spectroscopy

Transient absorption spectroscopy (TAS) is a well established technique that is widely used to follow the excited-state dynamics as function of time by monitoring changes in absorption signals [31, 32]. However, it is helpful to consider steady-state absorption spectroscopy first. When electromagnetic radiation is passed through a sample at specific wavelength, absorption will occur if the radiation induces a transition from the ground state to a higher lying electronic excited state, as described above. To characterise the absorption of a sample the Beer-Lambert law can be used [33]:

$$A = -\log_{10}(\frac{I}{I_0}) = \varepsilon cl \tag{1.5.1}$$

Where A is absorption, I_0 is the incoming intensity, I is the transmitted intensity, ε is the molar extinction coefficient, c is the concentration of the sample, and l is the path length of the sample. TAS offers the added benefit of time-resolution, allowing for the interrogation of the excited-state dynamics as they evolve. The change in absorption between the ground and excited state is measured as a function of pump-probe delay time and wavelength, $\Delta A(\lambda, t)$. At each time delay, both pump-on and

pump-off measurements are recorded. This allows for the isolation of absorption signatures in the excited state, and the difference signal (Δ) A can be obtained from:

$$\Delta A = -\log_{10}\left(\frac{I_{\text{pump-on}}}{I_{\text{pump-off}}}\right) \tag{1.5.2}$$

Where $I_{\text{pump-on}}$ is the intensity of the light measured with the pump-on and $I_{\text{pump-off}}$ with the pump off. Figure 1.5.1 is a illustration of a typical TAS spectrometer.

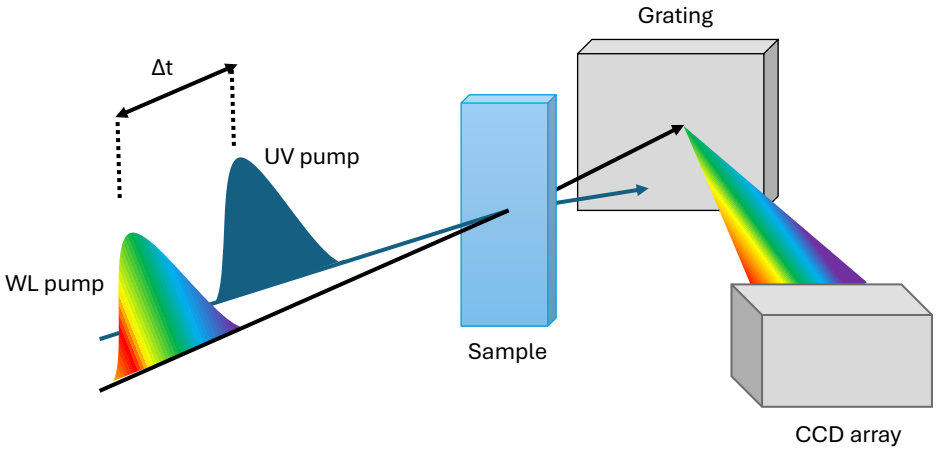

Figure 1.5.1: Schematic diagram of a typical transient absorption spectrometer.

1.6 Absorption Signatures in Transient Absorption Spectroscopy

Typically TAS spectra contain contributions from up to four different processes. These features can be identified from the shape and amplitude of the probe wavelength plotted against the change in absorbance. Obviously spectral features will be unique to the molecule of interest. These can be observed in Figure 1.6.1.

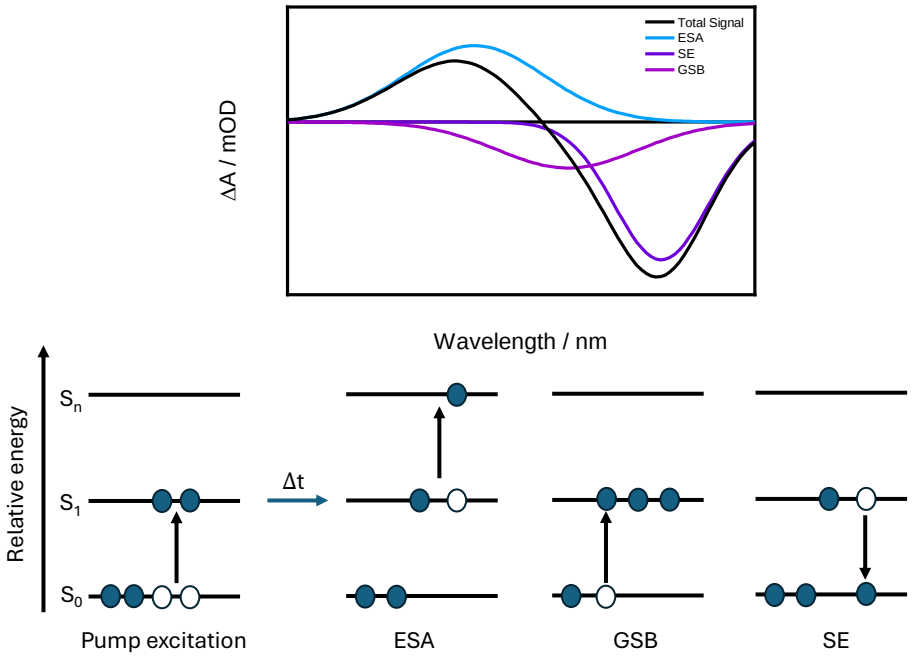

Figure 1.6.1: Graph showing an example TA spectrum at one pump probe delay time. The signal has contribution from GSB, SE and ESA. Below is a schematic diagram of the ESA, GSB and SE contributions.

(1) A ground state bleach (GSB) would present itself as a negative contribution in a TA difference spectrum. This is due to the depletion of the ground state population due to excitation from the pump pulse. Hence, absorbance of the probe-only spectrum will be less in the region of the steady-state absorption spectrum of the molecule, resulting in negative signal in the corresponding region. This feature will be present in the region of the probe spectrum that matches the steady-state absorption spectrum.

(2) Stimulated emission (SE) occurs following photoexcitation of a singlet excited state by the pump pulse. The probe pulse can then induce emission, therefore releasing a photon. Due to the larger number of photons seen by the detector in the pump-probe spectrum in comparison to the pump-only spectrum a negative difference spectrum is obtained. This typically will present itself in the region of the probe spectrum matching the steady-state emission spectrum, making it beneficial to know what the photoemission spectrum looks like before beginning to analyse

TAS data. The SE is observed to shift to longer wavelengths than the GSB.

(3) Excited state absorption (ESA) portrays itself as a positive signal in a TA spectrum. Following photoexcitation to a singlet state by the pump pulse, the probe can induce further excitation of the system to higher lying excited singlet states. Since, the sample absorbs some of the incident probe photons there will be a greater number of photons in the relevant region in the pump-only spectrum, therefore a positive signal arises. The position of the ESA signal in the spectrum depends on the energy difference between the populated electronic excited state and the higher-lying electronic excited state that becomes accessible due to the probe pulse.

(4) Product absorption (PA) also results in a positive ΔA signal. The principle is the same as that of ESA, except the absorption of the probe photons is due to a transient product being formed after photoexcitation.

There a various different approaches to analysing and interpreting a TAS spectrum that has many overlapping features, and these are discussed in detail in Chapter 2.

1.7 Photoelectron Spectroscopy of Liquids

Photoelectron spectroscopy is a extremely useful and widely used technique to determine the electron binding energies of molecules. The work described in this thesis exploits time-resolved photoelectron spectroscopy (TR-PES) to study the photochemical dynamics of phenolate (Chapter 5) to compare with measurements made using TAS (Chapter 3). Although, it is possible to use this technique on neutrals and it can also be applied in the solid- and gas-phase. The development of the liquid microjet in the late 1990s enabled the application of photoelectron spectroscopy to liquid samples [34–36]. The liquid microjets were first used at synchrotrons with intense x-ray pulses [37]. The use of liquid microjets combined with laboratory UV and EUV sources to measure photoelectron spectra is now a very active area of study [38–41]. The work presented in this thesis will utilise

UV pump and UV probe photoelectron spectroscopy. A major advantage of this technique is the ability to use solutions with low concentrations. In contrast, when using x-ray probes in order to obtain a spectrum of decent quality solutes have to have concentration of $\geq$[42] 0.2 M. This is so adequate signal to noise can be obtained as the photoelectron spectrum of water (56 M) has to be subtracted. Due to concentration limits, many organic molecules are excluded, as they are weakly soluble in water.

The arguments presented are similar for neutral molecules, but since this thesis focuses on molecular anions, the discussion will be framed within that context. Following the absorption of a photon by the molecular anion an electron can be detached, *via* the photoelectric effect, and the process can be summarised as:

$$M^- \xrightarrow{h\nu} M^{\cdot} + e^- \tag{1.7.1}$$

Where M^- is a the closed-shell anion, $h\nu$ is the energy of the photon, $M^{\cdot}$ is the corresponding neutral radical formed after photodetachment and e^- is the electron produced from photodetachment. The photon energy is tuned to initiate photodetachment *via* a resonant or non-resonant process and then the electron kinetic energy (eKE) distribution of the ejected photoelectrons is measured. From the eKE the electron binding energy (eBE) of the molecule can be determined from the following:

$$eBE = h\nu - eKE \tag{1.7.2}$$

This relies on Koopmans' theorem: in a closed-shell system the first ionisation energy is equal to the negative of the orbital energy of the highest occupied molecular orbital (HOMO). [43] This assumes there is no reorganisation of the remaining electrons after photodetachment. Therefore, the electron binding energy can be described by 1.7.2. The timescale of electron photodetachment is significantly faster than nuclear rearrangement, thus within the limit of the Born-Oppenheimer approx-

imation. Therefore, the profile of the spectrum is dictated by the Franck-Condon overlap of the two electronic states. In other words, the overlap of the vibrational wavefunctions of the anion and the neutral radical formed after photodetachment.

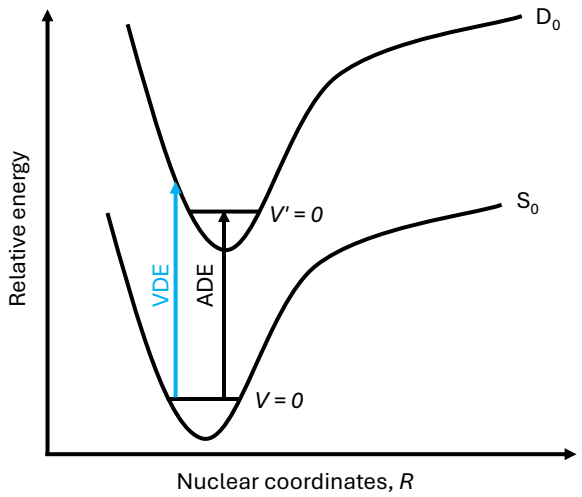

Figure 1.7.1: Potential energy curves in the ground electron state (S_0) and the corresponding neutral radical (D_0) plotted as a function of the nuclear coordinate. The VDE is represented by the blue arrow and the ADE by the black arrow.

In a photoelectron spectroscopy experiment, the measured electron binding energies are characterised as the vertical detachment energy (VDE) and the adiabatic detachment energy (ADE), as depicted in Figure 1.7.1. The VDE is defined as the energy difference between the anion and the neutral radical when the anion is in its ground vibrational state. In contrast, the ADE is the same energy difference, but when both the anion and the neutral radical are in their respective vibrational ground states. In the experimental data photoelectron data presented in kinetic energy, the VDE and ADE are assigned as the peak maxima and the onset of a transition, respectively.

In the gas-phase picture, the valence electrons of a molecular anion are weakly bound, so a single UV photon usually has sufficient energy to initiate photodetachment. The mechanisms of electron detachment from molecular anions can be

classified into direct and indirect detachment processes. Photoelectron spectra will have contribution from both of these processes. Direct detachment will give rise to a photoelectron spectrum where the maximum eKE is determined by the overlap of the Franck-Condon vibrational wavefunction of the ground electronic singlet state (S_0) with the neutral radical (D_0). In contrast, as the valence electrons are weakly bound almost all of the electronic excited states of the molecular anion are above the ADE. Therefore, they are susceptible to indirect detachment and the photoelectron spectra will have contributions from both direct and indirect detachment. Molecular anions that do not undergo significant changes in geometry during photodetachment tend to conserve vibrational energy. Hence, if photodetachment to D_0 occurs *via* a resonant electronic state, such as S_n, it results in photoelectrons with kinetic energy eKE $\sim h\nu$ - E (D_0) - E_{vib}. Here, E_{vib} represents the excess vibrational energy in S_n (where $E_{vib} = h\nu - E(S_n)$), which is conserved in D_0.

Often, a single photon of UV light does not provide sufficient energy to initiate photodetachment, meaning its energy is lower than the VDE. Therefore, there are two different methods for initiating photodetachment. A non-resonant multiphoton ionisation, where the ground state absorbs multiple photons and the cumulative energy is larger than the VDE and there are no nearby resonances at the single photon level, see Figure1.7.2. Alternatively, resonant multiphoton ionisation, where the first photon promotes the molecule to an excited state ($S_0 \rightarrow S_n$), and then a second photon exceeds the energy of the VDE. Both these processes are illustrated in Figure 1.7.2.

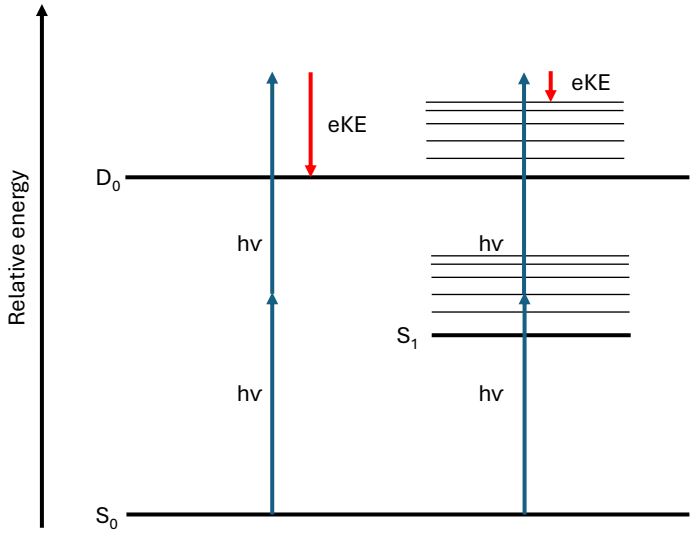

Figure 1.7.2: Schematic energy level diagram illustrating: **Left:** a non-resonant multiphoton ionisation and **Right:** resonant multiphoton ionisation. Blue arrows are the photon energy used to initiate photodetachment and red arrows are the kinetic energy of the photoelectrons measured in a photoelectron spectroscopy experiment.

Photoelectron spectroscopy must be conducted under high vacuum conditions to minimise the scattering of ejected photoelectrons. This presents a unique challenge when applying the technique to liquids, as these conditions can cause liquid samples to freeze or evaporate. The liquid microjet delivers the liquid sample into the vacuum chamber with high-velocity laminar flow. The liquid beam is typically 10-25 μm in diameter. These conditions reduce the surface area exposed to vacuum and maintains the liquid in a stable flow within the laminar region, preventing it from breaking up into droplets. This and other technical challenges are discussed in Chapter 2.

The ability to study photochemical dynamics in solution is of great advantage due to the large influence solvation can have. The solvent can have various implications on chemical and biological processes [17]. Examples include; the excited-state

photochemistry [44], structural and function of biomolecules [45], and the thermochemistry of chemical reactions [46, 47]. Time-resolved photoelectron spectroscopy utilises the pump-probe technique described earlier. The pump is resonant with an excited electronic state and the delayed probe pulse detaches the electron, thus employing a photodetachment *via* a resonant process (see Figure 1.7.2). The capabilities of this approach, along with preliminary data, will be discussed and presented in this thesis. Figure 1.7.3 provides an example of the potential energy pathways in time-resolved photoelectron spectroscopy.

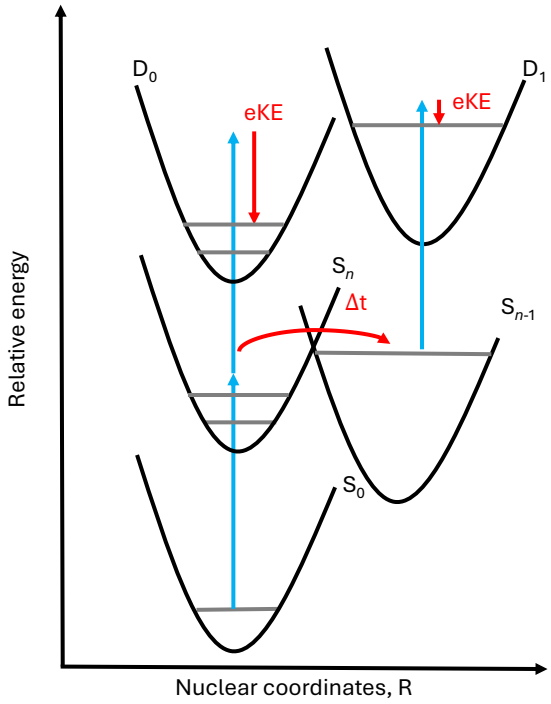

Figure 1.7.3: Schematic energy level diagram illustrating electronic and vibrational dynamics in a time-resolved photoelectron spectroscopy experiment.

Another added challenge that arises from photoelectron spectroscopy of liquids is the inelastic scattering of the ejected photoelectrons, resulting in the distortion and loss of the kinetic energy thus changing the measured distribution. After photoexcitation the photon is absorbed by the system of interest, resulting in the electron detaching into the liquid conduction band. The electron travels through the liquid and then eventually escapes into the vacuum.

The mean free path (MFP) is defined as the distance the electron can travel through the liquid before it experiences scattering. The inelastic mean free path (IMFP) is the average distance an electron can travel before experiencing inelastic scattering, which results in loss kinetic energy. The elastic mean free path (EMFP) is analogous to the IMFP but refers to the average distance an electron travels before undergoing elastic scattering, where the electron's kinetic energy remains unchanged. The IMFP characteristic plot is commonly known as the universal curve. For kinetic energies ranging from 0 to 4 eV, the IMFP typically spans from 2 to 3.5 nm. While the shape of the IMFP curve varies significantly depending on the material, for liquids, direct measurements are challenging, leading to considerable uncertainty about the precise shape of the curve [48].

A major challenge in performing liquid microjet photoelectron spectroscopy with UV laser pulses is the limited universal understanding of the effects of inelastic scattering on low electron kinetic energy (eKE) electrons [26, 49, 50]. Previously, three methods have been employed to extract accurate electron binding energies. The method developed by the Fielding group builds upon this prior work by combining elements of the two earlier approaches[51–53]. This method integrates Monte Carlo simulations of electron scattering with spectral inversion, based on the assumption that extreme UV measurements yield the true photoelectron spectra[54]. The different concentration profiles associated with solutes of differing solubility were also taken into consideration. A key finding from their work was that for weakly soluble organic molecules whose concentration profiles peak around 1 nm or less into a liquid from the surface of the jet, is that the inelastic scattering is < 0.1 eV which is around the limit of accuracy of liquid jet measurements. Therefore, for the work presented in this thesis presented in chapter 5 inelastic scattering can be ignored for the time-resolved measurements.

1.8 Summary

This chapter has introduced some of the basic photochemistry/photophysics of molecules following the absorption of UV and the two experimental techniques. Studying chromophores in the condensed phase allows us to understand how the environment affects their dynamics, providing a closer approximation to what their behavior would be like when they are found in nature. The next chapter will provide a detailed discussion of the transient absorption and liquid microjet spectrometers used to record the data presented in this thesis and the data processing and data analysis tools used to interpret the data. Following this, Chapters 3, 4, and 6 will present three different transient absorption spectroscopy studies. Finally, Chapter 5 will present and discuss preliminary time-resolved liquid microjet photoelectron spectroscopy data of aqueous phenolate.

Chapter 2

Experimental Methods

This Chapter outlines the two experimental setups and the procedures for data collection and processing employed to obtain the experimental data presented in Chapters 3, 4, 5 and 6. The first technique discussed is femtosecond-transient absorption spectroscopy used to study the photoinduced dynamics of aqueous phenolate, substituted phenolates and derivatives of oxyluciferin. The second technique is liquid-microjet photoelectron spectroscopy employed as a complementary technique to transient absorption spectroscopy to investigate the photoinduced dynamics of aqueous phenolate.

2.1 The Femtosecond Laser System

A commercially available Coherent Astrella-HE laser system was used to generate femtosecond laser pulses for all the experiments discussed in this thesis. The Coherent Astrella-HE laser system is a titanium-doped sapphire (Ti:sapphire) laser system that includes a Vitara mode-locked oscillator that generates femtosecond pulses at an 80 MHz repetition rate with a central wavelength of 800 nm. The Vitara is pumped by a Verdi continuous wave 532 nm Nd:YLF laser. Upon leaving the Vitara, the laser pulses are temporally stretched before entering a regenerative amplifier, where the Ti:sapphire crystal serves as the lasing medium. A Revolution nanosecond 527 nm Nd:YLF laser then pumps the crystal. Every millisecond, a pockel cell traps a pulse inside the cavity, where it is amplified and then finally emitted. The emitted compressed pulses have been measured to have duration of

32 fs and a central wavelength of 800 nm. The Coherent Astrella-HE operates at a 1 kHz repetition rate and the outputted pulses are 9 mJ. The 9 mJ, 32 fs pulses are split among several experimental end stations. For the work presented in this thesis the focus will be on the transient absorption spectroscopy and the liquid microjet photoelectron spectroscopy end stations.

2.2 Transient Absorption Spectroscopy

The principles behind transient absorption spectroscopy (TAS) are described in Chapter 1. A commercial TAS spectrometer, Ultrafast Systems Helios Fire, was used to record the data presented in Chapters 3, 4, and 6. The Coherent Astrella-HE provides 2.4 W of power to the TAS setup. Of this, 1.21 W is used to generate tunable pump laser pulses, while the majority of the remaining power is allocated to the femtosecond stimulated Raman beam line, with a small proportion used to generate the broadband probe beam. The tuneable pump beam is generated by an optical parametric amplifier (OPA, specifically the Coherent OPerA Solo). The wavelength of the pump beam is confirmed with a spectrometer (ocean optics). For the work presented in Chapters 4 and 6 it came to my attention whilst writing this thesis that the spectrometer used to set the wavelength of the OPA had become uncalibrated in mid 2023, so for measurements made since then, the scattered light observed in the TAS data was used to define the pump wavelength instead. The 800 nm pulses allocated for the generation of the probe pulses are directed to a cube retroreflector mounted on a mechanical delay stage with a maximum delay of 8 ns, achieved by two double passes. The 800 nm pulses are then focused into a crystal, where the broadband probe is generated. The Helios system uses three different crystals for the generation of the probe pulses, each tailored for specific wavelength ranges: 350-650 nm (UV, calcium fluoride), 450-750 nm (visible, sapphire) and 800-1600 nm (near-infrared, YAG). The pump pulse is directed by mirrors through a lens tube, allowing the focal length, and thus the spot size of the beam to be adjusted. The pump pulse is focused around 1 mm in front of the sample cell windows to avoid burning sample on to them. Both the pump and probe pulses are then

spatially overlapped within the sample. This is achieved by adjusting the pointing of the final pump mirror before the sample holder. Pump-on and pump-off measurements are achieved by passing the pump beam through a mechanical chopper operating at 500 Hz, half the repetition rate of the laser. The probe beam travels straight through the sample to the CCD detector for UV and visible or to a fibre detector for the nIR.

There are two options for sample holders: a cuvette that can be rastered or a Harrick flow cell used with a peristaltic (Masterflex 77390-00) pump. The Harrick flow cell can be constructed with varying path lengths (6 μM to 1 mm), with a 100 μm path length used for the results presented in this thesis. The peristaltic pump that flows the liquid sample through the cell ensures each laser pulse interacts with fresh sample.

When setting up a TAS measurement, both the pump and probe beams are first aligned down the table. In the Helios software, the desired probing region is selected, prompting the software to move a mirror to the corresponding crystal for generating the broadband probe pulse. The probe spectrum is optimised by adjusting a neutral density filter to control how much 800 nm light it is pumped with. The optimal position is when a broad stable white light spectrum spanning the entire desired wavelength region required can be observed on the software, an example spectrum is displayed in Figure 2.2.1.

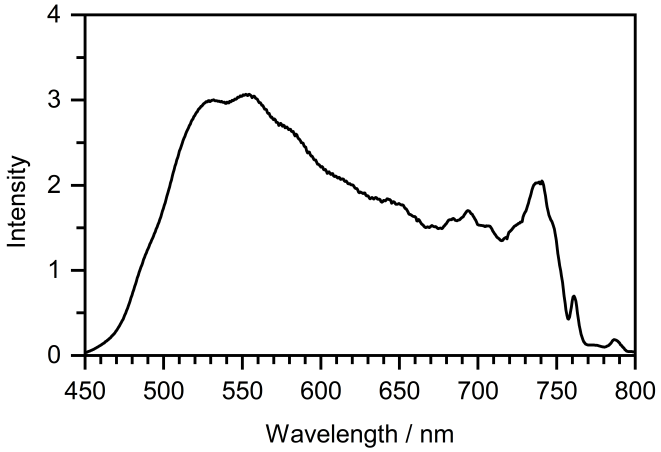

Figure 2.2.1: Example of the probe pulse white light spectrum generated from focusing a 800 nm pulse into a sapphire crystal.

The polarisation of the pump pulse is set using a Berek waveplate so that the relative polarisations of the pump and probe pulses are at the magic angle. Spatial overlap of the pump and probe pulses is then found using a reference sample that gives a very large absorption signal, usually zinc porphyrin. The pump pulse should be larger than the probe pulse at the point of spatial overlap to ensure only the excited state population is probed. Time zero is then defined in the Helios software as the pump-probe delay time at which the absorption signal begins to grow on the blue edge of the spectrum. Before time zero there should be no signal. Then the pump power is adjusted using a neutral density filter to the value desired for the experiments. The sample of interest, typically in a Harrick flow cell, is then placed in the path of the overlapping pump and probe beams. This setup is mounted on a small translation stage, which is adjusted to ensure that the laser pulses overlap in the middle of the cell. Scattering of the pump laser is often detected, and to reduce this signal, the probe beam directed to the detector is often irised. The pump-probe delay times are then defined in the software and then the data can be collected.

2.3 Pre-processing of Transient Absorption Spectra

Before a TAS spectrum can be interpreted some steps to process the data have to be undertaken. Specifically, these steps involve subtracting the solvent-only spectrum from the solute spectrum, background subtraction to remove any time independent

contributions, and finally performing the chirp correction. All processing of TAS data in this thesis was carried out using the *Surface Xplorer* software.

2.3.1 Solvent Subtraction

When recording a TAS spectrum of a solute, it is considered best practice to also record a spectrum of the solvent without the solute. This solvent-only spectrum serves as a reference, helping to identify any background signals or artifacts arising from the solvent itself. This ensures that the recorded data accurately reflects the true dynamics and spectral features of the solute under study. In the *Surface Xplorer* software this is a built in feature that simply allows the data matrix of the solvent to be subtracted from the solute. All transient absorption spectra in this thesis were recorded in aqueous solution, so no solvent features were observed. Solvated electrons can be generated in aqueous solution; therefore, the pump power used was kept low enough to avoid this issue. An example of TAS data before and after solvent subtraction is presented in Figure 2.3.1. There is minimal difference between the before and after subtraction data since the solvent spectrum has zero signal. Solvent subtraction can add noise to TAS data and is not always necessary if there is no solvent signal.

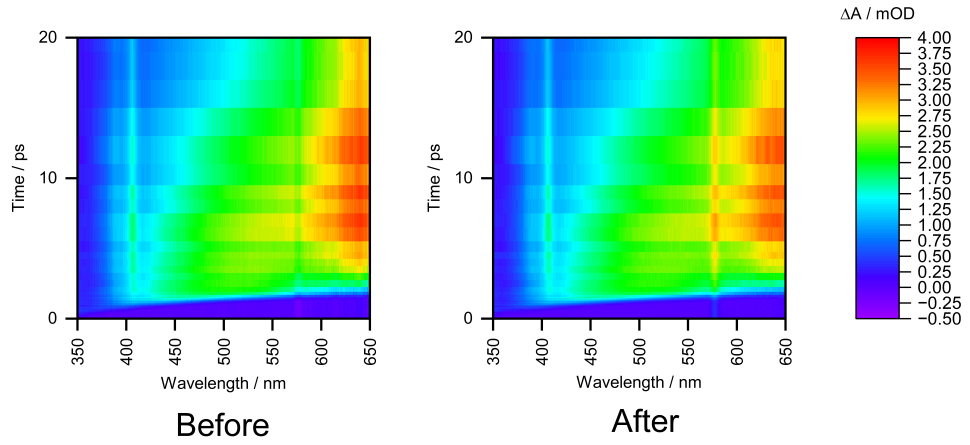

Figure 2.3.1: An example of transient absorption data before and after solvent subtraction.

2.3.2 Background Subtraction

To eliminate any non-time-dependent contributions to the spectrum, a background subtraction is performed. An example of such a contribution is scattered light from the pump beam reaching the detector. The process involves averaging several spectra recorded before time zero and subtracting this average from the entire dataset.

2.3.3 Determining the Instrument Response Function

The IRF defines the temporal resolution of the experiment. The solvent-only data is fitted to a sum of Gaussian functions at various probe wavelengths using the *Surface Xplorer* software. This fitting process determines both the IRF and the position of t_0 at each specific probe wavelength. The instrument response function (IRF) for the data present in Chapters 3, 4 and 6 are all determined in the following way. An example fit to determine the instrument response function is displayed in Figure 2.3.2.

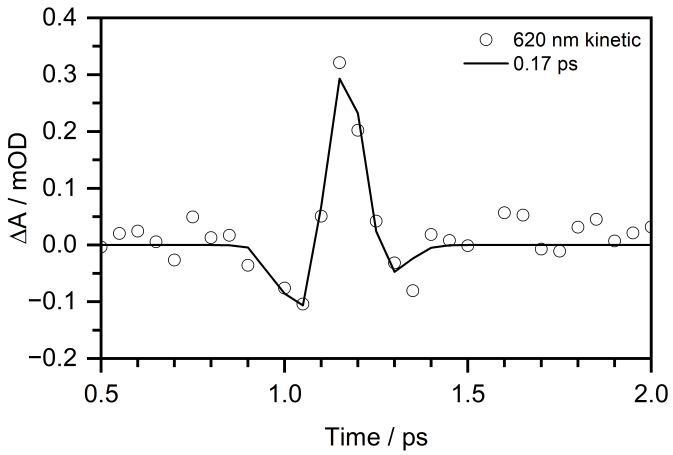

Figure 2.3.2: An example fit to determine the IRF. Fit is conducted at a probe wavelength of 620 nm and the IRF was found to be 0.17 ps.

2.3.4 Chirp Correction

At early pump-probe delay times, it is typical to observe the signal shifting from blue to red wavelengths due to the difference in the group velocity of each wavelength. This phenomenon is known as chirp. In other words the longer wavelengths arrive later in time than the shorter ones [31]. The chirp correction must be carried

out on every TAS data set to determine the true value for time-zero. The chirp correction is carried out in the *Surface Xplorer* software where the following function is fit to the data:

$$t_0 = a\sqrt{\frac{b\lambda^2 - 1}{c\lambda^2 - 1}} + d. \tag{2.3.1}$$

Figure 2.3.3 shows example transient absorption data before and after chirp correction.

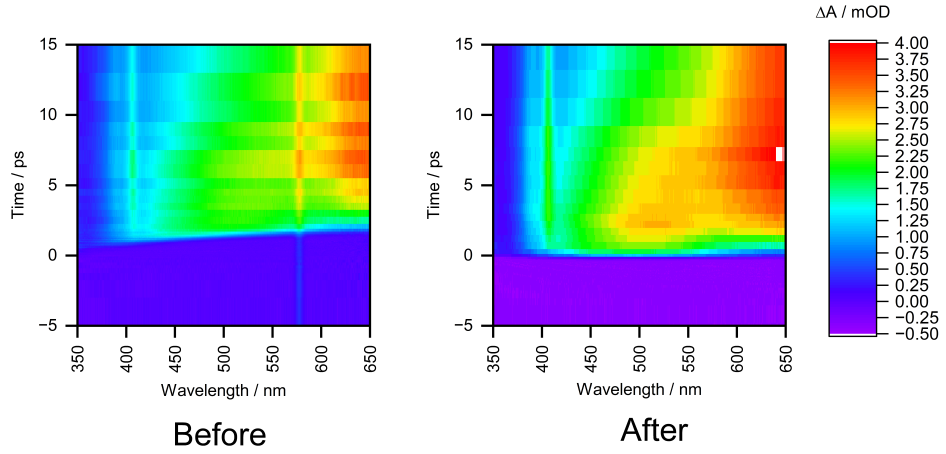

Figure 2.3.3: An example of transient absorption data before and after chirp correction

Where a,b,c,d are the parameters determined during the fit, λ is the wavelength, and t_0 is time zero. The chirp was corrected using a spectrum of the neat solvent, which in this thesis is water, where a non-resonant pump-probe signal can be clearly observed at time zero for all probe wavelengths. This signal has been attributed to impulsive and stimulated Raman scattering of both the pump and probe pulses [55, 56].

2.4 Analysis of Transient Absorption Spectra

TAS data is challenging to interpret due to the high likelihood of numerous overlapping absorption features in the spectrum (see Chapter 1 Section 1.6). These features are also likely to have different timescales associated with them and thus the dynamics typically involve various overlapping signals, resulting in a mixture of

different components in the kinetics and amplitudes. There are various approaches to deconvolute the overlapping spectral signals such as applying a kinetic model to the data or employing a global analysis method. A kinetic model is typically applied when there is some level of understanding of the dynamics present in the TAS spectrum. When there is less prior knowledge about the system it is often more appropriate to employ a global analysis method.

For the data in Chapter 3 all possible contributions to different spectral regions were considered, and they were systematically removed so that instrument functions convoluted with exponential rises and decays could be fitted to extract the relevant time constant. Various software packages exist for the analysis of TAS data examples are Glotaran, Pyglotaran, and KOALA [57, 58]. For the deconvolution of the dynamics in the TAS data presented in Chapters 4 and 6 the University of Bristol's KOALA software was employed[59]. This software extracts the kinetics by fitting a basis function to each feature in the TAS spectrum at every pump-probe delay time. The details of how this analysis was approached in this thesis is described in Chapters 3, 4 and 6, focusing on the study of the photooxidation dynamics of phenolate in aqueous solution, the impact of methyl-group substitution on the photooxidation dynamics of phenolate in aqueous solution, and the emission properties of bioluminescent emitters, respectively.

2.5 Liquid-microjet Photoelectron Spectroscopy

Liquid-microjet photoelectron spectroscopy (LJ-PES) is a powerful experimental technique that allows for the measurement of electron binding energies to be measured directly for molecules in aqueous solution. A schematic diagram of the UCL liquid-jet photoelectron spectroscopy experimental apparatus is displayed in Fig 2.5.1.

The spectrometer in comprised of three sections: the interaction chamber, time-of-flight (TOF) chamber and the detection chamber. In the interaction chamber, as displayed in Figure. 2.5.1, the solution is pumped through a 20 μm fused silica

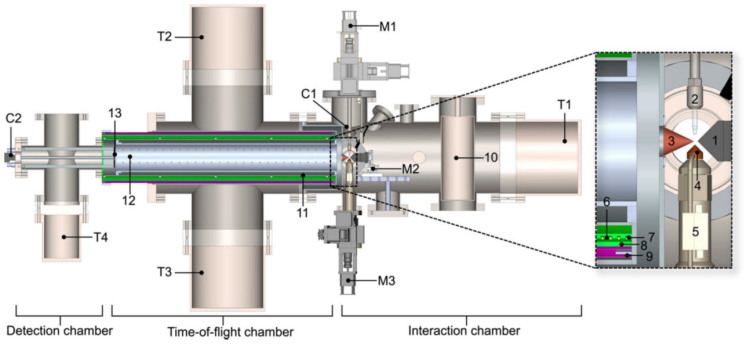

Figure 2.5.1: Schematic diagram of the liquid-microjet photoelectron spectrometer. The inset displays the interaction region of the spectrometer and shows; (1) 1 T magnet, (2) assembly holding the liquid-microjet nozzle, (3) the skimmer, (4) the catcher, (5) the heating element for the catcher, (6) inner PTFE sleeve with a groove for the solenoid, (7) the solenoid, (8) outer PTFE sleeve and (9) double μ-metal tube. (10) cold trap. (T1-4): are the turbomolecular pumps operating at speeds of 1000 (T1), 600 (T2 and T3) and 220 (T4) $1\,s^{-1}$. While there is liquid a pressure of around 2×10^{-5} mbar is achieved in the interaction region. (M1-3): xyz translation stages which allow for movement of the liquid-microjet (M1), the magnet (M2), and the catcher (M3). (C1-2): CMOS cameras used to aid alignment of the liquid-microjet to the catcher (C1) and observe the flourescence of the phosphor screen behind the microchannel plates (C2). The time-of-flight chamber has (11) a flight tube and (12) a drift tube. The detection chamber contains a double-stack microchannel plate (MCPs). Reproduced from Ref. [60]

nozzle (2) by a high-performance liquid chromatography (HPLC) (Microliquids 02) pump. The flow rate of the HPLC pumps was optimised for each experiment in order to help minimise the streaming potential (see Section 2.5.5). For a solvent of water the pump was typically operated with flow rates between 0.5-0.8 mL min^{-1}. Usually, the jet of liquid is aligned at atmospheric pressure to be in the centre of the 500 μm hole in the top of the heated catcher (4) using the M1 motors and then is recirculated. However, due to some technical problems with the motors this meant that for the results presented in Chapter 5 the catcher could not be used. Therefore, a liquid nitrogen cold trap mounted in place of the catcher was used. Experiments could be conducted for approximately 6 hours before the trap was full. The nozzle tip should be $\sim$2 mm above the point of ionisation and then the catcher should be $\sim$1 mm below this. For the case of the cold trap the nozzle tip should

also be $\sim$2 mm above the point of ionisation. The stream of liquid maintains laminar flow for approximately 3-4 mm. A peristaltic pump was operated between 160 - 170 rpm to efficiently removed the liquid from the bottom of the catcher assembly.

Within the interaction region there is a 1 T magnet (1) mounted on a *xyz* translation stage (M2) and opposite is the skimmer (3). There is also a gas nozzle used for calibrating the spectrometer with xenon and nitric oxide gas. Components in the interaction region are coated in Aquadag, a water based colloidal graphite coating. The graphite is applied to the the magnet, skimmer, catcher, liquid microjet nozzle, and gas nozzle. This ensures all components in the interaction region have the same work function and therefore, a constant vacuum level around the ionisation point. For operation during experiments the nozzle is positioned in the centre of the skimmer and the magnet with $\sim$2 mm of space either side. The alignment of the magnet and the laser can be checked with the CMOS camera that images the phosphor screen with $+5000\ V$ applied to it. The distribution of the photoelectrons on the phosphor screen can be monitor while ionising Xe (2+1) with 249.7 nm. This will produce a line of photoelectrons on the phosphor screen, which corresponds to electrons emitted along the axis of the laser. The length of the line corresponds to the skimmer diameter. The alignment is optimised when the line of photoelectrons its sharpest. The femtosecond laser light interacts with the liquid perpendicular to the axis of the magnet and the skimmer. The photoelectrons ejected from the liquid are directed by the magnet through the skimmer into the TOF tube. A turbomolecular (Leybold TURBOVAC 1000c) differentially pumps the interaction region to a pressure of 2×10^{-5} mbar during operation with the liquid-microjet running, and approximately 1×10^{-6} mbar without it. This pump operates at 1000 ls^{-1} and is backed by a rotary pump (Edwards 28) with a maximum operating speed of 32.3 $\mathrm{m}^3\mathrm{h}^{-1}$. The TOF region is differentially pumped by two turbomolecular pumps (Leybold TURBOVAC 600c) operating at 600 ls^{-1} maintain a pressure of 2×10^{-7} mbar. The detector region has another smaller turbomolecular pump (Edwards EXT250) operating at 250 ls^{-1} and the pressure in

this region is 4×10^{-7} mbar. The turbomolecular pumps in the TOF and detector regions are backed by two scroll pumps (Leybold Scrollvac SC15D and SC30D) and they have maximum pumping speeds of 15 and 30 m^3h^{-1}, respectively.

2.5.1 Optical Layout

Section 2.1 discusses in greater detail the optical layout for femtosecond laser system employed in these experiments (Figure 2.5.2). Figure 2.5.2 is a schematic diagram of the pump and probe beam lines from the laser system to the chamber. The pump beam is generated by an optical parametric amplifier (OPA, Coherent OPerA Solo) providing tuneable wavelengths from 235-2600 nm. When two-colour experiments are performed, the probe is generated by the process of third harmonic generation (THG). A portion (1.47 W) of the 800 nm pump laser is passed through a β-barium-borate (BBO) crystal to frequency double via second harmonic generation (SHG). The 400 nm produced is then spatial and temporal overlapped with the residual 800 nm to produce 267 nm from the process of THG. For time-resolved experiments, the 267 nm probe beam is delayed mechanically with respect to the pump beam using a 125 mm delay stage (Newport, DL125). After the delay stage the probe beam is reflected off a dichroic mirror (chosen depending on required wavelengths) and the pump beam is transmitted through the back of the same dichroic mirror. This makes the beams collinear and then they are directed by three mirrors to a lens with a 30 cm focal length where both beams are focused into the chamber.

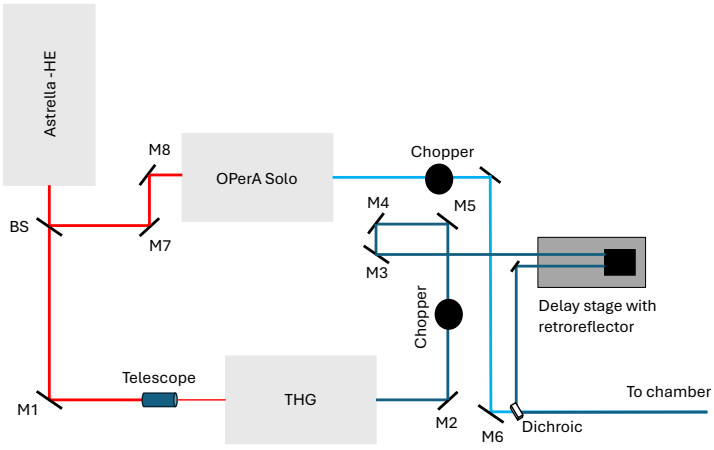

Figure 2.5.2: Diagram of the optical layout. 800 nm beams are shown in red and all UV beams are displayed in blue. The Astrella-HE provides 800 nm which is divided by a beam splitter to the OPA and the third harmonic generation (THG) unit. The OPA arm generates the tuneable pump beam and the THG arm generates the 267 nm probe. The probe beam is delayed with respect to the pump beam with a mechanical delay stage. Then both beam are combined with a dichoric mirror, and from here travel collinear with one another to the vacuum chamber. Mirrors are labelled M1-M8.

2.5.2 Interaction Region

Figure 2.5.3 is a photograph of the inside of the vacuum chamber, showing the interaction region where the laser pulses interact with either a liquid or gas to generate photoelectrons. The liquid micro-jet nozzle is inserted into the interaction region and sits between the skimmer (1) and the magnet (2). The liquid stream is aligned into the recirculating catcher (note the procedure for doing this is described in Section 2.5.6) (3) to remove the liquid from the vacuum chamber. The strong 1 T magnet is comprised of two magnetised cylinders made of Sm_2Co_{17}. The tip of the magnet is a 15 mm iron cone. As stated previously, photoelectrons are generated by the laser pulses interacting with either the liquid or gaseous sample. Once generated, the ejected photoelectrons are directed by a 1 T permanent magnet, which is mounted on an XYZ translation stage to ensure precise alignment of the magnetic bottle. The magnet's tip is positioned 1 mm away from the microjet nozzle and 2 mm from the skimmer. The skimmer, with a 300 μm orifice, allows for differential pumping between the interaction region and the time-of-flight chamber. After

passing through the skimmer, the photoelectrons travel down the flight tube, where their velocities are measured to determine their kinetic energies. Photograph of the nozzle is shown in Figure 2.5.4

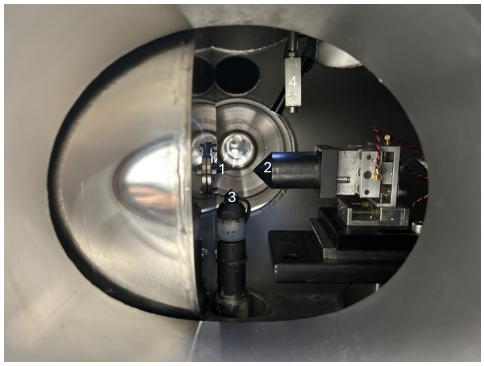

Figure 2.5.3: Photograph of the interaction region. 1. Is the skimmer, 2. Soft iron cone of the 1 T magnet, 3. catcher and, 4. Torch, so inside of chamber can be seen on camera. The skimmer, magnet, catcher and liquid microjet nozzle (when present) are all graphite coated to ensure they have the same work function, which minimises the potential gradients.

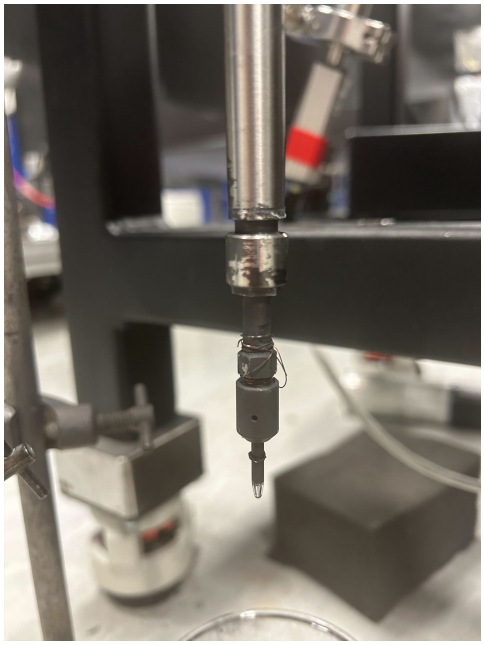

Figure 2.5.4: Photograph of the the graphite coated 20 μm fused silica nozzle.

2.5.3 Magnetic Bottle Time-of-Flight Spectrometer

The UCL liquid microjet spectrometer employs a magnetic bottle time-of-flight (TOF) method to measure the photoelectrons. Although various other detection

methods are available, such as velocity map imaging and hemispherical analysers [61, 62], the magnetic bottle TOF technique is preferred for its high collection efficiency and ability to detect low-energy electrons effectively. TOF spectroscopy operates on the simple principle: a photoelectron is ejected and travels a known distance before its arrival time is recorded by a microchannel plate (MCP) coupled with a phosphor screen (Beam Imaging Solutions, BOS-25). From the recorded arrival time, the velocity of the photoelectron can be determined using the equation:

$$v = \frac{d}{t}. \tag{2.5.1}$$

Where v is velocity, t is the measure arrival time, and d is the distance traveled. From the determined velocity the kinetic energy of the photoelectron can be determined from:

$$E_k = \frac{1}{2} m_e v^2. \tag{2.5.2}$$

Where E_k is kinetic energy, m_e is the mass of the electron, and v is velocity. The magnetic bottle component of the spectrometer is formed by combining the magnet in the interaction region (see Section 2.5.2) with a solenoid placed in the drift tube. The 1 T magnet provides a strong inhomogeneous magnetic field in the interaction region; the solenoid provides a weak homogeneous field of 2 mT, which was previously determined. Pressures of $\sim 5 \times 10^{-7}$ mbar are maintained, with the liquid microjet running, through the use of differential pumping which is essential to reduce electron scattering and allowing for the operation of the MCP detector.

2.5.4 Conversion of Time-of-Flight Data to Photoelectron Kinetic Energy

Data recorded using the UCL spectrometer is collected in the form of electron counts as a function of their TOF. The raw data has to first be transformed into electron kinetic energy and then has to be corrected for the instrument function (efficiency of collection efficiency as a function of electron kinetic energy), the streaming potential and the vacuum level offset (see Section 2.5.5). To calibrate

the spectrometer we use gaseous specious (NO and Xe), which have well known ionisation potentials so can be used to convert of TOF to eKE.

Figure 2.5.5 is an example calibration curve, with the magnet in the close position. A series of non-resonant multiphoton ionisation TOF spectra of nitric oxide (NO) vibronic transitions ($X^2\Pi_{\frac{1}{2}}$, v"= 0) $\rightarrow$ NO ($X^1\sum^+$, v^+) and the resonant xenon (Xe) $^1S_0 \rightarrow {}^2P_{\frac{3}{2},\frac{1}{2}}$ transitions are recorded at both magnet close and magnet far positions.

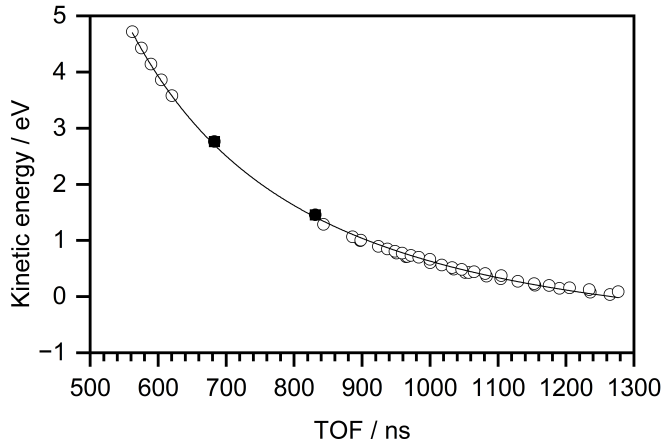

Figure 2.5.5: Exemplar calibration curve for magnet close position. Kinetic energy of photoelectrons from non-resonant NO vibronic transitions (circles) NO ($X^2\Pi_{\frac{1}{2}}$, v"= 0) $\rightarrow$ NO ($X^1\sum^+$, v^+) and resonant Xe transition $^1S_0 \rightarrow {}^2P_{\frac{3}{2},\frac{1}{2}}$ (squares).

Figure 2.5.7 shows an example of four No spectra recorded in the magnet close position. Both are required as experimental data is recorded in the magnet close position, but the streaming potential measurements are made in the magnet far position (see Section. 2.5.5). This is because the jet is translated during the streaming potential measurements and there is not enough space to do so if the magnet is in the close position. Wavelengths range from $\sim$ 235 - 266 nm. Measurements with the magnet in the close position are carried out with the magnet tip $\sim$ 2 mm away from the ionisation point and the magnet in the far position is $\sim$ 8 mm away. The ionisation energies of NO and Xe are well known [63, 64] and therefore, can be used to determine the conversion between TOF and eKE. As displayed in Figure

2.5.5, the expected kinetic energy of the electrons from the ionisation of NO and Xe are plotted against the measured TOF of the photoelectrons. The peak maxima of each vibronic transition in NO is determined by fitting a Gaussian function. From the known ionisation potential and the photon energy used to ionise the electron kinetic energy (eKE) can be determined by the following equation:

$$\mathrm{eKE} = nh\nu - IP. \tag{2.5.3}$$

n is the number of photon, $h\nu$, and IP is the ionisation potential. The peak maxima of the NO vibronic transition and Xe are plotted against eKE. The peak positions are then fit to with the following function:

$$\mathrm{eKE}(t) = \frac{m_e}{2}\frac{s^2}{(t-t_0)^2} - E_0. \tag{2.5.4}$$

eKE is the expected electron kinetic energy from the measured multiphoton ionisation of NO and Xe, m_e is the mass of the electron (9.11×10^{31} kg), s is the length of the TOF tube, t is the measured TOF of each transition, t_0 is the temporal offset between the laser trigger and the digitiser, and E_0 is the energy offset that accounts for any stray electric fields. The calibration constants obtained from the fit in Figure 2.5.5 are $s = 0.70 \pm 0.01$ m , $t_0 = 65 \pm 3$ ns , and $E_0 = 0.97 \pm 0.02$ eV. For all data presented in Chapter 5 the calibration was recorded on the week the experiments were conducted.

The obtained calibration constants from Equation 2.5.4 were then used to convert the TOF data to eKE, and an example of this transformation is shown in Figure 2.5.6.

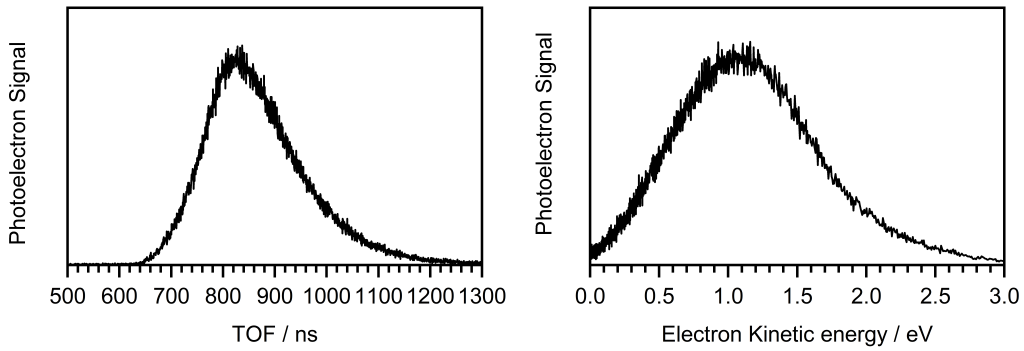

Figure 2.5.6: 1+1 resonant detachment of 0.1 mM Phenolate with 1.8 mM NaOH. λ_{pump} =287 nm and λ_{probe} =267 nm. **Left:** shows the raw experimental data plotted in time-of-flight. **Right:** Plot of the transformed data to kinetic energy. Jacobian transformation has been applied.

The relationship between the TOF of the photoelectrons and their kinetic energy is non-linear. The flight time of the photoelectrons is determine by recording their arrival time at the MCP detector as a histogram. The photoelectron counts are sorted into 0.5 ns bins. The points in TOF are equally spaced and once transformed to eKE the lower energy electrons become closer together and the higher energy electrons are more spread out. Thus, the TOF spectra have to be appropriately scaled with a Jacobian transform, shown in Equation 2.5.5, 2.5.6.

$$\int S(\text{eKE})d\text{eKE} = \int S(\text{eKE}(t))\frac{d\text{eKE}}{dt}dt. \tag{2.5.5}$$

Substituting for the derivative of eKE:

$$\int S(\text{eKE})d\text{eKE} = \int S(\text{eKE}(t))m_e\frac{s^2}{(t-t_0)^3}dt. \tag{2.5.6}$$

The intensity of each bin in TOF must be multiplied by the Jacobian factor, $m_e\frac{s^2}{(t-t_{0)^3}}$. This ensures the intensity of the eKE spectrum is correctly scaled.

At low eKE ($<\sim 0.3$ ev) the collection efficiency of the spectrometer is much lower. As the eKE tends towards zero the influence of stray fields is greater and thus the reduction in collection efficiency at lower eKE has to be characterised. In order to

determine the collection efficiency of the spectrometer, referred to as the instrument function, NO spectra were recorded at photon energies between 235-250 nm, four example spectra are shown in Figure 2.5.7.

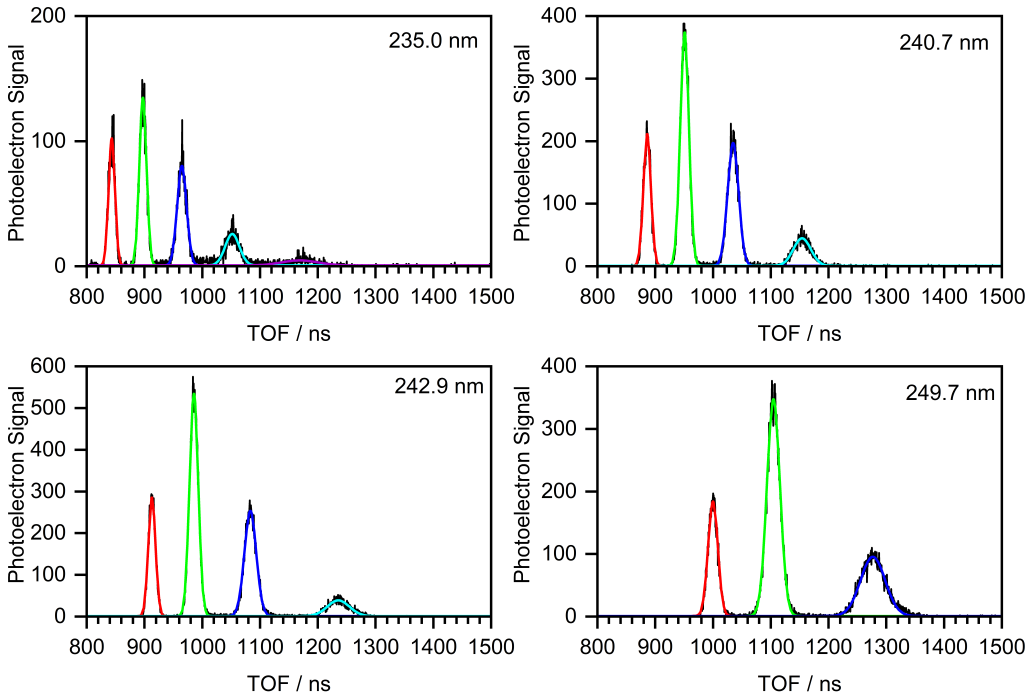

Figure 2.5.7: Example spectra of the multiphoton ionisation of No recorded at 235.0 nm (top left), 240.7 nm (top right), 242.9 nm (bottom left) and 249.7 nm (bottom right). Black lines represent the experimental data. Red, green, dark blue and light blue Gaussians represent the $V^+ = 0,1,2$, and 3 states of NO^+, respectively.

All photoelectron spectra are normalised to the $v^+ = 0$ transition, since it can be observed at all photon energies. Figure 2.5.8 shows an example fit to determine the instrument function. The data points are fit to with an exponential decay (Equation 2.5.7), this is to determine the low energy cut-off which will be approximately the x-intercept.

$$S(\mathrm{eKE}) = Ae^{\frac{-\mathrm{eKE}}{\tau}}. \tag{2.5.7}$$

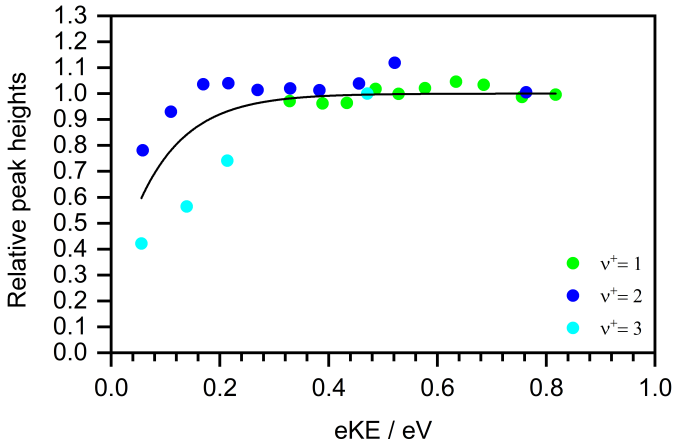

Figure 2.5.8: An example of the instrument function. Relative intensities of the $v^+ = 1$ (green), $v^+ = 2$ (dark blue), and $v^+ = 3$ (light blue) transitions of NO plotted as a function of eKE. All the peak heights are scaled relative to the $v^+ = 0$. The $v^+ = 1$ (green), $v^+ = 2$ (dark blue), and $v^+ = 3$ (light blue) transitions are then normalised to peaks with energies of 0.3 eV within the same vibronic transition. The black line is the exponential function (Equation 2.5.7). Then typically the parameters determined from the fit are used to correct the photoelectron data for the decrease in collection efficiency.

$S(eKE)$ is the normalised intensity of the NO vibronic transitions, A and τ are the parameters that are fit to. All photoelectron spectra in Chapter 5 are divided by the instrument function. The instrument function fit is approximate because it increases to infinity as the exponential function tends towards zero. This is not a true representation, so we cut off our photoelectron spectrum at very low eKE. The spectra presented in Chapter 3 are preliminary, and an accurate instrument function was not recorded at the time. Therefore, they are cut off for kinetic energy < 0.3 eV, although previously, the value would be in the region of < 0.1 eV.

2.5.5 Streaming Potential and Vacuum Level Offset

Photoelectron spectra of liquids are also effected by the streaming potential of the liquid microjet. This streaming potential is the electrostatic charging of the liquid. The liquid microjet nozzles are made of quartz or crystalline silica meaning an electric double layer can form at the liquid-nozzle interface. This results in a build up of electrostatic charge and thus induces an electric field that can raise or lower the vacuum level with respect to the skimmer. The gradient between the ionisation

region and the skimmer, depending on the amplitude and sign of this streaming potential causes the ejected photoelectrons to be accelerated or decelerated which shifts the measured photoelectron spectra to higher or lower eKE.

Three methods have been employed in the literature [65–67] for reducing the streaming potential: the addition of salt to the solution, the changing of the flow rate to alter the velocity profile of the liquid-jet and the application of a voltage bias to the solution [61, 68]. For all measurements in this thesis a low concentration of sodium hydroxide (NaOH), $\sim$ 1.8-2 mM, was added to deprotonate phenol to make phenolate and also minimise the streaming potential. This minimises the streaming potential effectively, and then to get it to as close to zero as possible the flow rate is adjusted, 0.6-07.5 mL min^{-1}.

In order to correct the measured photoelectron spectra for the streaming potential it must be experimentally quantified. This is achieved by recording photoelectron spectra of the $\text{Xe}^1\text{S}_0 \rightarrow^2 P_{\frac{3}{2}}$ transition at different distances between the liquid-microjet and the skimmer. The magnet is translated to the far position for these measurements to ensure the nozzle does not hit it. Then in increments the nozzle is moved away from the ionisation point and a photoelectron spectrum is recorded at each distance. An example of a streaming potential measurement and fit is displayed in Figure 2.5.9.

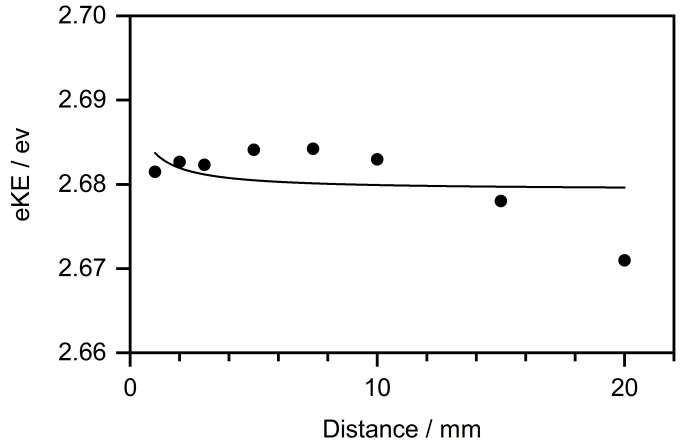

Figure 2.5.9: Plot of the measured eKE of the multiphoton ionisation of Xe (black circles) to its $^2P_{\frac{3}{2}}$ state at 249.7 nm as a function of distance from the liquid jet. The solid line is the fit of Equation 2.5.9 to the data. This example has a streaming potential of $\Phi_{\text{stream-pot}=-0.24}$ eV and $V_0 = 0.085$ eV .

The eKE points of the Xe transition are plotted as a function of the distance from the interaction region, see Figure 2.5.9. These points are then fit to with the following equation:

$$\Phi(x) = \Phi_{\text{stream-pot}} \frac{\ln(\frac{2Y+x}{x})}{\ln(\frac{2(Y+x)-r}{r})}. \tag{2.5.8}$$

$\Phi_{\text{stream-pot}}$ is the streaming potential, Y is the distance between the skimmer and the ionisation point, x is the distance between the liquid micro-jet and the ionisation point, r is the radius of the liquid micro-jet. The following equation describes the measured kinetic energy:

$$\text{eKE}_{measured} = \text{eKE}_{\text{true}} - \Phi_{\text{stream-pot}} \frac{\ln(\frac{2Y+x}{x})}{\ln(\frac{2(Y+x)-r}{r})} - V_0. \tag{2.5.9}$$

eKE_{true} is the electron kinetic energy in the absence of any fields and V_0 is the vacuum level offset. The vacuum level offset is another essential parameter that must be considered. It describes the difference in vacuum level between the solution and the spectrometer. Equation 2.5.9 is fit to the measured Xe peaks at different distances from the skimmer to extract the vacuum level offset and the streaming potential. We aim to have a completely flat potential in the interaction region.

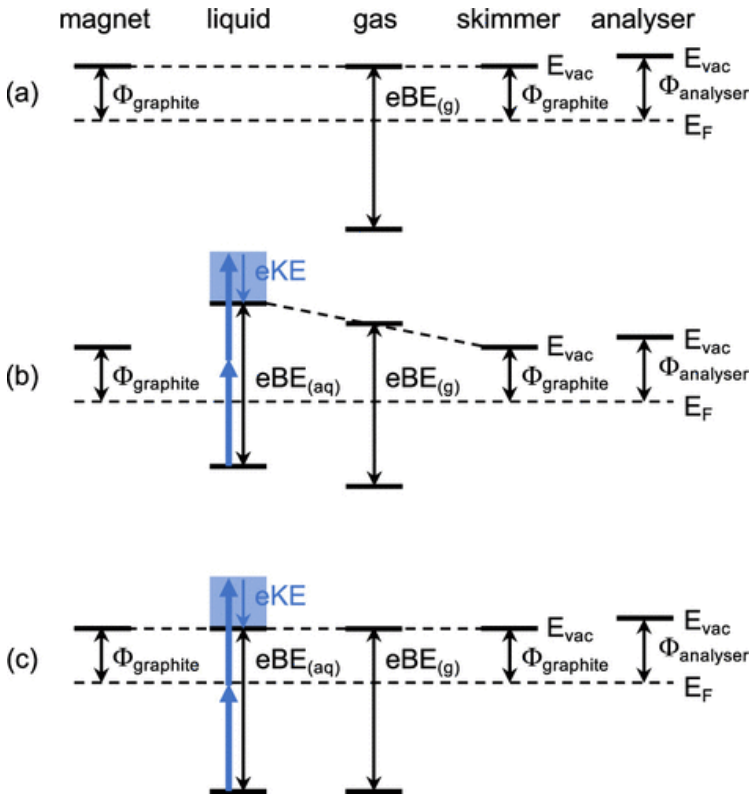

Figure 2.5.10: Schematic energy level diagram illustrating the relative electronic energy levels of all components within the UCL spectrometer. In the interaction region of the spectrometer the skimmer, magnet, liquid-jet nozzle and catcher are all coated in graphite. $\Phi_{graphite}$ and $\Phi_{analyser}$ represent the work functions, E_F is the Fermi level, and E_{vac} is the vacuum level. (a) Example without the liquid jet present. There is no potential gradient between the magnet and the skimmer. (b) The liquid jet is added resulting in a potential gradient due to the different work function of the jet. In this example the photoelectrons will be accelerated. (c) Adjusting the flow rate or concentration of electrolytes in the liquid flattens the potential between the magnet and the skimmer. Reproduced from Ref. [42].

The vacuum level offset is another parameter that is determined from Equation 2.5.9. It represents the difference between the measured kinetic energy of Xe and its true value. The offset (V_0) represents the energy difference between the conduction band and the vacuum level. During experimental measurements, the measured photoelectron kinetic energies are likely to vary due to the difference in vacuum level between the solution and the analyser, [69]. Figure 2.5.10 (b) illustrates how introducing the liquid jet into the interaction region creates a potential gradient.

2.5.6 Overall Operation

This sections described the method of operating the UCL liquid micro-jet photoelectron spectrometer. At atmospheric pressure the micro-jet assembly is put into the source region of the chamber. Typically the liquid micro-jet would then be aligned with the recirculating catcher but, the motors during the time of experiments were broken. Therefore, a cold trap was used instead. If the catcher was in use, the liquid microjet nozzle would be moved using the motors, and the CMOS camera (iDS, UI-3250LE-M) would be used to visualise its position. The cold trap is removed from the vacuum chamber to ensure the liquid stream is coming through centrally and if not it is adjusted by manually moving the motors. Next liquid nitrogen is place under the cold trap to freeze the liquid collected in it. The source region of the chamber can now be pumped down. To do this the backing line to the source turbo is closed and then the roughing line is opened. With the cold-trap assembly this can be opened quickly as turbulence of the jet will not misaligned it from the cold trap but, if the catcher is in use this should be done very gradually. Once the pressures in the TOF and detector regions reach $\sim 10^{-2}$ mbar the three gates valves for the TOF and detector region can be opened. The pressures in the TOF and detector region fall to between $\sim 10^{-5}$- 10^{-6} mbar. The pressure in the source region will now be around $\sim 10^{-1}$ mbar. Next the cold trap in the source region is filled with liquid nitrogen, lowering the pressure to $\sim$ 3x10^{-3} mbar. Now the roughing line in the source region is closed and the turbo backing line is then opened. After this the source region gate valve can be opened and the pressure will reach between $\sim 3 \times 10^{-4}$-8×10^{-5} mbar. Now the liquid micro-jet is then aligned to ensure that the laser light hits the liquid in the laminar flow region, located 3-4 mm below the nozzle tip. This distance can be measured using the CMOS camera software, which is employed for viewing inside the interaction region. The magnet is moved to the far position and the streaming potential is now recorded. The streaming potential is minimised until its amplitude is less than 0.1 eV. Once an optimal streaming potential is achieved photoelectron spectra can be recorded. The photoelectron signal is recorded by a double-stack microchannel plate (MCP) coupled to a phosphor screen

(Beam Imaging Solutions BOS-25-IDA-CH-MS). Originally, the signal would then be amplified (20V/V, Ortec 9326) although this was found to be no longer needed for the work presented in Chapter 5 of this thesis, after the MCPs were replaced. The photoelectron signal is then digitised (Keysight U5309A) and the electron arrival times are recorded relative to the laser trigger. This is interfaced with a custom LabVIEW software used to record and visualise the photoelectron spectra.

2.5.7 Time-resolved Experiments

Developing the capability for time-resolved experiments was an important development that was undertaken for the work that is presented in this thesis. This section will describe the method of time-resolved photoelectron spectroscopy (TRPES). The current design uses two UV light pulses and employs a standard pump-probe technique. The pump pulse is provided by an OPA (Coherent OPerA Solo) and is tuneable from $\sim$ 235-2600 nm. The 266 nm probe pulse generated by THG. The beam line is shown in detail in Section 2.5.1. The pump pulse promotes the population from the ground electronic state to a higher lying one. This is followed by the probe pulse, with a known time delay with respect to the pump pulse. The probe initiated the photodetachment and then spectra are recorded at multiple pump-probe time delays to build a picture of the dynamics of the system of interest. First, the pump and probe laser pulses have to be spatially and temporally overlapped on the lamina region of the liquid jet. Temporal overlap is roughly found by the use of a fast photodiode and a 500 MHz Oscilloscope (LeCroy Waverunner 6050A). This allows the observation of temporal overlap within 200 ps, as the maximum resolution is 200 ps/division. In order to precisely find where on the delay stage the pump and probe pulses overlap, known as time zero (t_0), a scan of the delay stage can be performed. Figure 2.5.11 displays an example phenolate data set with the normalised photoelectron signal plotted as a function of pump-probe delay time. The delay stage provides a method to delay the probe pulse with respect to the pump pulse by increasing the distance the probe has to travel. A Newport (DL125) 125 mm stage is used. Typically, time zero would be found, and the instrument function determined by multiphoton ionisation of Xe with 249.7 nm. However, there was no access to

Xe at the time of recording this data.

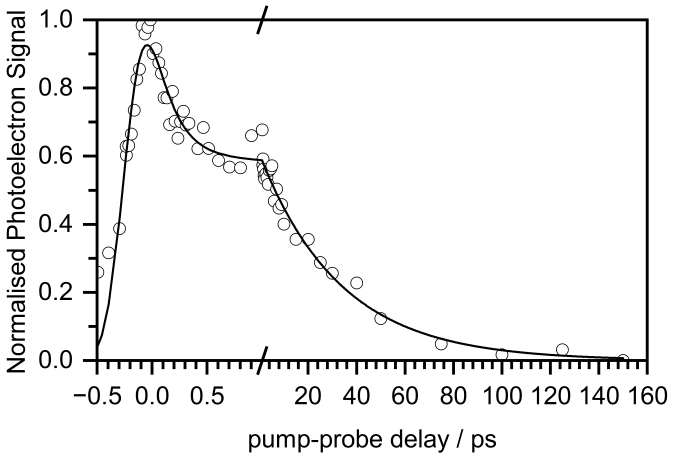

Figure 2.5.11: Pump-probe delay scan following 1+1 resonant detachment of 0.1 mM Phenolate with 1.8 mM NaOH. λ_{pump} =287 nm and λ_{probe} =267 nm. Experimental data (circles) and the biexponential fit (solid line) to the experimental data are plotted.

2.6 Summary

This chapter presented two experimental techniques employed to recorded the experimental data in Chapters 3, 4, 5 and 6: transient absorption spectroscopy and liquid microjet photoelectron spectroscopy. It described the principles of each technique, their operation, and how to interpret the resulting data. The first half of the chapter focused on transient absorption spectroscopy, beginning with an introduction to the femtosecond laser system. It then described how the transient absorption data presented in Chapters 3, 4 and 6 was recorded. The steps for processing the raw data and the subsequent analysis were then discussed. Next, liquid microjet photoelectron spectroscopy was discussed, starting with a detailed focus on the experimental apparatus and its components. The process of calibrating the spectrometer was then covered, including how to account for the streaming potential and vacuum level offset. The chapter also described the standard operating procedures for recording data on the UCL liquid microjet photoelectron spectrometer. Finally, the steps for setting up the time-resolved liquid microjet photoelectron spectroscopy experiments, a capability developed during this thesis, were explained.

Chapter 3

The Wavelength Dependent Mechanism of Phenolate Photooxidation in Aqueous Solution

Phenolate photooxidation plays a crucial role in various biological processes, yet the exact mechanism of electron ejection has been a subject of debate. In this Chapter, we discuss the results of a comprehensive study that combines femtosecond transient absorption spectroscopy, with high-level quantum chemistry calculations carried out by Anton Boichenko under the supervision of Anastastia Bochenkova (Moscow State University), and liquid microjet photoelectron spectroscopy measurements performed by William Fortune to explore the photooxidation dynamics of aqueous phenolate across a range of excitation wavelengths. These wavelengths span from the onset of the S_0–S_1 absorption band to the peak of the S_0–S_2 band. Our findings indicate that for wavelengths $\geq$ 266 nm, electron ejection occurs from the S_1 state on two timescales into the continuum associated with a contact pair where the $PhO^{\cdot}$ radical is in its ground electronic state. Conversely, for wavelengths $\leq$ 257 nm, electron ejection also occurs into continua associated with contact pairs containing electronically excited $PhO^{\cdot}$ radicals. These excited contact pairs exhibit faster recombination times compared to those with $PhO^{\cdot}$ radicals in their ground state.

3.1 Motivation

The phenolate anion is a common molecular motif present in many chromophores, and thus can be used as a model system for larger and more complex biological systems. Examples of these systems are chromophores including the photoactive yellow protein (PYP) and the green fluorescent protein (GFP). [8–10, 23, 70]

After photoexcitation with ultraviolet (UV) light, the phenolate anion in aqueous solution undergoes photooxidation to form a solvated electron ($e^-_{(aq)}$) and the neutral phenoxy radical, $PhO^{\cdot}$. UV induced photooxidation is known to be important in various photochemical reactions, such as the photocycle in fluorescent proteins; however it has also been reported to have deleterious effects, such as photodamage in DNA. [41, 71, 72]

Photooxidation of molecules in aqueous solution is also of fundamental interest. The solvated electron represents the simplest form of an anion in solution, since it doesn't have any nuclear structure. Within a living cell, the water exposed to UV radiation will undergo ionisation and produce solvated electrons and OH radicals also making the dynamics of solvated electrons important in biochemical processes [73].

Phenol has been studied extensively in both the gas- and condensed-phases [74, 75]. After photoexcitation at a 267 nm, which directly populates the first $\pi\pi^*$ state (S_1), the timescale for electron ejection in aqueous phenol is reported to be on a nanosecond timescale. [75, 76]. This process results in the loss of both an electron and a proton. However, it is important to note the dissociative $\pi\sigma^*$ state is absent in phenolate, and the timescale of electron ejection is drastically different at the same excitation wavelength. Oliver *et al.* also followed the dynamics after photoexcitation at 200 nm and the photoproducts (solvated electron and phenoxy radical) However, a key difference was noted in the formation timescales; following 200 nm photoexcitation, the electrons are ejected immediately.

Prior to the work in this chapter, there were three transient absorption (TA) studies of aqueous phenolate. The earliest work used picosecond-TA spectroscopy [77] and followed the dynamics after photoexcitation at 265 nm. The peak of the S_0-S_1 absorption band is 287 nm and therefore, 265 nm lies very high in the first absorption band (Figure 3.2.1). The electron ejection in these experiments was observed to be on a timescale shorter than the experimental resolution of 27 ps. This study was followed by a femtosecond-TA [78] study using a photoexcitation wavelength of 266 nm, similar to the picosecond-TA study. Time-resolved fluorescence spectra were also reported, and the S_1 ($^1\pi\pi^*$), as fluorescence lifetime was established to be 22 ps; this lifetime was then fixed for the TA analysis. S_1 ($^1\pi\pi^*$) will now be referred to as S_1. After a detailed global target analysis, two timescales for electron ejection were obtained. The first, 1.4 ps, was assigned to be from vibrationally hot S_1. The second involved the vibration relaxation (VR) of the excited state population to the vibrationally cold S_1 state, and subsequent ejection of the electron on a timescale of 22 ps. These timescales differ significantly from the typical timescale of charge transfer to solvent (CTTS) reactions of inorganic anions, in which the timescale is usually less than 100 fs. A subsequent, and the most recent study also made use of femtosecond-TA [79]. However unlike the earlier two measurements, the photoexcitation wavelength was 257 nm. This lies between the first and second absorption (S_0-S_1 and S_0-S_2, where S_2 is the $^2\pi\pi^*$ state) bands. The observed dynamics differ significantly, with only one timescale observed for electron ejection, occurring on an approximately 500 fs. This is comparable to the timescale of CTTS observed from iodide [79]. This study concluded, that only rapid electron ejection is observed. The authors assigned it to be from vibrationally hot S_1, and proposed that the rapid electron ejection was out-competing VR from hot to cold S_1. A Marcus picture for electron ejection was then proposed, in which electron tunnelling occurred through the barrier between the S_1 state and the radical-electron contact pair. This mechanism would be highly sensitive to excitation energy, and at 257 nm they assume to the be close to the top of the barrier as the tunnelling out-competes the VR, see Figure 3.1.1. This finally brings us on to the motivation for our study.

We were curious why it had not been considered that a higher lying electronic excited state could be involved in the electron ejection, considering especially that 257 nm is directly between the S_0-S_1 and S_0-S_2 and even on the rising edge of the S_0-S_2 transition (Figure 3.2.1) . We also thought it could be plausible that the dark state, $n\pi^*$ (S_{1n}), could be involved and have resulted in the significantly faster timescale.

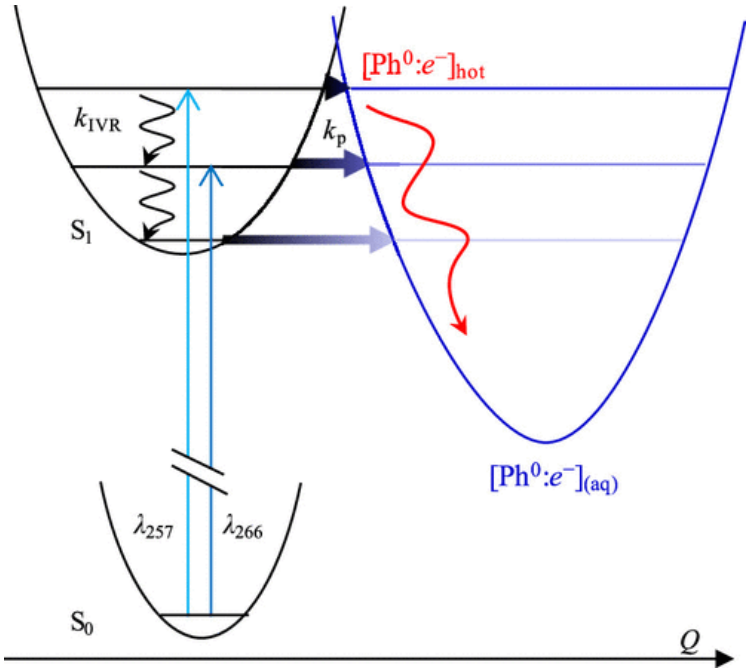

Figure 3.1.1: Reprinted (adapted) with permission from [79]. Copyright 2019 American Chemical Society. Schematic energy level diagram plotted along the solvent coordinate for phenolate in aqueous solution. Diagram illustrates internal vibrational relaxation (k_{IVR}) is out competed by the electron tunneling (k_p) with higher excitation energy.

3.2 Experimental Details

3.2.1 Steady-state Absorption Characterisation

The ground steady-state absorption spectrum of aqueous phenolate is well characterised in the literature [78]. Our spectrum is displayed in Figure 3.2.1. The 20 mM phenolate solution was prepared from phenol ($\geq$ 99 %, Sigma-Aldrich) and used without any further purification. The phenol was deprotonated by adding a small volume of concentrated sodium hydroxide until the solution was at pH 13. The pH of the solution was confirmed with a pH meter (Hanna Instruments, HI-2020). UV-vis spectra of aqueous phenolate were recorded using a PerkinElmer LAMBDA 365 spectromphotometer.

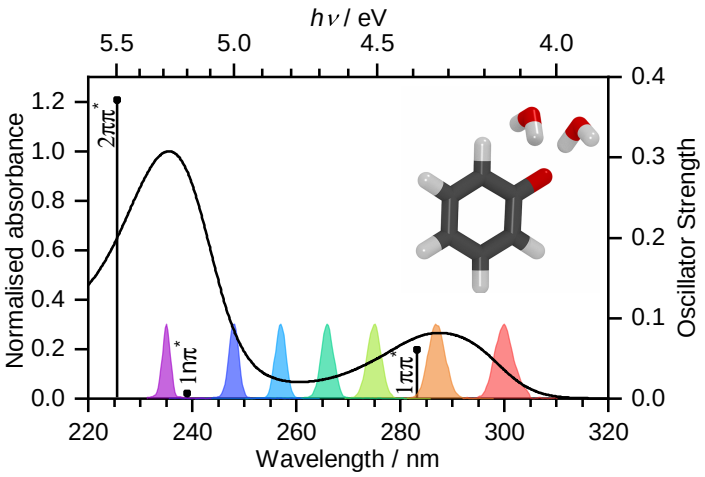

Figure 3.2.1: Reproduced from Ref. [80] with permission from the Royal Society of Chemistry. UV-vis spectrum of 20 mM aqueous phenolate. The absorbance is normalised to be between 0 and 1. Gaussians indicate the spectral profiles of the femtosecond pump pulses employed in the TA experiments. Vertical lines mark XMCQDPT2/SA(7)-CASSCF(10,8)/(aug)-cc-pVDZ//EFP calculated vertical excitation energies (VEEs) with heights proportional to oscillator strengths. Inset: PBE0/(aug)-cc-pVDZ//EFP(1043) equilibrium geometry of $PhO^- + 2H_2O$.

3.2.2 Transient-Absorption Spectroscopy

TA spectra were obtained, using the experimental set-up outlined in Chapter 2. Briefly, TA spectra were recorded following photoexcitation at seven pump wave-

lengths. These were: 300 nm, 287 nm, 275 nm, 266 nm, 257 nm, 248 nm and 235 nm, see Figure 3.2.1. These were chosen to span excitation from the low energy side of the S_0-S_1 band to the peak of the S_0-S_2 absorption band.

Each pump wavelength was generated from the optical parametric amplifier (OPA) and then attenuated at the sample using a neutral density filter to achieve a pulse energy of approximately 100 nJ. This Chapter presents experiments that both use the Visible and UV probes that have a combined probing region of 350-720 nm. The relative polarisations the pump and probe beams were set to be at the magic angle (54.7°). This ensures effects from rotations are not measured. A Harrick flow cell with a 100 μm spacer was used and the 20 mM solution was flowed constantly through it at a speed of 10 mL min^{-1}, using a liquid diaphragm pump (KNF, Simdos 02). Sample preparation was described above in Section 3.2.1.

3.3 Results and Discussion

This section presents data from TA spectroscopy experiments with supporting Liquid-Jet photoelectron spectroscopy (LJ-PES) measurements. The LJ-PES data were recorded by William Fortune, the visible TA data were recorded by Dr Julia Davies with assistance from the author of this thesis, and the UV TA data were recorded by the author, with assistance by Dr Julia Davies. Supporting calculations were carried out by Anton Boichenko from Anastasia Bochenkova's group at the University of Moscow. The remainder of this section beings with a discussion of visible probe TA data and analysis, and then progresses on to the the UV probe TA data.

3.3.1 Visible Probe Transient Absorption Spectroscopy

TA spectra were recorded following photoexcitation at seven pump wavelengths. Figure 3.3.1 (top) displays the 480-720 nm TA spectrum of aqueous phenolate after excitation at the peak of the S_0-S_1 absorption band, 287 nm. Two excited state absorptions (ESA) can be observed. The first is present at very early pump-probe delay times, and can be observed at 500 fs (pink) and 1 ps (red). It is a broad band

absorption with a maximum around 540 nm. This feature can be assigned to an excited state absorption of the S_1 state of phenolate. This is supported by the work of Chen *et al.* [78], as seen in Figure 3.3.2. They confirmed this assignment because the lifetime of the ESA matches the fluorescence lifetime of phenolate. Complementary XMCQDPT2/SA(15)-CASSCF(10,8)/(aug)-cc-pVDZ//EFP calculations also support this assignment as they determined the brightest vertical transition from S_1 corresponds to excitation to S_3 and is located at 547 nm with an oscillator strength of 0.07.

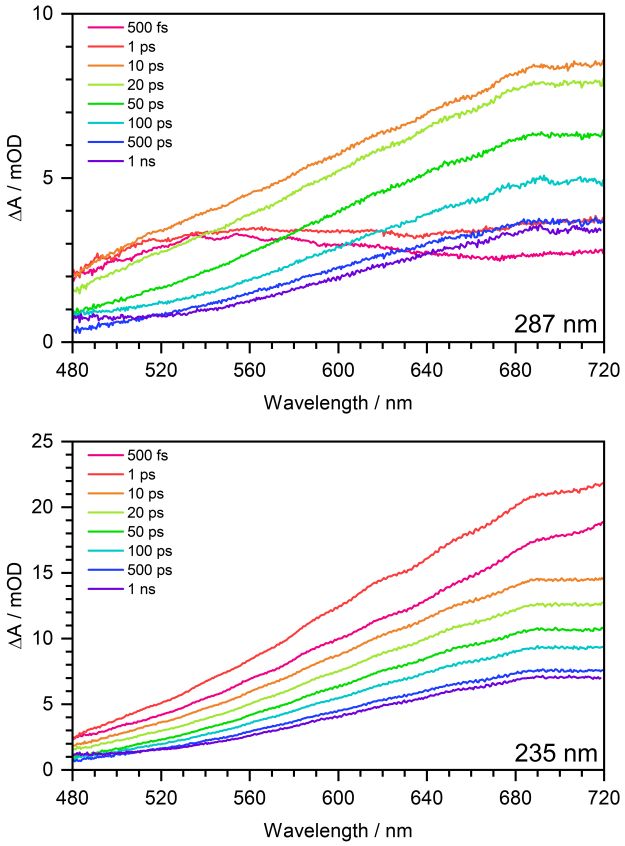

Figure 3.3.1: Reproduced from Ref. [80] with permission from the Royal Society of Chemistry. 480-720 nm TA spectra 20 mM phenolate at pump-probe delay times displayed in the legend. Spectra were recorded following photoexcitation at 287 nm (top) and 235 nm (bottom). The broad absorption centred around 540 nm is attributed to the S_1 state of phenolate and the broadband absorption at 700 nm is the $e^-_{(aq)}$.

The second ESA is a broadband absorption centred around 700 nm. The spectral profile evolves between 1 and 10 ps to reveal this feature. After 10 ps, this broadband feature is observed to decay during our 1 ns experimental window. This broadband absorption is characteristic of a spectrum associated with the solvated electron. Chen *et al.* [78] confirmed this assignment by adding the electron scavenger NO_3^-, and observing the depletion of the signal.

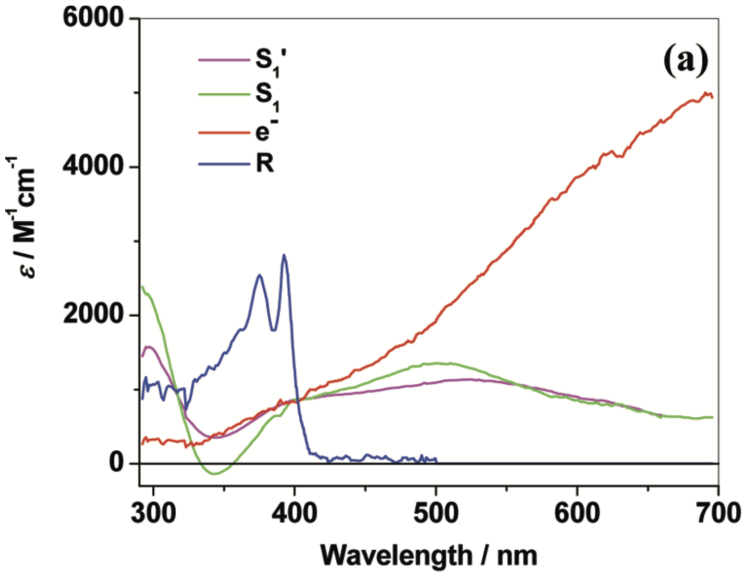

Figure 3.3.2: Figure showing the absorption spectrum of 90 mM aqueous phenolate solution of each component of the TA spectrum, obtained from global target analysis. Red is the spectrum of the solvated electron, blue is the spectrum of the phenoxy radical, purple is the spectrum of vibrationally hot S_1, and green is the spectrum of vibrationally cold S_1. Reprinted with permission from [78]. Copyright 2011 American Chemical Society.

Now the discussion will turn to the TA spectrum obtained from the peak of the S_1-S_2 absorption at 235 nm. As seen in Figure 3.3.1 (bottom), there is no evidence here of the S_1 ESA at 540 nm, and the only transient absorption signature observed is associated with $e^-_{(aq)}$. The $e^-_{(aq)}$ transient absorption signal is observed to reach its absorbance maxima after around 1 ps, which is significantly faster than the approximately 10 ps seen following photoexcitation at the peak of S_1. The signal then begins to decay, again on a timescale quicker than the equivalent observed following direct populating of S_1.

Having looked at the spectra at each extreme the discussion will now focus on the wavelengths between the peaks of the two excited states, starting with the pump wavelengths associated with the S_1 state. The TA spectra are displayed in Figure 3.3.3.

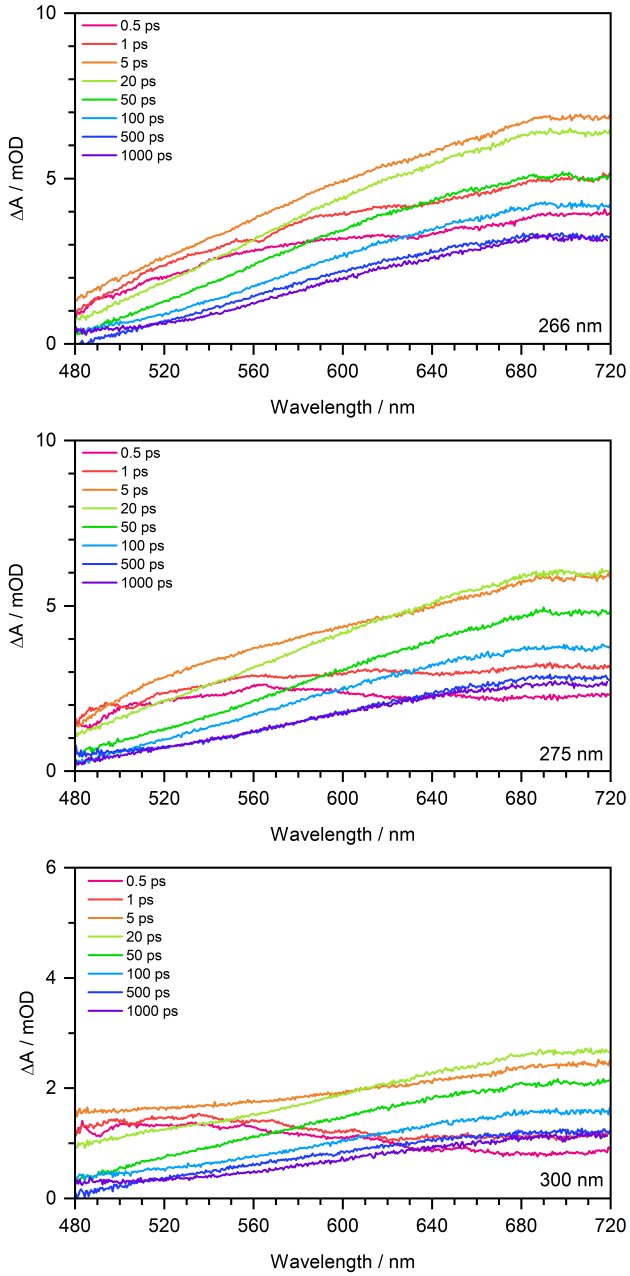

Figure 3.3.3: Reproduced from Ref. [80] with permission from the Royal Society of Chemistry. TA spectra with a probing region of 480-720 nm 20 mM phenolate at pump-probe delay times displayed in the legend. Spectra are following photoexcitation at 266 nm (top), 275 nm (middle) and 300 nm (bottom). All spectra display a broad absorption centred around 540 nm that is attributed to the S_1 state of phenolate and the broadband absorption at 700 nm is the $e^-_{(aq)}$

In all three spectra, 300 nm (top), 275 nm (middle) and 266 nm (bottom), the same two ESA features are observed. The ESA associated with S_1 is present at early

times and the spectrum evolves to reveal the $e^-_{(aq)}$, which decays over the rest of the 1 ns experimental window.

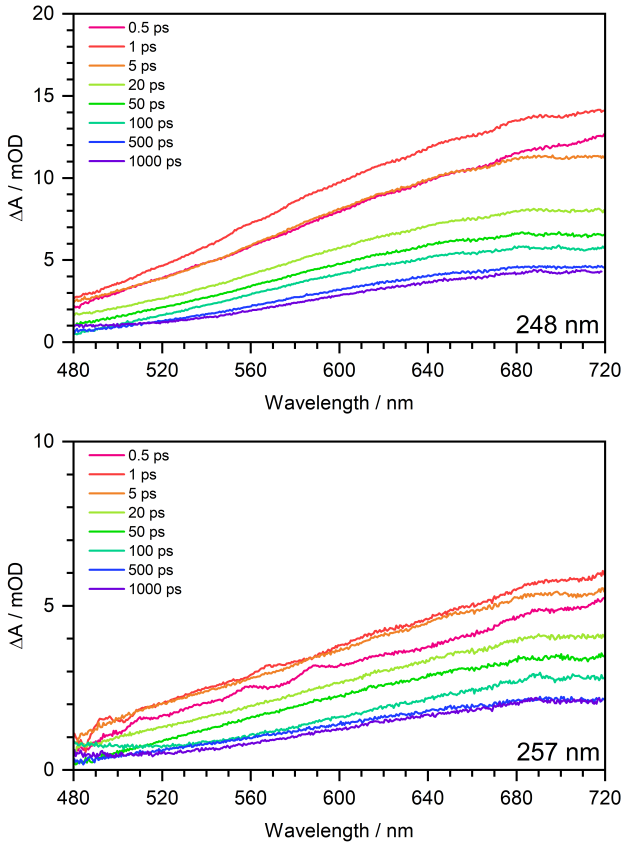

Figure 3.3.4: Reproduced from Ref. [80] with permission from the Royal Society of Chemistry. TA spectra with a probing region of 480-720 nm 20 mM phenolate at pump-probe delay times displayed in the legend. Spectra are following photoexcitation at 248 nm (top) and 257 nm (bottom). All spectra display only one broad absorption centred around at 700 nm assigned to the $e^-_{(aq)}$

As seen in Figure 3.3.4, the 248 nm and 257 nm TA spectra appear similar to the TA spectrum associated recorded following photoexcitation at S_2, 235 nm (Figure 3.3.1). There is no evidence of the S_1 ESA that would be centered around 540 nm. Instead, a rapid sub-ps growth of the $e^-_{(aq)}$ electron signal is observed and then the signal decays over the next 1 ns.

After examining the seven TA spectra and observing that each either contains one or two ESA features, the kinetic traces were plotted at two important probe

wavelengths 540 nm and 700 nm. These represent, respectively, the ESA of S_1 and absorption of $e^-_{(aq)}$. The kinetic traces were normalised and plotted for each pump wavelength and displayed in Figure 3.3.5.

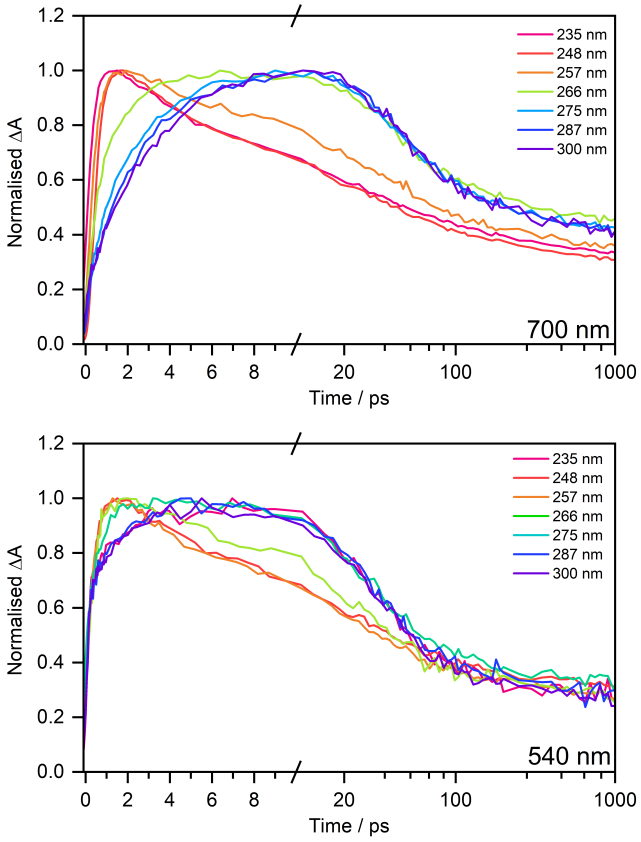

Figure 3.3.5: Reproduced from Ref. [80] with permission from the Royal Society of Chemistry. Normalised kinetic traces for probe wavelengths of 700 nm (top) and 540 nm (bottom). Kinetic traces are plotted at each pump wavelength. Scale is linear from 0-10 ps and is logarithmic from 10-1000 ps.

Starting with the kinetic trace at the probe wavelength of 700 nm, which illustrates the dynamics of the $e^-_{(aq)}$, it is seen after photoexcitation of S_2 ($\lambda \leq 248$ nm), a rapid sub-ps formation of the electron is observed and within the first few picoseconds the signal starts to decay. It is also apparent that, compared to photoexcitation of S_1 ($\lambda \geq 266$ nm), it is much faster. The $e^-_{(aq)}$ formation at pump wavelengths corresponding to photoexcitation of S_1 clearly has two timescales associated with it. Moreover, the decay timescales related to the $e^-_{(aq)}$ transient signal also differ: those

from photoexcitation of S_2 photoexcitation start to decay within a few picoseconds, whereas, following photoexcitation of S_1, the $e^-_{(aq)}$ transient signal only begins to decay after around 10 ps.

Looking at the 540 nm kinetic traces, it can be seen that they are almost identical to the 700 nm kinetic traces following photoexcitation with $\lambda \leq 248$ nm. Contrasting this, after photoexcitation with $\lambda \geq 266$ nm, the transient absorption appears instantaneously and after approximately 5 ps begins to resemble the 700 nm traces.

Photoexcitation with 257 nm (Figure 3.3.4 (bottom)), the same pump wavelength used by Tyson *et al.*, does not exactly yield kinetic traces associated with just S_1 or S_2 photoexcitation. In the 700 nm kinetic trace, is a component with a slower decay between 2-20 ps. The characteristics are similar to the relaxation dynamics associated with S_1 photoexcitation. Between 100-1000 ps, the trace also could contain the slower contribution that is characteristic of S_1 photoexcitation. This contribution of S_1 is confirmed by comparing the kinetic traces at probe wavelengths of 515 nm and 680 nm, see Figure 3.3.6.

A kinetic fitting procedure was performed on each data set to extract time-constants associated with each pump wavelength. First, we will look at the data associated with the pump wavelength of 257 nm (Figure 3.3.6). The 515 nm probe is used to isolate the S_1 contribution, since it is on the blue edge of the S_1 ESA is should have less signal contribution from $e^-_{(aq)}$. The 680 nm kinetic trace is used to describe the $e^-_{(aq)}$ transient absorption. This probe wavelength remains consistent for the rest of the analysis discussed in this chapter. At longer pump-probe delay times, there will only be a contribution from $e^-_{(aq)}$ to the data because S_1 will have decayed entirely. Since the reported fluorescence lifetime [78] is around 22 ps, normalising the data to 500 ps (Figure 3.3.6 (top)) highlights there is an early time contribution from S_1, otherwise the dynamics of both kinetic traces are the same. Normalising the data

to the maximum (Figure 3.3.6 (bottom)) also shows a deviation in the dynamics of each trace at longer pump-probe delay times, confirming a contribution from S_1. The rapid, sub-ps rise time of the 680 nm transient absorption, indicates rapid electron formation and resembles the dynamics at the peak of S_2 (Figure 3.3.1). Therefore, due to 257 nm lying between both the S_0-S_1 and S_0-S_2 absorption band, it has dynamical contributions from both electronic states. This makes it difficult to quantitatively analyse the data due to the contribution of two different excited states, therefore no further fitting was carried out for this data set.

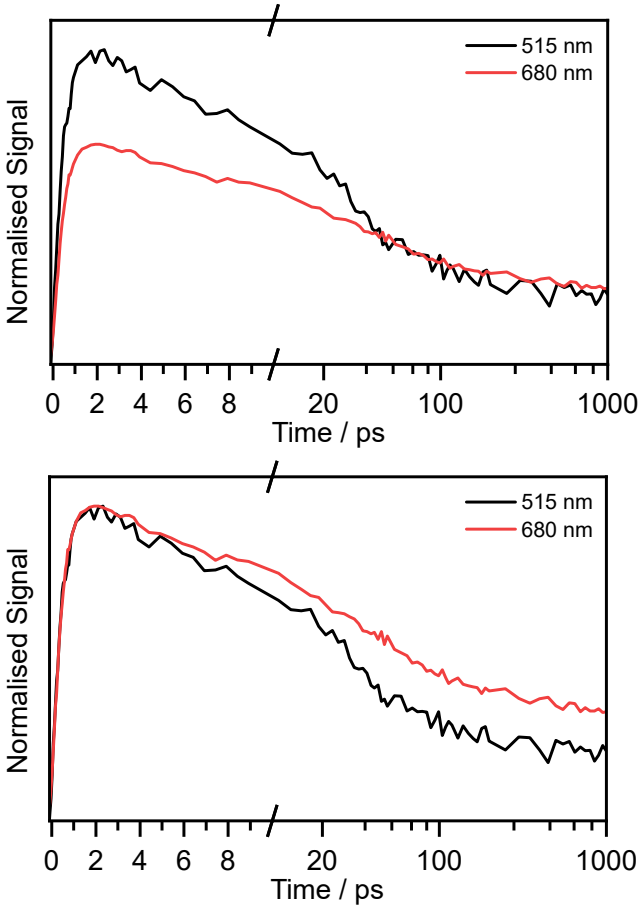

Figure 3.3.6: Reproduced from Ref. [80] with permission from the Royal Society of Chemistry. Data displayed is following photoexcitation with 257 nm and probing wavelengths 515 nm (black) and 680 nm (red). Top: Kinetic traces are normalised to 500 ps. Bottom: Kinetic traces are normalised to the maximum. These plots illustrate the dynamics at probe wavelength 515 nm differ from the dynamics at 680 nm. This would suggest there is a significant contribution from S_1 present. The fast rise time at 680 nm suggests that there is a significant contribution from S_2 . Therefore, we conclude that at 257 nm both S_1 S_2 are photoexcited.

All other datasets were fit using two different procedures. First, we will discuss the method used to obtain time constants from the data associated with S_1 ($\lambda \geq 266$ nm) photoexcitation. The method of fitting data sets associated with S_1 photoexcitation was adapted from the method reported in the work of Chen *et al.* [78]. Figure 3.3.7 shows the data analysis procedure for the data following photoexcitation at 287 nm, the peak of S_1.

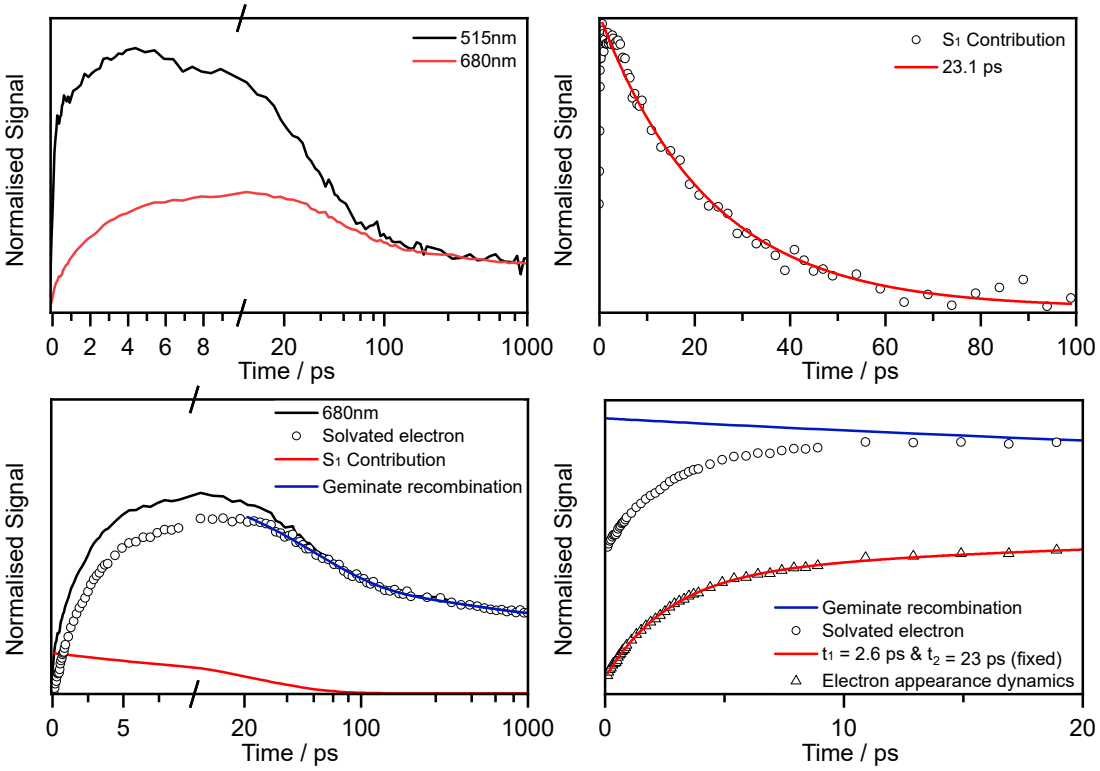

Figure 3.3.7: Reproduced from Ref. [80] with permission from the Royal Society of Chemistry. Data analysis conducted at the pump wavelength of 287 nm, at the peak of the first absorption band. Top left shows kinetic traces at 515 nm (S_1 and 680 nm ($e^-_{(aq)}$) normalised to 500 ps. At 500 ps there will only be a contribution from the solvated electron. The difference is then plotted in the top right figure. This difference is the isolated S_1 signal with the solvated electron subtracted. Fitting a exponential gives a time constant of 23.1 ps, representing the S_1 lifetime. The bottom left figure displays the S_1 contribution (red) with it's instantaneous lifetime set to match that of the 680 nm trace (black). The S_1 contribution is then subtracted from the 680 nm trace to isolate the signal from the solvated electron (black circles). The solvated electron is then fitted from 20-1000 ps with a biexponential to describe the geminate recombination (blue). The bottom right shows the fit of the geminate recombination (blue) interpolated to early time. This is subtracted from the solvated electron signal, to isolate the appearance dynamics (black triangles). The appearance dynamics are the fitted to with a biexponential with the second time constant fixed to be the S_1 lifetime.

The top left plot in Figure 3.3.7 displays kinetic traces from probe wavelengths at 515 nm and 680 nm normalised to 500 ps, where the only contribution to the signal is the transient $e^-_{(aq)}$. Taking the difference between these normalised kinetic traces subtracts the $e^-_{(aq)}$ contribution, and leaves us with a kinetic trace only describing S_1. The difference is displayed in the top right plot of Figure 3.3.7. Fitting an

exponential to this will provide a time constant that can be associated with the lifetime of the phenolate S_1 state. This was found to be 23 $\pm$ 1 ps, similar to the fluorescence lifetime of 22 $\pm$ 2 ps recorded by Chen *et al.* [78] Once the time constant representing the S_1 lifetime was extracted, it was then used to remove the S_1 contribution from the 680 nm trace (see bottom left of Figure 3.3.7). Making the instantaneous lifetime of the exponential modelling the decay of S_1 equivalent to the instantaneous lifetime of the 680 nm kinetic trace, allows the kinetic trace only containing a contribution from the solvated electron to be subtracted. The geminate recombination dynamics of the solvated electron were modelled by fitting a biexponential [78] from 20-1000 ps. Starting from 20 ps allows the early-time formation and thermalisation dynamics to have minimal impact. The bottom right plot of Figure 3.3.7 shows the recombination dynamics (blue) extrapolated to time zero, thus assuming recombination of the radical and electron is not immediate. This can then be used to extract the electron appearance dynamics, by removing the contribution of the recombination from the solvated electron signal. The resulting kinetic trace, describing the electron appearance dynamics was best described by a biexponential function. Fitting a monoexponential yielded a single time constant of 3.6 ps. The timescale of the electron appearance dynamics relates to the depopulation of the precursor state of the $e^-_{(aq)}$ [78, 81]. This 3.6 ps timescale is short, like the lifetime of the S_1 state, although the timescale do not match well with the S_1 lifetime which is 23 ps. With the biexponential describing the appearance dynamics better Chen *et al.* [78] concluded there were two precursor states and that the second with a shorter lifetime. They then confirmed this assignment by global analysis and assigned the two precursor states as vibrationally hot and vibrationally cold S_1. Thus, when fitting the biexponential the longer time constant was fixed to be the extracted lifetime of the S_1 state. This fitting procedure was repeated for every other pump wavelength associated with S_1 and the resulting fits can be seen in Figs. 3.3.8, 3.3.9, 3.3.10 and time constants in Table 3.3.1.

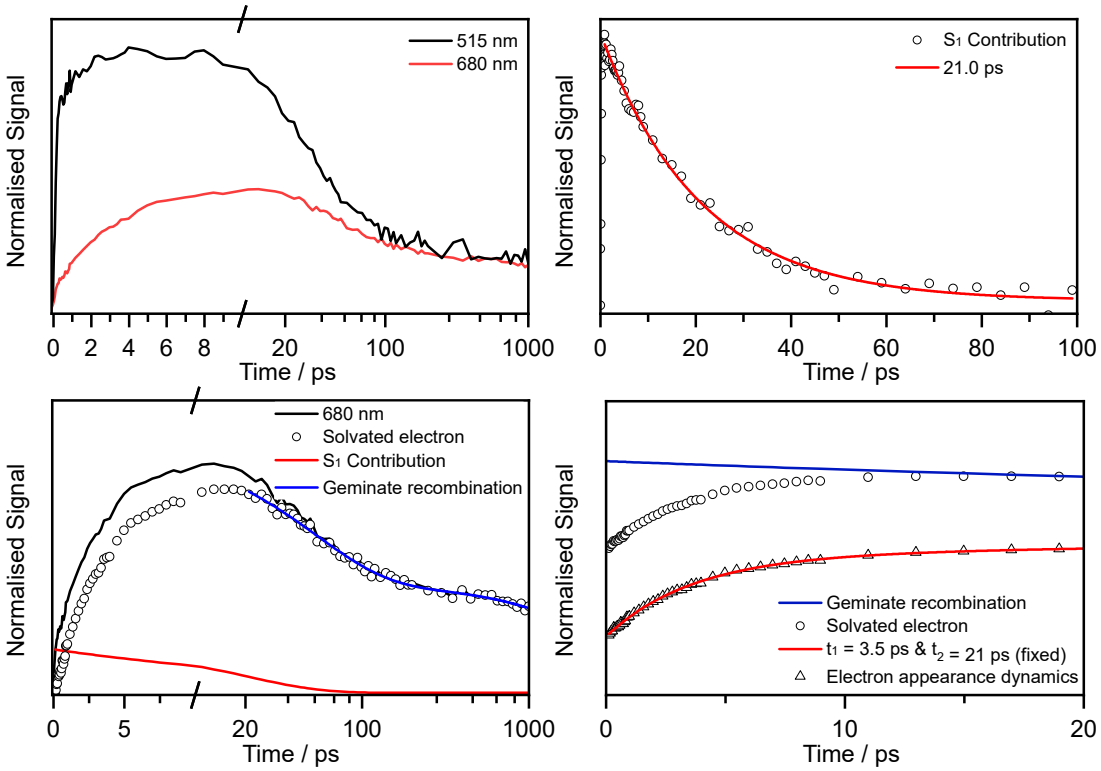

Figure 3.3.8: Reproduced from Ref. [80] with permission from the Royal Society of Chemistry. Figure displays the data analysis conducted at the pump wavelength of 300 nm, on the low energy side of the first absorption band. Top left shows kinetic traces at 515 nm (S_1 and 680 nm ($e^-_{(aq)}$) normalised to 500 ps. At 500 ps there will only be a contribution from the solvated electron. The difference is then plotted in the top right figure. This difference is the isolated S_1 signal with the solvated electron subtracted. Fitting a exponential gives a time constant of 23.1 ps, representing the S_1 lifetime. The bottom left figure displays the S_1 contribution (red) with it's instantaneous lifetime set to match that of the 680 nm trace (black). The S_1 contribution is then subtracted from the 680 nm trace to isolate the signal from the solvated electron (black circles). The solvated electron is then fitted from 20-1000 ps with a biexponential to describe the geminate recombination (blue). The bottom right shows the fit of the geminate recombination (blue) interpolated to early time. This is subtracted from the solvated electron signal, to isolate the appearance dynamics (black triangles). The appearance dynamics are the fitted to with a biexponential with the second time constant fixed to be the S_1 lifetime

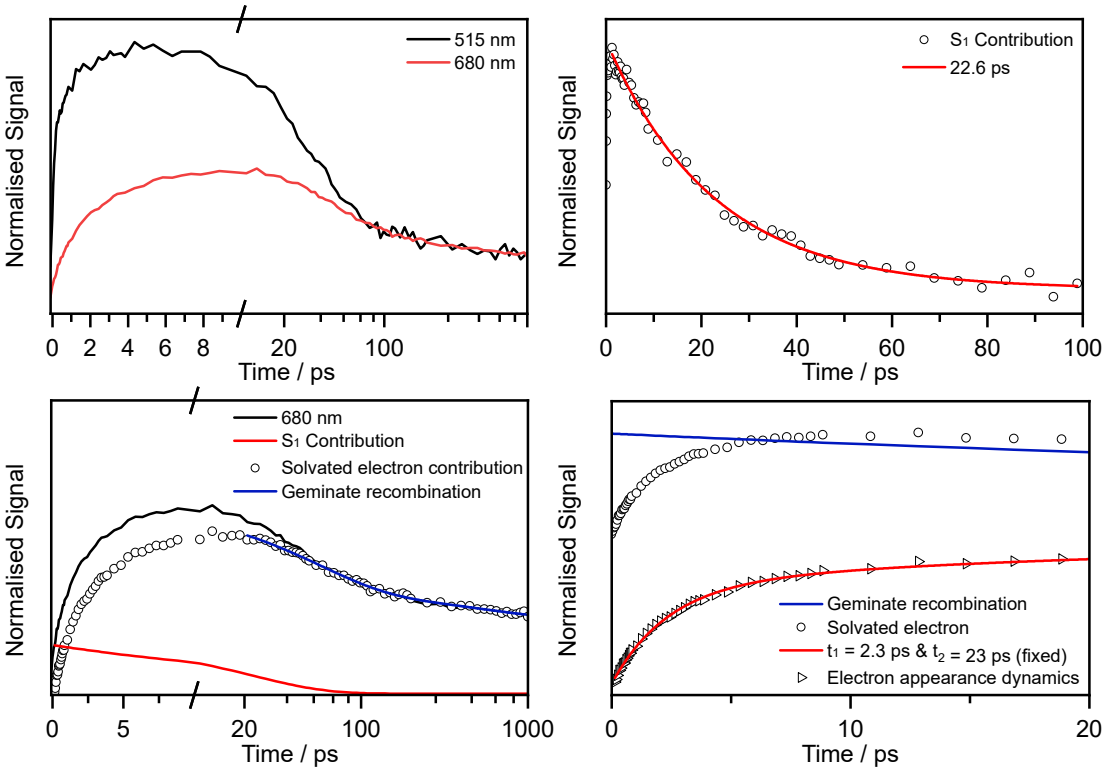

Figure 3.3.9: Reproduced from Ref. [80] with permission from the Royal Society of Chemistry. Figure displays the data analysis conducted at the pump wavelength of 275 nm, on the high energy side of the first absorption band. Top left shows kinetic traces at 515 nm (S_1 and 680 nm ($e^-_{(aq)}$) normalised to 500 ps. At 500 ps there will only be a contribution from the solvated electron. The difference is is then plotted in the top right figure. This difference is the isolated S_1 signal with the solvated electron subtracted. Fitting a exponential gives a time constant of 23.1 ps, representing the S_1 lifetime. The bottom left figure displays the S_1 contribution (red) with it's instantaneous lifetime set to match that of the 680 nm trace (black). The S_1 contribution is then subtracted from the 680 nm trace to isolate the signal from the solvated electron (black circles). The solvated electron is then fitted from 20-1000 ps with a biexponential to describe the geminate recombination (blue). The bottom right shows the fit of the geminate recombination (blue) interpolated to early time. This is subtracted from the solvated electron signal, to isolate the appearance dynamics (black triangles). The appearance dynamics are the fitted to with a biexponential with the second time constant fixed to be the S_1 lifetime

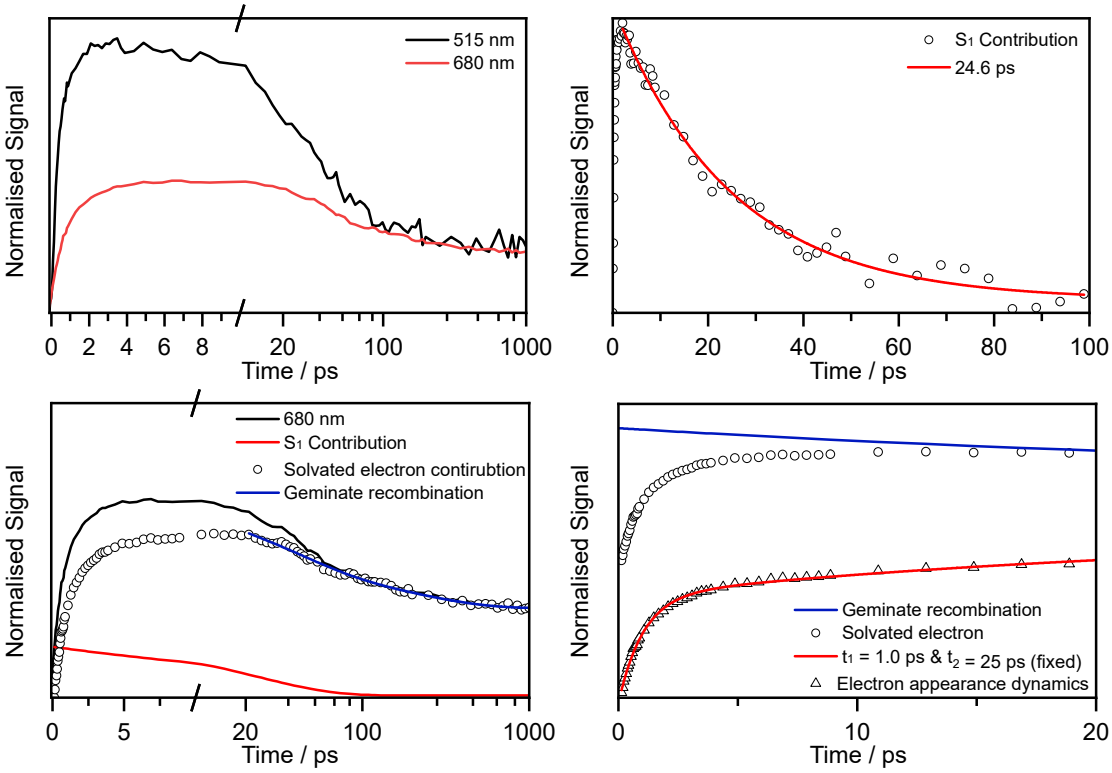

Figure 3.3.10: Reproduced from Ref. [80] with permission from the Royal Society of Chemistry. Figure displays the data analysis conducted at the pump wavelength of 266 nm, on the high energy side of the first absorption band. Top left shows kinetic traces at 515 nm (S_1 and 680 nm ($e^-_{(aq)}$) normalised to 500 ps. At 500 ps there will only be a contribution from the solvated electron. The difference is is then plotted in the top right figure. This difference is the isolated S_1 signal with the solvated electron subtracted. Fitting a exponential gives a time constant of 23.1 ps, representing the S_1 lifetime. The bottom left figure displays the S_1 contribution (red) with it's instantaneous lifetime set to match that of the 680 nm trace (black). The S_1 contribution is then subtracted from the 680 nm trace to isolate the signal from the solvated electron (black circles). The solvated electron is then fitted from 20-1000 ps with a biexponential to describe the geminate recombination (blue). The bottom right shows the fit of the geminate recombination (blue) interpolated to early time. This is subtracted from the solvated electron signal, to isolate the appearance dynamics (black triangles). The appearance dynamics are the fitted to with a biexponential with the second time constant fixed to be the S_1 lifetime

In comparison to the kinetic traces associated with wavelengths that photoexcite S_1, those associated with photoexcitation S_2 have minimal, if any contribution from S_1. This is illustrated by looking at 235 nm (Figure 3.3.11). In the top left plot of Figure 3.3.11, kinetic traces from 515 nm and 680 nm transient absorption are normalised

to 500 ps. The traces are very similar, therefore any contribution from S_1 is minor and can be excluded from fitting. The 680 nm kinetic trace convoluted with the IRF was fitted to four exponential. The exponents had lifetimes of 0.36 ps (rise), 6.6 ps (decay), 99 ps (decay) and ∞ (decay). The infinite lifetime is included to account for the solvated electron signal remaining beyond our experimental window of 1 nm. The same procedure was followed for the 248 nm data (see Figure 3.3.12).

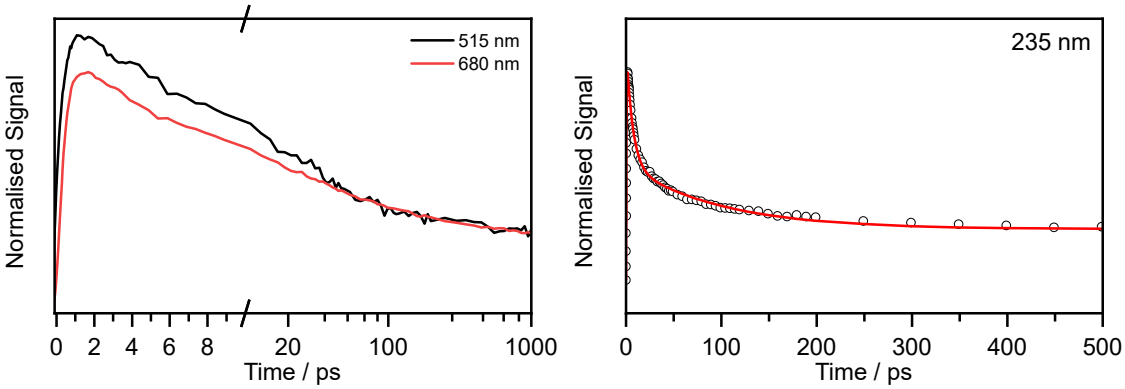

Figure 3.3.11: Reproduced from Ref. [80] with permission from the Royal Society of Chemistry. Left: Data displayed is for a pump wavelength of 235 nm and probe wavelengths of 515 nm and 680 nm. Kinetic traces are normalised to 500 ps. As the dynamics at both probe wavelengths are so similar, the contribution from S_1 is minor and can be excluded from the fitting. Right: Four exponential functions convoluted with the IRF. The exponents have lifetimes: 0.36 ps (rise), 6.6 ps (decay), 99 ps (decay) and ∞ (decay). The infinite lifetime is included to account for the solvated electron signal beyond our experimental window.

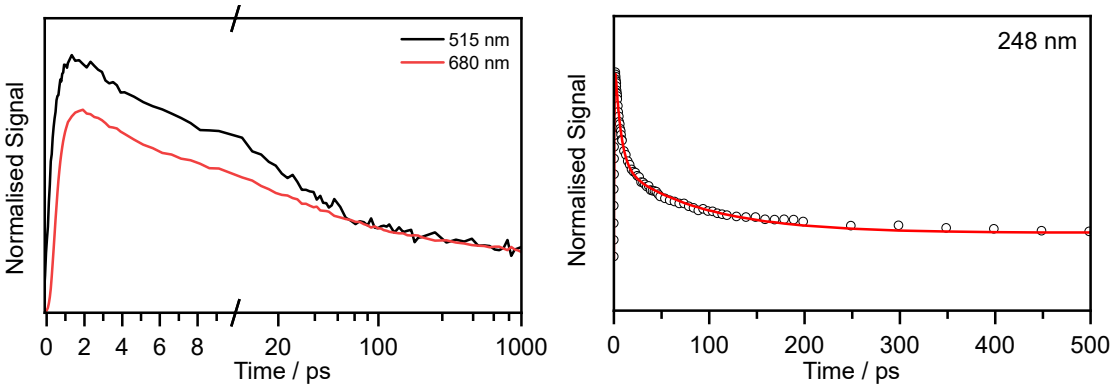

Figure 3.3.12: Reproduced from Ref. [80] with permission from the Royal Society of Chemistry. Left: Data displayed is for a pump wavelength of 248 nm and probe wavelengths of 515 nm and 680 nm. Kinetic traces are normalised to 500 ps. The dynamics at both probe wavelengths are very similar, and although there is clearly more contribution from S_1 at this wavelength compared to 235 nm (above), it is still minor and can be excluded from the fitting. Right: Four exponential functions convoluted with the IRF. The exponents have lifetimes: 0.42 ps (rise), 6.2 ps (decay), 90 ps (decay) and ∞ (decay). The infinite lifetime included to account for the solvated electron signal beyond our experimental window.

We can progress on to interpreting what these time constants tell us. Table 3.3.1 summarises the time constants obtained from fitting to each data set.

Table 3.3.1: Time constants (in ps) obtained from fits to the kinetic traces (displayed in Figs. 3.3.7-3.3.12) τ_{instr} is the instrument response function. $\tau_{S'_n \rightarrow e^-(aq)}$ is the timescale of $e^-_{(aq)}$ formation from directly populated 'hot' S_1 or S_2 and $\tau_{S_1 \rightarrow e^-(aq)}$ is the timescale of $e^-_{(aq)}$ formation from 'cold' S_1. τ_{r1}, τ_{r2} and τ_{r3} describe the decay of $e^-_{(aq)}$ by geminate recombination.

λ_{pump} / nm	τ_{instr}	$\tau_{S'_n \rightarrow e^-(aq)}$	$\tau_{S_1 \rightarrow e^-(aq)}$	τ_{r1}	τ_{r2}	τ_{r3}
235	0.4	0.4 ± 0.2		6.6 ± 0.4	99 ± 9	> 1000
248	0.4	0.4 ± 0.3		6.2 ± 0.5	90 ± 8	> 1000
266	0.4	1.02 ± 0.03	25 ± 1	36 ± 6	210 ± 50	
275	0.4	2.3 ± 0.1	23 ± 0.8	54 ± 5	550 ± 300	
287	0.3	2.6 ± 0.1	23 ± 1	50 ± 3	490 ± 200	
300	0.3	3.5 ± 0.1	21 ± 0.8	52 ± 4	> 1000	

Following photoexcitation at S_1 ($\lambda \geq 266$ nm), $e^-_{(aq)}$ are formed on two timescales: few-picosecond and ~ 20 ps timescales. These timescales, as previously discussed,

relate to the depopulation of the precursor states of the solvated electron, namely vibrationally hot and vibrationally cold S_1 respectively. This is consistent with the earlier study by Chen *et al.* [78] following photoexcitation at 266 nm, who assigned time constants of 1.4 ps and 20 ps to be fast electron ejection from vibrationally hot S_1, and vibrational relaxation followed by slower electron ejection from vibrationally cold S_1.[78]. It is worth noting that, following photoexcitation at 300 nm, close to the S_0-S_1 origin, the slow electron emission was found to occur on a timescale of 21 ± 0.8 ps, which is in excellent agreement with to the fluorescence lifetime of S_1 measured by Chen *et al.*[78] (22 ± 2 ps).

In contrast to the dynamics observed following photoexcitation of S_1, following photoexcitation of S_2 ($\lambda \leq 248$ nm), $e^-_{(aq)}$ are formed more rapidly, on a sub-picosecond timescale. There is no evidence here of the slower timescale for electron formation associated with emission from vibrationally cold S_1. This observation is similar to that reported by Tyson *et al.*, following photoexciation at 257 nm [79].

Following photoexcitation to S_1 ($\lambda \geq 266$ nm), the $e^-_{(aq)}$ decay (as already discussed) is best described by a bi-exponential, with the time constants τ_{r1} and τ_{r2}. Geminate recombination is known to be a very complex process, but fitting a bi-exponential is a reasonable estimate of the timescales [78]. Our τ_{r1} timescales obtained from our fits are of the same order of magnitude as the faster recombination timescale observed in the earlier 266 nm TAS measurement reported by Chen *et al.* (50 ps) [78]. Within our 1 ns experimental window, the $e^-_{(aq)}$ transient absorption signal does not decay to zero. Interestingly, we found that after photoexcitation at 300 nm, the second timescales associated with geminate recombination was 1 ns, i.e. larger than our experimental window, and thus has a large associated error.

Following photoexcitation to S_2 (248 and 235 nm), the decay of the $e^-_{(aq)}$ transient absorption is best described by three exponentials, with the time constants τ_{r1}, τ_{r2} and τ_{r3}. τ_{r3} accounts for the population that lives beyond our 1 ns experi-

mental window. The other two timescales, τ_{r1} and τ_{r2}, are noticeably shorter than the equivalent timescales observed following photoexcitation of S_1. The noticeably shorter timescales associated with recombination, following photoexcitation of S_2, suggests that the phenoxy radical could be formed in a higher lying electronically excited state, leading to a lower kinetic energy electron. In this scenario, recombination would be expected to be faster since the lower kinetic energy electron would not travel so far away from its radical partner, following photoexcitation at 248 and 235 nm compared to photoexcitation at $\lambda \geq 266$ nm.

Interestingly, following photoexcitation of S_1, the faster timescale associated with the $e^-_{(aq)}$ formation from vibrationally hot S_1 decrease after photoexcitation with shorter pump wavelengths (Table 3.3.1). The decreases is most noticeable at 266 nm, which could suggest there is a contribution from the S_2 state. However, the longer time dynamics follow those associated with S_1 (Figure 3.3.5). Therefore, this faster time constant is attributed to increasing vibrational energy in S_1. In the Marcus picture suggested by Tyson *et al.* [79] the rate of tunnelling from S_1 to form the contact pair of the $e^-_{(aq)}$ and the phenoxy radical is very sensitive to the barrier height (see Figure 3.1.1). Therefore, the noticeable decrease in time constant between 275 nm and 266 nm could suggest that 266 nm excitation lies close to the top of the barrier.

Due to the simultaneous photoexcitation of S_2 and S_1, following photoexcitation at 257 nm, it is extremely difficult to separate the contributions form both electronic excited states.

3.3.2 Liquid Microjet Measurements

To support the conclusions drawn from the TAS experiments 1+1 resonance enhanced liquid jet-photoelectron spectroscopy experiments of aqueous phenolate were conducted [80]. Following photoexcitation, at 285 nm, 266 nm, 257 nm, and 236 nm. This was to determine which photodetachment continua were accessible from the different electronic excited states of aqueous phenolate. Figure 3.3.13 dis-

plays the four photoelectron spectra from these experiments. All the liquid microjet photoelectron spectra presented in this Chapter were recorded by William Fortune.

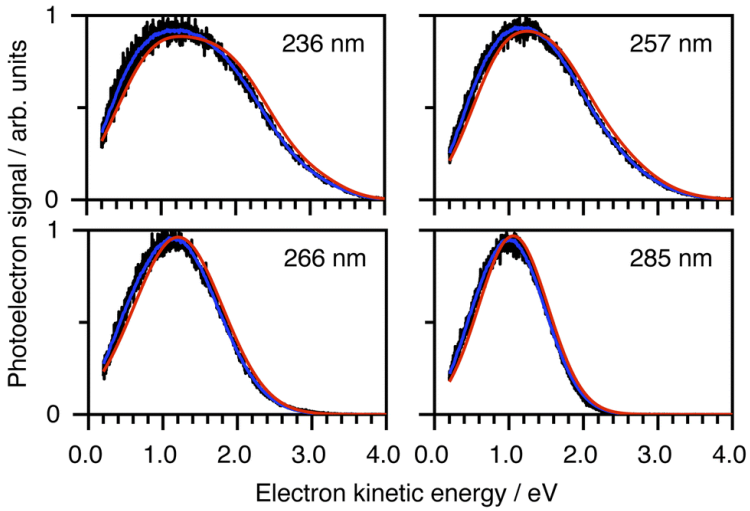

Figure 3.3.13: Reproduced from Ref. [80] with permission from the Royal Society of Chemistry. Resonance enhanced $1+1$ photodetachment of aqueous phenolate following excitation at 236 nm, 257 nm, 266 nm, and 285 nm (blacK). The blue lines are a fit to the experimental data (black). The red lines are the retrieved true photoelectron spectra corrected for inelastic scattering.

The spectral lineshapes of the photoelectron spectra following 287 nm and 266 nm photoexcitation can be reproduced by fitting a single Gaussian. This was assigned to be S_1-D_0 detachment. The photoelectron spectra following excitation at higher photon energies (236 nm and 257 nm) are more complicated. Their lineshapes could only be reproduced by fitting a linear combination of Gaussian functions. It is likely the photoelectron spectrum following 236 nm excitation, has contribution from resonance enhance photodetachment *via* S_2 to D_0, D_{1n}, and D_2. Although, ultrafast internal conversion to S_1 cannot definitively be ruled out. It is likely in line with the observations from the TAS data that the 257 nm photoelectron data has contribution from S_1 and S_2. Assignments of the accessible photodetachment continua are supported by calculation, present in detail in the following section.

3.3.3 Calculations

XMCQDPT2/SA(15)-CASSCF(9,8)/(aug)-cc-pVDZ//EFP calculations were carried out by Anton Boichenko under the supervision of Anastastia Bochenkova

(Moscow State University). Figure 3.3.14 summarises the results from the high-level quantum chemistry calculations.

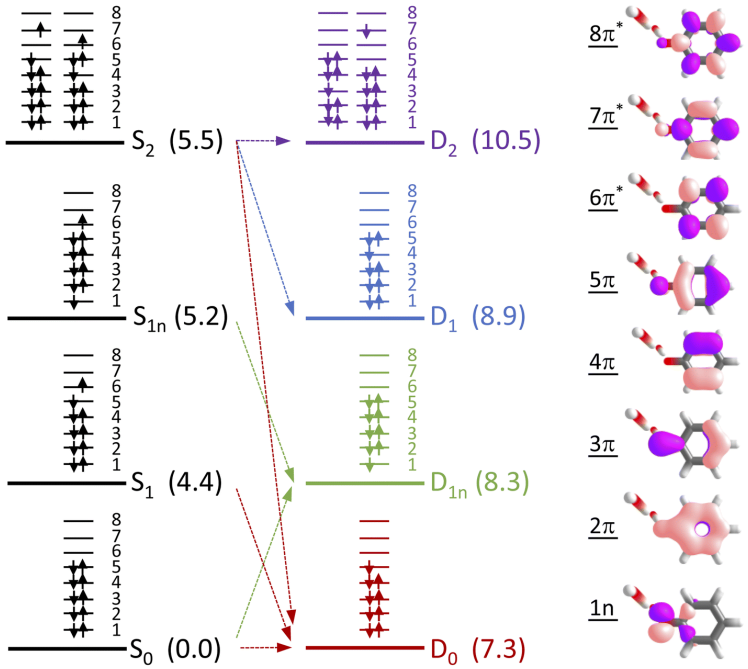

Figure 3.3.14: Reproduced from Ref. [80] with permission from the Royal Society of Chemistry. The electronic configuration of phenolate's four lowest lying singlet and lowest doublet electronic states of the corresponding neutral radical in aqueous solution. Number in brackets are from XMCQDPT2/SA(7)-CASSCF(9,8)/(aug)-cc-pVDZ//EFP and XMCQDPT2/SA(7)-CASSCF(10,8)/(aug)-cc-pVDZ//EFP calculations in eV. These are the vertical excitation and vertical detachment energies calculated relative to S_0. Arrows indicate the allowed detachment processes. Natural SA(7)-CASSCF(10,8) are also displayed.

Using Koopmans' arguments we were able to determine that S_0 is most likely to detach to D_0 and D_{1n}, S_1 to D_0, S_{1n} to D_{1n}, and S_2 to D_0, D_1, and D_2. This clearly supports that the photoelectron spectra following $1+1$ resonance enhanced photodetachment *via* 285 nm (S_1 absorbance maximum) and 266 nm (high energy edge of S_1) correspond to S_1 to D_0 detachment. The situation is more complicated for the 236 nm and 257 nm with D_0, D_1, and D_2 all being accessible after photoexciting S_2.

The binding energy of the solvated electron is known to be 3.7-3.8 eV [26, 52]. It is highly likely that the S_1 state is coupled to the solvated electron continuum to the D_0 state of the phenoxy radical, and S_2 to the D_0 and D_1 states of the phenoxy

radical. Tyson *et al.* previously suggested that it was not possible to access the D_1 continuum following 257 nm excitation. However, based on our calculations and the second vertical detachment energy reported by Ghosh *et al.* [22], we can confirm that it is indeed possible. They identified the first neutral radical states from the ground electronic state to have detachment energies of 7.1 $\pm$ 0.1 eV and 8.5 $\pm$ 0.1 eV, respectively. Therefore, suggesting it is possible from S_2 to access the D_1 following 257 nm excitation. The calculations confirm that at higher photon energies it is possible to access the continuum of the radical in higher lying excited states. Thus, supporting the faster recombination timescales observed in TAS measurements being a result of the recombination being the solvated electron being coupled to a continuum of the corresponding neutral radical in a higher-lying electronic state.

3.3.4 Ultraviolet Probe Transient Absorption Spectroscopy

To confirm that upon photoexcitation of S_2 the phenoxy radical is formed in a higher lying electronic state we recorded TA spectra with an UV probe, see Figure 3.3.15. These spectra were recorded following photoexcitation at the peak of the S_0-S_1 (287 nm) and S_0-S_2 (235 nm) absorption bands. From the work of Chen *et al.* [78] we know the formation of the phenoxy radical in its D_0 state can be observed between probe wavelengths of 330 - 400 nm. As observed in Fig 3.3.15 (top) the TA spectrum following photoexcitation at 287 nm shows a structured ESA, the same as those observed by Chen *et al.* following photoexcitation at 266 nm. In addition to this ESA, following photoexcitation at 235 nm (Figure 3.3.15 (bottom)) an additional peak is observed around 427 nm, and a shoulder on the longer wavelength edge of the peak around 400 nm. These additional features are present instantaneously and decay on a sub-picosecond timescale. Similar transient absorptions were observed for aqueous phenol following excitation at 200 nm and the small peak at 427 nm was assigned to the phenol radical cation.[75]. Our assignment is consistent with the earlier observation [75] as of phenol at 200 nm could generate the phenoxy radical in the D_1 state. Oliver *et al. observed the intermediate of the phenol radical cation being formed and then it rapidly deprotonates to form the*

phenoxy radical. We attribute this weak absorption around 427 nm to absorption of an excited electronic state of the phenoxy radical, slightly red-shifted from the absorption band attributed to the radical in its ground electronic state. This is supported by XMCQDPT2/SA(15)-CASSCF(9,8)/(aug)-cc-pVDZ//EFPcalculations carried out by our collaborator Dr. Anastasia V. Bochenkova from the University of Moscow. These calculations showed the most bright $D_1 \rightarrow D_3$ vertical transition is located at 411 nm with an oscillator strength of 0.06. This is red-shifted from the most bright $D_0 \rightarrow D_2$ transition located at 386 nm with an oscillator strength of 0.1.

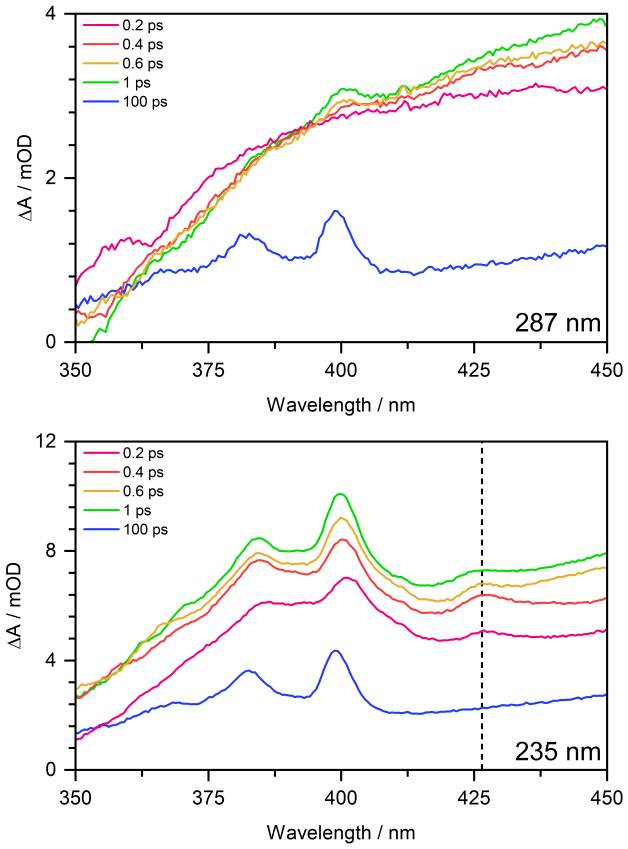

Figure 3.3.15: Reproduced from Ref. [80] with permission from the Royal Society of Chemistry. 350–450 nm transient absorption spectra of 20 mM aqueous phenolate at displayed pump-probe delays following photoexcitation at 287 nm (top) and 235 nm (bottom). The dashed vertical line highlights the peak at 427 nm attributed to the $D_1 \rightarrow D_3$ absorption of the phenoxy radical.

The results from these UV-TA spectra reinforce our conclusion that the quicker recombination times are due to the phenoxy radical being formed in a higher lying electronic state. The corresponding electrons would have less kinetic energy, thus explaining the faster timescales for geminate recombination.

3.4 Conclusions

To conclude, the wavelength dependent mechanism of phenolate photooxidation has been unravelled. Upon systematic photoexcitation at many pump wavelengths we have been able to understand the mechanism and resolve the recent controversy in the literature [77–79]. We found that following photoexcitation at $\lambda \geq 266$ nm, electron ejection occurs from the S_1 state in to the continua associated with the [Phe$^{\cdot}$(D_0):$e^-_{(aq)}$]. The timescales we obtained support the assignments in the previous study by Chen *et al.* and are associated with electron ejection from vibrationally hot and cold S_1. Following photoexcitation at $\lambda \leq 248$ nm, we found that electron ejection occurs from a higher lying electronic excited state the S_2 ($^2\pi\pi^*$) into a continua where the phenoxy radical is also formed in an electronically excited state, [Phe$^{\cdot}$ (D_1):$e^-_{(aq)}$]. The geminate recombination was found to be faster in contact pairs compared to those where the radical was in its ground electronic state. We also found that, following photoexcitation at 257 nm both S_1 and S_2 are simultaneously populated and the dynamics observed are associated with both excited states. We propose the significantly quicker timescale for electron ejection observed following photoexcitation at this wavelength, is associated with electron ejection for S_2, like that observed following photoexcitation at 235 nm and 248 nm. Figure 3.4.1 presents a schematic energy level diagram summarising our findings.

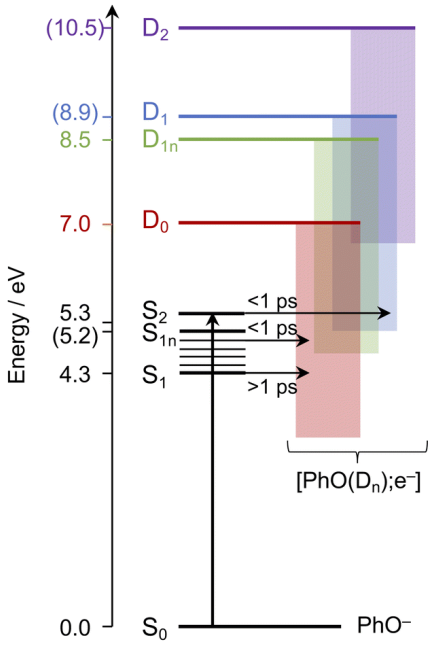

Figure 3.4.1: Reproduced from Ref. [80] with permission from the Royal Society of Chemistry. Schematic energy level diagram illustrating the two possible photooxidation pathways and their corresponding timescales, following photoexcitation of S_1, S_{1n}, and S_2 of aqueous phenolate. Numbers in brackets are the calculated vertical detachment and vertical excitation energies, present in Figure 3.3.14. Numbers in brackets are the absorbance maxima fron the steady-state absorption spectrum (Figure 3.2.1) and vertical detachment energies from UV (D_0 and x-ray (D_{1n} liquid microjet photoelectron spectroscopy measurements. [22, 54] The horizontal arrows represent the coupling to the corresponding solvated electron continua (shaded rectangles) with the timescales of the process.

Chapter 4

Methyl Substitution on the Mechanism of Phenolate Photooxidation in Aqueous Solution

The systematic modification of chromophores can be an excellent method to study their photochemistry. This chapter presents the results of a study of three methyl-substituted phenolates (2-, 3-, and 4-methylphenolate) aimed at understanding the implications the substituent has on the photooxidation mechanism. We combined femtosecond transient absorption spectroscopy experiments carried out in our lab with the results of time-correlated single photon counting (TCSPC) experiments carried out by Shivalee Dey under the supervision of Stephen Bradforth (University of Southern California), and high-level quantum chemistry calculations carried out by Anton Boichenko under the supervision of Anastastia Bochenkova (Moscow State University), to investigate the photooxidation dynamics of methyl-substituted aqueous phenolates following excitation at the maxima of their S_0-S_1 absorption bands. We found methyl-substitution in the *ortho* and *meta* positions lead to faster timescales for electron recombination, while in the *para* position the recombination dynamics were similar to those of phenolate.

4.1 Motivation

As discussed in Chapter 3 the photooxidation mechanism in phenolate has been studied as a model system, for larger biological chromophores. The photoactive yellow (PYP) and the green fluorescent (GFP) proteins are both examples of photoactive proteins whose chromophores share a common molecular motif of phenolate. They are known to undergo photooxidation reactions following photoexcitation with ultraviolet (UV) light. [82] This chapter presents the results of a study investigating three substituted phenolates (2-, 3-, and 4-methylphenolate), in an attempt to understand the effect of substituting a methyl group at different positions on the aromatic ring on the ultrafast dynamics after UV photoexcitation. Figure 4.1.1. displays the chemical structure of each of the molecules studied in this week. Studying the aromatic building blocks of photoactive chromophores, such as phenolate, allows us to develop a fundamental understanding of the relationship between the structure of a molecule and the photoinduced dynamics. Systematic modifications can be made to these chromophores to alter their photochemistry and are an excellent way to explore their fundamental behaviour. The photochemistry of phenolate has been studied extensively by both experimental and theoretical methods. Previously, there have been four transient absorption spectroscopy studies in aqueous solution [77–80], all of which have been described in detail in Chapter 3. From the prior work an extensive understanding has already been developed of the ultrafast dynamics of phenolate and we wish to build upon this, by studying 2-, 3-, and 4-methylphenolate (2MP, 3MP, and 4MP). In the case of DNA, the methylation of cytosine, to form 5-methylcytosine, plays an important role in epigenetic mechanisms in various biological processes [83, 84]. Methylation of the cytosine has been associated with mutations from the formation of cyclobutene pyrimidine dimers after UV irradiation [84–87]. The absorption spectrum in aqueous solution after cytosine methylation of nucleosides is significantly red-shifted. In aqueous solution the lifetime of the first $\pi\pi^*$ state is also noticeably increased. The potential energy surface of this state contains a minimum that is separated from the crossing region with the ground state that is not present in cytosine. This explains the longer

lifetime of the first $\pi\pi^*$ state [88]. It is clear from this work the significance of the addition of methyl group to the excited state dynamics of molecules and the implications this can have in biology, and thus the major importance of understanding the implications methylation has on a molecules photophysics. The photostability of molecules is enhanced by anharmonic coupling, as this leads to the delocalisation, and therefore distribution, of internal energy [89–91]. A study by Timber *et al.* [92] compared the rates of intramolecular vibrational redistribution (IVR) of *m*-fluorotoluene and *p*-fluorotoluene and found that *m*-fluorotoluene experiences IVR much quicker than *p*-fluorotoluene. Davies *et al.* [89] also observed that *m*-fluorotoluene undergoes more rapid IVR than *p*-flourotoluene.

To the best of our knowledge, the work presented here is the first systematic study of the effect of methylation on photooxidation dynamics. Previously, two studies have investigated 4-methylphenolate (4MP) in aqueous solution using flash photolysis and transient absorption spectroscopy, conducted by Feitelson *et al.* and Ichino *et al.*, respectively [93, 94]. Both studies observed a spectral structure similar to that of phenolate, particularly around 400 nm. In phenolate, as discussed in Chapter 3 these structured bands where assigned to the absorption of the radical, the same assignment given in 4MP. These structured bands are also observed in tyrosine. We will explore the influence that the substitution of a methyl group has (on the 2, 3, and 4 positions) of phenolate as a model system for photooxidation reactions in biological chromophores.

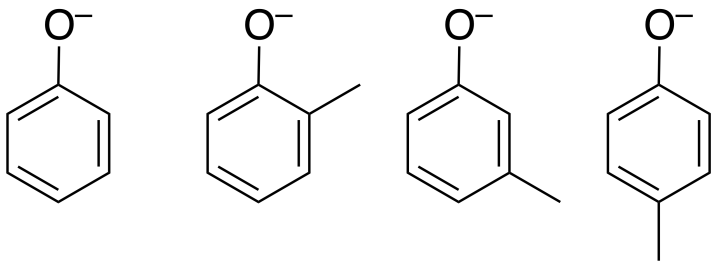

Figure 4.1.1: Chemical structure of the molecules studied in this work, listed from left to right, are phenolate, 2-methylphenolate, 3-methylphenolate, and 4-methylphenolate.

4.2 Experimental Details

4.2.1 Steady-State Absorption and Emission

Steady-state absorption spectra were recorded at UCL, while the steady state emission spectra were recorded at the University of Southern Califronia by Shivaley Dey under the supervision of Prof. Stephen Bradforth. Figure 4.2.1 displays the steady-state absorption spectra of each molecule.

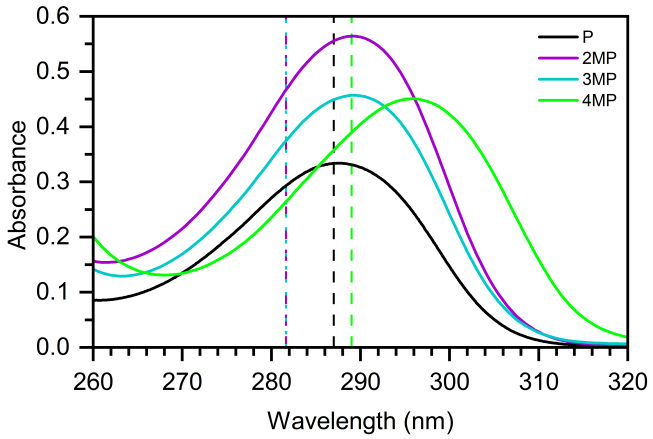

Figure 4.2.1: Steady-state absorption spectrum of 20 mM aqueous solution of phenolate, 2-, 3- and 4-methylphenolate. A path length of 100 μm was used. Excitation wavelengths are displayed as dashed lines on the plot: 282 nm (2MP and 3MP). 287 nm (P) and 289 nm (4MP).

Figure 4.2.2 displays the steady-state emission spectra of each molecule and Figure 4.2.3 shows the fluorescence lifetimes of each molecule.

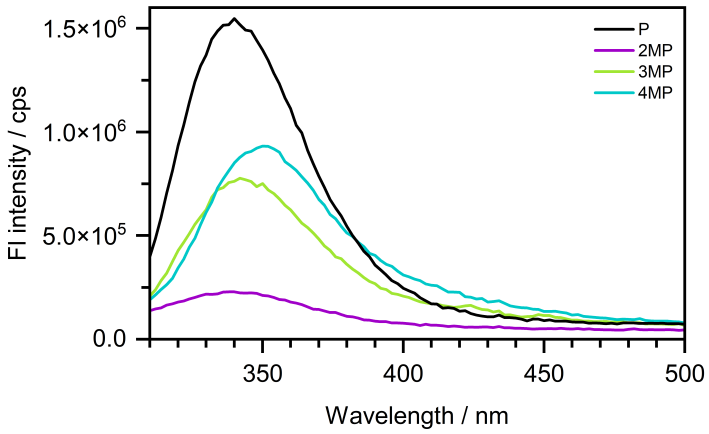

Figure 4.2.2: Steady-state emission spectra of 0.1 mM aqueous solution of phenolate, 2-, 3- and 4-methylphenolate recorded by Shivaley Dey in Prof. Stephen Bradforth's laboratory at the university of Southern California. Step sizes of 2 nm with a 2 nm slit and 2 second integration time. The excitation wavelength of each was the full width half maximum of the first absorption band, and the spectra are normalised to the optical density of the solution at the excitation wavelength.

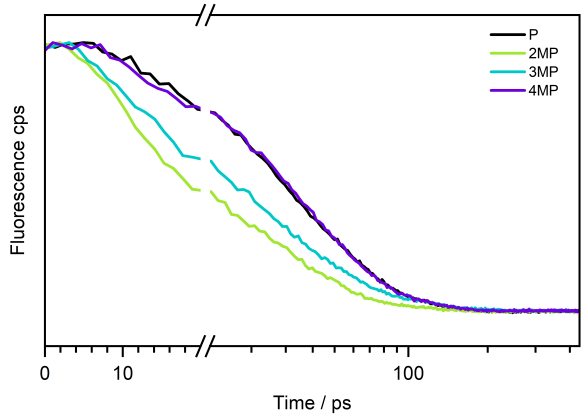

Figure 4.2.3: TCSPC measurements of 0.1 mM aqueous solution of phenolate, 2-, 3- and 4-methylphenolate recorded by Shivaley Dey in Prof. Stephen Bradforth's laboratory at the university of Southern California. Fluorescence intensity is plotted in counts per second (cps). The excitation wavelength for each compound was chosen at the full width at half maximum (FWHM) of the first absorption band on the high-energy edge: 272 nm for phenolate (P), 275 nm for 2-methylphenolate (2MP), 275 nm for 3-methylphenolate (3MP), and 278 nm for 4-methylphenolate (4MP).The spectra are normalised to the optical density of the solution at the excitation wavelength.

Table 4.2.1 summarises, for each molecule, the absorbance maximum, the emission maximum after photoexcitation at 274 nm, and the intensity of the emission at the

emission maxima. This excitation wavelength corresponds to the high-energy edge of the absorption spectrum, consistent with the TCSPC data. Although, phenolate was photoexcited at the peak of the absorption band.

Table 4.2.1: Summary of the absorbance maxima, emission maxima and the intensity of the emission at the emission maxima.

	Absorbance Maximum / nm	Fluorescence Maxima	Intensity at Maxima / cps
P	287	339	1.53×10^6
2MP	282	340	2.2×10^5
3MP	282	342	7.66×10^5
4MP	289	350	9.30×10^5

4.2.2 Time-Correlated Signal Photon Counting

As observed in our earlier work (see Chapter 3), the timescale for slow electron emission from the bottom of S_1 occurs on the same timescale as fluorescence. Therefore, knowing the fluorescence lifetimes is valuable for fitting the transient absorption data. The fluorescence lifetime of each molecule was characterised using time-correlated single photon counting (TCSPC). These experiments were conducted by Shivaley Dey in Prof. Stephen Bradforth's laboratory at the University of Southern California. The results from these experiments are summarised in Table 4.2.2.

Table 4.2.2: Summary of the fluorescence lifetimes for each of the methyl-phenolates. All pump wavelengths are at the full-width half maxima of the S_0-S_1 absorption band.

	Pump Wavelength /nm	Lifetime / ps
P	272	20
2MP	275	7
3MP	275	9
4MP	278	20

4.2.3 Transient Absorption Spectroscopy

2-, 3- and 4-methylphenol (all three: Sigma-Aldrich, $>99\%$ purity) were purchased and used without further purification. 20 mM aqueous 2-, 3-, 4-methylphenolate, and phenolate (2MP, 3MP, 4MP, and P) were prepared from these samples by the addition of concentrated sodium hydroxide solution to achieve pH 13. A commercial (Ultrafast Systems Helios Fire) transient absorption spectrometer was used to interrogate the ultrafast dynamics of phenolate, 2-, 3-, and 4-methylphenolate. The three UV pump wavelengths (287 nm, 282 nm, 282 nm, and 289 nm) were obtained using an optical parametric amplifier (OPAs; Coherent OPerA Solo). The fundamental 800 nm was derived from a regenerative amplifier seeded by a Ti:sapphire oscillator (Coherent Astrella-HE-USP). Each experiment had a pulse energy of around 100 nJ at the sample. The broad-band UV probe was generated by focusing 800 nm on to a calcium flouride plate, providing a 350-650 nm probing region. To exclude effects from polarisation the pump and probe beams were set at the magic angle 54.7°. All four samples were flowed, using a liquid peristaltic pump (masterflex), through a Harrick cell that had a path length of 100 μm.

4.3 Results and Discussion

Transient absorption spectra of 20 mM aqueous 2MP, 3MP , 4MP and P, at various pump-probe delays are presented in Figure 4.3.1. Each molecule was photoexcited at maximum of the S_0-S_1 absorption band. From our previous work (see Chapter 3), [80] following photoexcitation of P at 287 nm there are two excited state absorption (ESA) features. At early pump-probe time delays, an ESA centered at approximately 540 nm is observed that has previously been assigned to an ESA of the S_1 state of phenolate [78, 80]. As observed in our earlier work (Chapter 3), within 10 ps the spectral profile changes, and a broadband feature centered at approximately 700 nm is observed. This is assigned to a solvated electron ($e^-_{(aq)}$) [28, 95]. The $e^-_{(aq)}$ signal decays from 10 ps and the population still exists beyond the 1 ns experimental window, as observed in our previous work. The TA spectra of P is plotted in Figure 4.3.1 (bottom right). Similar dynamics are observed upon photoexcitation

of 4MP at 289 nm, see Figure 4.3.1 (bottom left). The S_1 ESA is observed, centred at around 500 nm, and is most prominent at pump-probe delays before 1 ps. There are two structured bands centred at 406 nm and 387 nm, corresponding to the ESA of the phenoxy radical in it's D_0 (ground) state, as also observed in phenolate [78, 80] and also previously in 4MP[93, 94], though these bands are slightly red-shifted compared to phenolate. This indicates the S_1 ESA is also present within the first few picoseconds and the shape of the absorption band changes as the solvated electron ESA grows over the S_1 ESA and reaches a maximum absorbance at approximately 10 ps. The solvated electron signal then decays over the rest of the 7 ns experimental window. On the blue edge of the spectrum there is a negative absorption feature, centred at approximately 360 nm, this band shape matches the steady-state emission (see Figure 4.2.2) and therefore we have assigned it to be stimulated emission (SE), Fig 4.2.2. Following photoexcitation of 3MP at 282 nm, Figure 4.3.1 (top right), the same four absorption features are observed. The contribution of S_1 ESA (approximately centred at 500 nm) is not as prominent, likely due to a larger contribution of solvated electron. The S_1 ESA is always overlapped with the tail of the solvated electron ESA. The phenoxy radical peaks are again present effectively instantly, implying the electron is rapidly formed. The solvated electron contribution, again reaches its maximum absorbance at around 10 ps and then decays over the rest of the 7 ns experimental window. The red-edge of the SE can be seen at 350 nm, and the band shape of this matches with the steady-state emission spectrum, see Figure 4.2.2. Following photoexcitation at 282 nm of 2MP, Figure 4.3.1 (top left), again the same four absorption features can be observed. The S_1 ESA is weakly observed (centred at approximately 520 nm) in the first few picoseconds, but over this the solvated electron is rapidly formed reaching a maximum absorbance signal within 1 ps .

Again, the phenoxy radical peaks are again present effectively instantly thus implying the instanteous formation of the solvated electron.

Figure 4.3.2 displays the kinetic traces for 500 and 645 nm probe wavelengths. The 645 nm represents the solvated electron and the 500 nm represents the S_1 ESA.

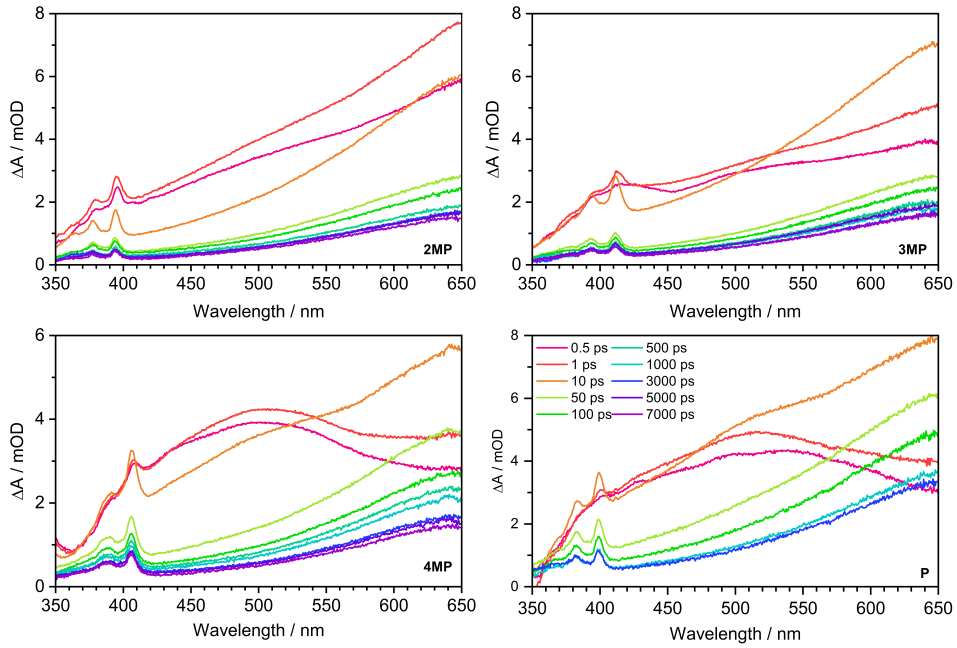

Figure 4.3.1: 350–650 nm transient absorption spectra of 20 mM aqueous P, 2MP, 3MP, 4MP, and phenolate at displayed pump-probe delays following photoexcitation at 282 nm (top left), 282 nm (top right), 289 nm (bottom left), and 287 nm (bottom right). The broad absorption centered around 650 nm is attributed to solvated electrons and the absorption feature with a peak around 500 nm is attributed to the S_1 state. This feature is most prominent in 4-methylphenolate and phenolate.

The solvated electron plot highlights the difference in electron recombination times. The closer the methyl group is to the oxygen atom the faster the recombination timescale.

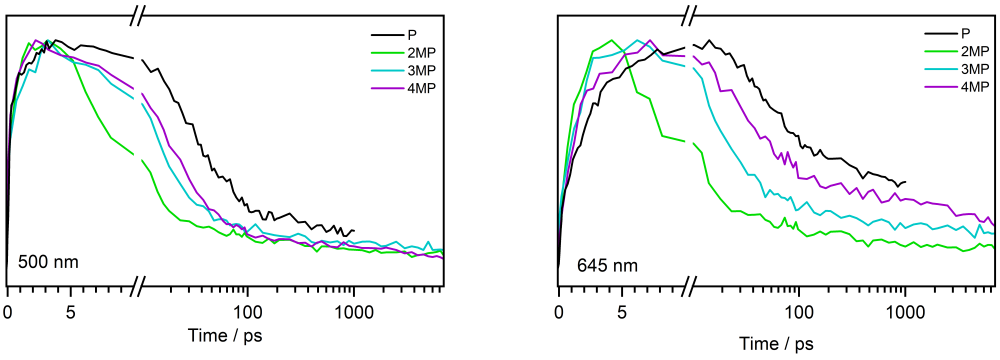

Figure 4.3.2: Kinetic traces at two probe wavelengths displayed for 2MP, 3MP, 4MP and P; **Left** 500 nm and **Right** 645 nm. Kinetic traces are normalised.

4.3.1 Experimental Data Analysis

As observed in the TA spectra, there are three common features: the excited-state absorption (ESA) of the solvated electron, the phenoxy radical peaks, and the S_1 ESA. The 645 nm kinetic traces (see Figure 4.3.2) clearly indicate that the formation of the solvated electron occurs on two distinct timescales. The ESA of the solvated electron is extremely broad, leading to overlap with the other ESA features. To disentangle the kinetics of these overlapping signals, all three molecules were analysed using the University of Bristol's KOALA software [59]. For consistency, the UV-TA spectrum of phenolate, from Chapter 3, was also analysed using the same approach. The KOALA software allows for arbitrary shapes to be fit to each spectral feature, enabling a global fit across all time points to extract the corresponding kinetics. The instrument response function (IRF) was determined as described in Chapter 2, by fitting to the solvent-only data across various pump wavelengths. Figure 4.3.3 provides an example of this fit applied to the phenolate data at a probe wavelength of 365 nm.

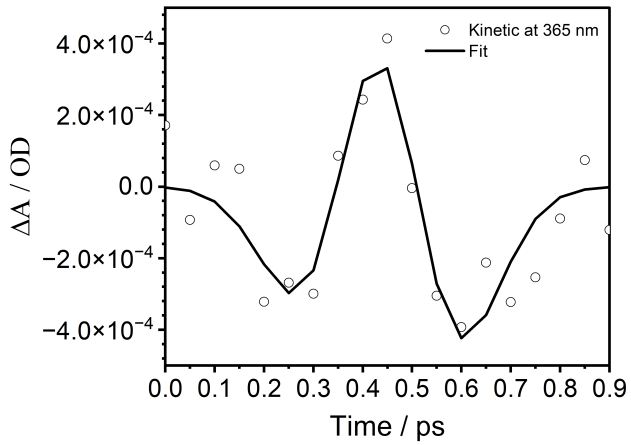

Figure 4.3.3: . Example fit of phenolate data at a probe wavelength of 365 nm to determine the IRF. This fit provides an IRF of 260 fs.

4.3.2 Phenolate

Figure 4.3.4 shows four frames from the fitting of the phenolate transient absorption spectrum across all times. This is to extract the kinetic profiles associated with each transient feature. These frames are 0.48 ps (top left), 1 ps (top right), 10 ps (bottom left) and 1000 ps (bottom right).

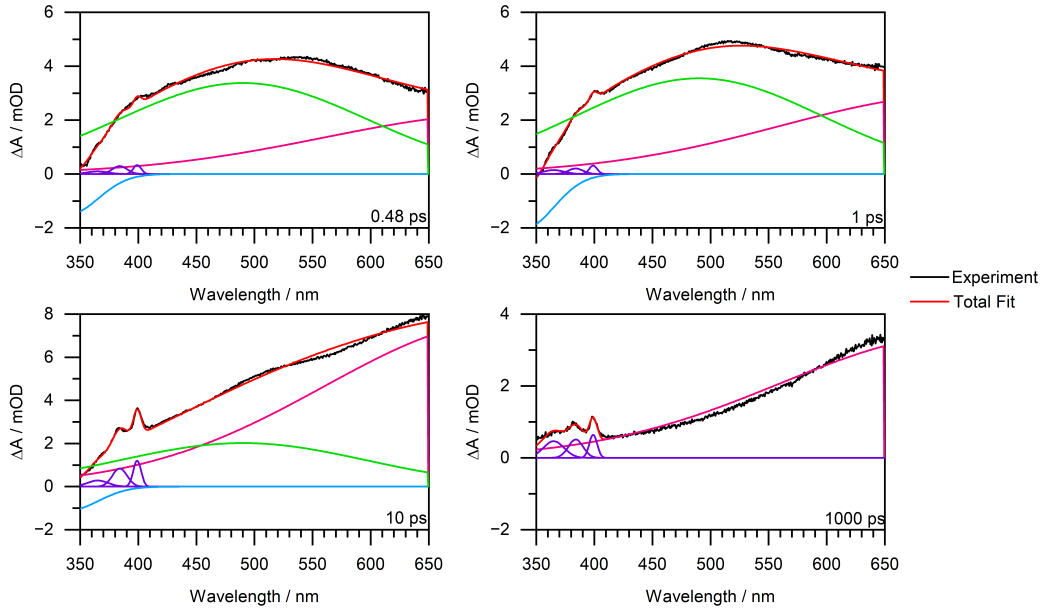

Figure 4.3.4: 350–650nm transient absorption spectra of 20 mM aqueous phenolate at 0.48 ps (top left), 1 ps (top right), 10 ps (bottom left) and 1000 ps (bottom right) pump-probe time delays following photoexcitation at 287 nm. Black line is the experimental data and the red is the total fit made up from each other feature; S_1 (490 nm), SE (340 nm), $PhO^{\cdot}$ (365 nm), $PhO^{\cdot}$ (384 nm), $PhO^{\cdot}$ (399 nm) and $e_{(aq)}$ (719 nm). Each feature was modelled by a Gaussian function.

The kinetic traces corresponding to the data fit in the KOALA software (see Figure 4.3.4) are extracted for each feature. The data in KOALA was fit to in two parts; from 0–30 ps and 30–1000 ps. In the longer time fit it is known there will be no contribution from S_1 as the literature fluorescence lifetime is 22 ps at a pump wavelength of 266 nm[78]. From our TCSPC measurements (see Section 4.2.2) we found the fluorescence lifetime to be 20 ps at a pump wavelength of 272 nm. Therefore, from 30 ps S_1 was not modelled in the KOALA fit as there will not be any significant contribution. Figure 4.3.5 displays the fit to the S_1 and SE contributions. The S_1 lifetime was found to be 19.3 ± 0.9 ps, which is in good agreement with the fluorescence lifetime. The SE kinetic extracted from the KOALA fit is a bit noisy. It was fit with a fixed lifetime of 19.3 ps and this gave an R^2 value of 0.88, the quality of the fit is reduced due to the noise on the SE signal.

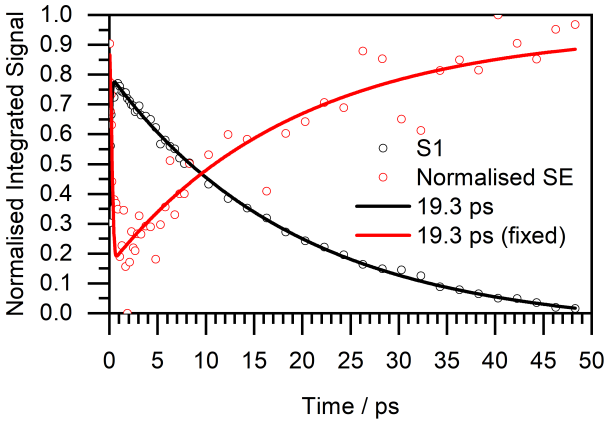

Figure 4.3.5: The S_1 signal (black circles) is fit (black line) with an exponential with a lifetime of 19.3 $\pm$ 0.9 ps, convoluted with the instrument response function (IRF) of 0.25 ps. The fit provides an R^2 value of 0.99. The S_1 amplitude is normalised relative to the solvated electron signal in the KOALA fit. For clarity, the SE kinetics (red circles) extracted from KOALA was normalised between 0 and 1, as it's amplitude contribution in the fit is small. The SE is fit with and exponential of fixed lifetime of 19.3 ps convoluted with the IRF of 0.25 ps. The fit provides an R^2 value of 0.88.

Figure 4.3.6 displays the fitting of the solvated electron signal to extract the geminate recombination and electron appearance timescales. Figure 4.3.6 (left) shows the fit to extract the electron appearance timescales. The black circles are the solvated electron signal extracted from the early time fit (0–30 ps). The geminate recombination dynamics (black line) are subtracted from the solvated electron signal, leaving the electron appearance signal (red circles). The electron appearance dynamics are fit to with a biexponential to describe the contributions from hot and cold S_1. One of the lifetimes is fixed to be 19.3 ps matching the S_1 lifetime, to describe the electron formation from cold S_1. The second time constant is 2.7 ± 0.2 ps. Figure 4.3.6 (right) shows the solvated electron signal from the long time fit (30–1000 ps), this is fit to with a biexponetial to extract the timescales for geminate recombination.

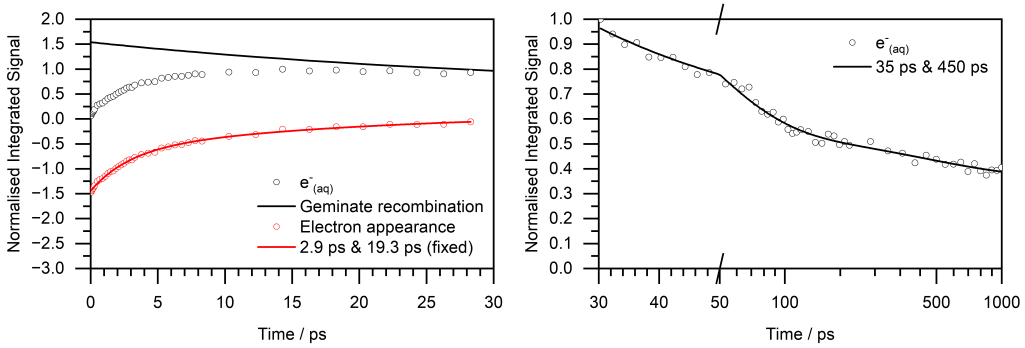

Figure 4.3.6: Fits to the 20 mM P data following 287 nm photoexcitation. **Left:** Black circles are the solvated electron signal extracted from the 0–30 ps fit. The black line, which if the fit to the geminate recombination, is interpolated to early times. The contribution of geminate recombination is subtracted from solvated electron signal (black circles) is taken from the early time KOALA fit (0–30 ps). This leaves the electron appearance (red circles) dynamics which are fit to with a biexponential (convoluted with the instrument function) with lifetimes of 2.9 $\pm$ 0.2 ps and 19.3 ps. The 19.3 ps lifetime is fixed during the fitting. **Right:** The black circles are the modelled solvated electron signal from the long time KOALA fitting (30–1000 ps) and the dynamics are fit with a biexponential function with lifetimes of 35 $\pm$ 4 ps and 450 $\pm$ 200 ps, to describe geminate recombination.

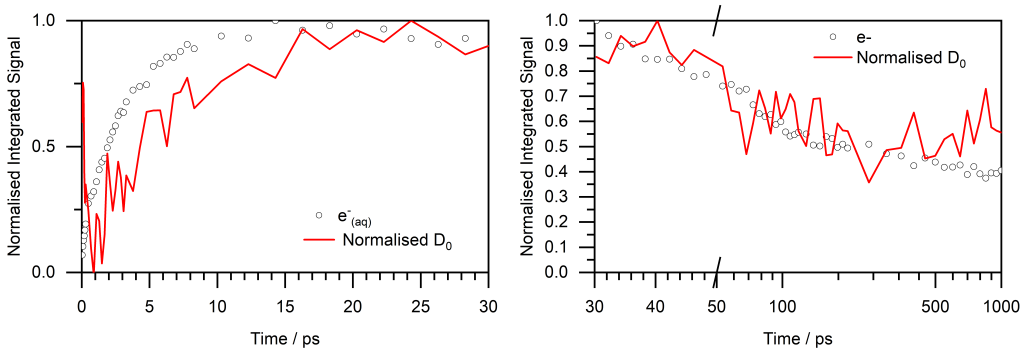

Figure 4.3.7: Fits to the 20 mM P data following 287 nm photoexcitation. **Left:** The early time (0–30 ps) KOALA extracted trace of the average phenoxy radical signal. The Phenoxy radical signal is normalised to the solvated electron signal. **Right:** The long time (30–1000 ps) kinetics of the solvated electron (black circles) are presented and the average phenoxy radical signal is normalised to the solvated electron signal.

Figure 4.3.7 displays the kinetics extracted from the KOALA software for the average phenoxy radical (red line) and the solvated electron (red circles). The phenoxy

radical signal is normalised to the solvated electron signal. The plot on the left displays the data extracted from the early time fits (0–30 ps) and the right displays the long time fits (30–1000 ps). The dynamics of the radical are expected to be the same as the solvated electron. Both the early and late time dynamics resemble the solvated electron dynamics reasonably, but the radical kinetics are clearly quite noisy.

4.3.3 2-Methylphenolate

Figure 4.3.8 shows four frames of the fitting done for the transient absorption spectrum across all times to extract the kinetic profiles associated with each transient feature. These frames are 0.48 ps (top left), 1 ps (top right), 10 ps (bottom left) and 1000 ps (bottom right).

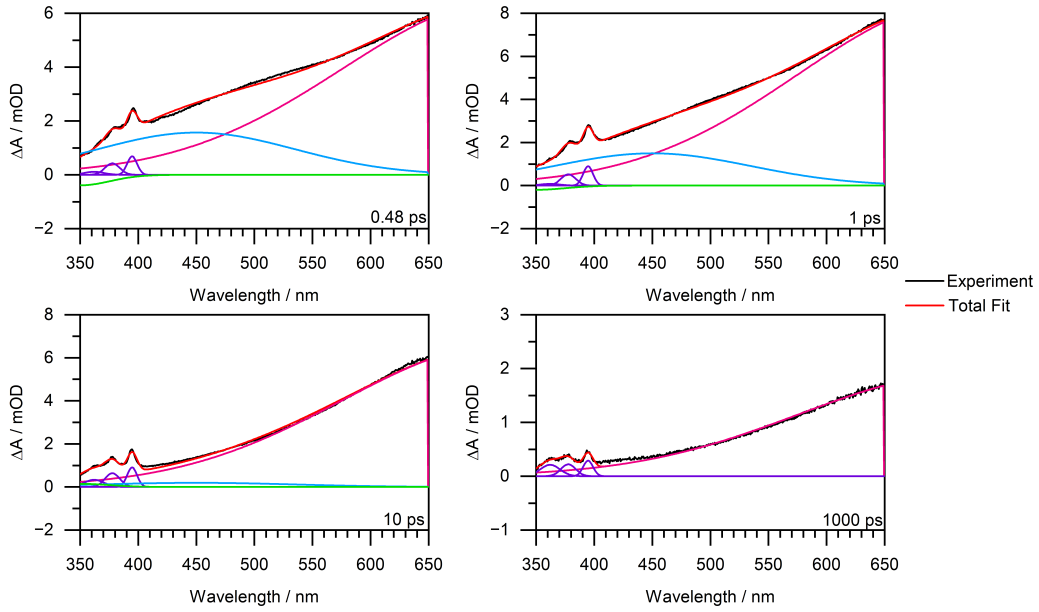

Figure 4.3.8: 350–650nm transient absorption spectra of 20 mM aqueous P following 287 nm photoexcitation at 0.48 ps (top left), 1 ps (top right), 10 ps (bottom left) and 1000 ps (bottom right) pump-probe time delays following photoexcitation at 282 nm. Black line is the experimental data and the red is the total fit made up from each other feature; S_1 (450 nm), SE (350 nm), $PhO^{\cdot}$ (362 nm), $PhO^{\cdot}$ (377.7 nm), $PhO^{\cdot}$ (394.7 nm) and $e_{(aq)}$ (719 nm). Each feature was modelled by a Gaussian function.

The kinetic traces corresponding to the fit to the data (see Figure 4.3.8) are extracted for each feature and then to extract the timescales of each process are fit to. The data

in KOALA was divided in two parts; from 0–20 ps and 10–1000 ps. In the longer time fit it is known there is no contribution from S_1 as the fluorescence lifetime is 7 ps at a pump wavelength of 275 nm (see Section 4.2.2). Therefore, from 10 ps S_1 was not modelled in the KOALA fit as there will not be any contribution. Figure 4.3.9 displays the fit to the S_1 and shows the kinetic trace for the SE contribution. The S_1 lifetime was fixed to be 7 ps, which provided a fit with a R^2 value of 0.96. The SE kinetic trace extracted from the KOALA fit was not fit as no sensible result could be obtained.

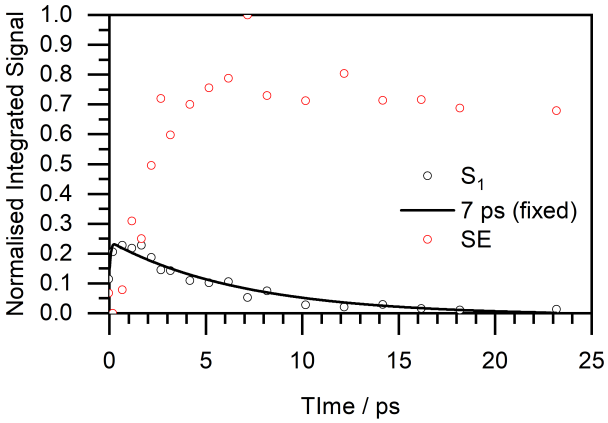

Figure 4.3.9: The S_1 signal (black circles) is fit (black line) with an exponential with a fixed lifetime of 7 ps, convoluted with the instrument response function (IRF) of 0.25 ps. The fit provides an R^2 value of 0.96. The S_1 amplitude is normalised relative to the solvated electron signal in the KOALA fit. For clarity, the SE kinetics (red circles) extracted from KOALA were normalised between 0 and 1, as it's amplitude contribution in the fit is small. The SE could not be fit reasonably.

Figure 4.3.10 displays the fitting of the solvated electron signal to extract the geminate recombination and electron appearance timescales. Figure 4.3.10 (left) shows the fit to extract the electron appearance timescales. The black circles are the solvated electron signal extracted from the early time fit (0–20 ps). The geminate recombination dynamics (black line) are subtracted from the solvated electron signal, leaving the electron appearance signal (red circles). The electron appearance dynamics are fit to with a biexponential to describe the contributions from hot and cold S_1. One of the lifetimes is fixed to be 7 ps, to describe the electron formation from cold S_1. The second time constant is 2.0 $\pm$ 0.1 ps. This fit provides an R^2

value of 0.99. Figure 4.3.10 (right) shows the solvated electron signal from the long time fit (10–1000 ps), this is fit to with a biexponential to extract the timescales for geminate recombination.

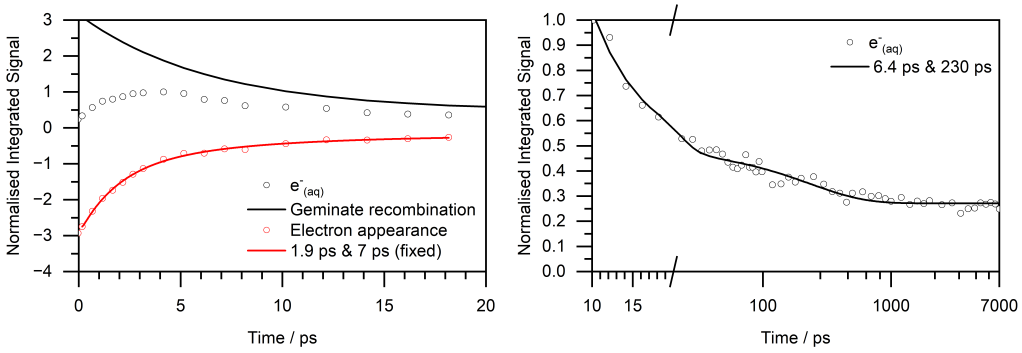

Figure 4.3.10: Left: Black circles are the solvated electron signal extracted from the 0–20 ps fit. The black line in the geminate recombination interpolated to early times. The geminate recombination contribution is subtracted from the solvated electron signal (black circles), from the early time KOALA fit (0–20 ps). This leaves the electron appearance (red circles) dynamics which are fit to with a biexponential (convoluted with the instrument function) with lifetimes of 1.9 $\pm$ 0.1 ps and 7 ps. The 7 ps lifetime is fixed during the fitting. **Right:** The black circles are the modelled solvated electron signal from the long time KOALA fitting (10–1000 ps) and the dynamics are fit with a biexponential function with lifetimes of 6.4 $\pm$ 0.6 ps and 230 $\pm$ 40 ps, to describe geminate recombination.

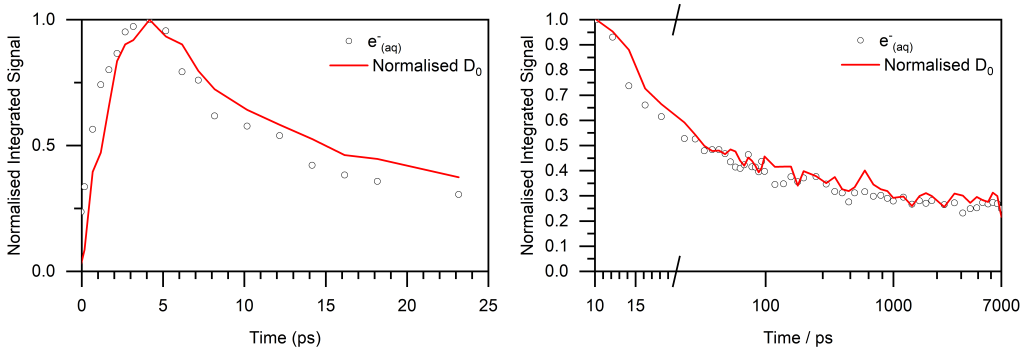

Figure 4.3.11: Left: The early time (0–20 ps) KOALA extracted trace of the average phenoxy radical signal. The Phenoxy radical signal is normalised to the solvated electron signal. **Right:** The long time (10–1000 ps) kinetics of the solvated electron (black circles) are presented and the average phenoxy radical signal is normalised to the solvated electron signal.

Figure 4.3.11 displays the kinetics extracted from the KOALA software for the average phenoxy radical (red line) and the solvated electron (red circles). The phenoxy radical signal is normalised to the solvated electron signal. The plot on the left displays the data extracted from the early time fits (0–20 ps) and the right displays the long time fits (10–1000 ps). The dynamics of the radical are expected to be the same as the solvated electron. Both the early and late time dynamics resemble the solvated electron dynamics well.

4.3.4 3-Methylphenolate

Figure 4.3.12 shows four frames of the fitting done to the transient absorption spectrum across all times to extract the kinetic profiles associated with each transient feature. These frames at are 0.66 ps (top left), 1 ps (top right), 10 ps (bottom left) and 1000 ps (bottom right).

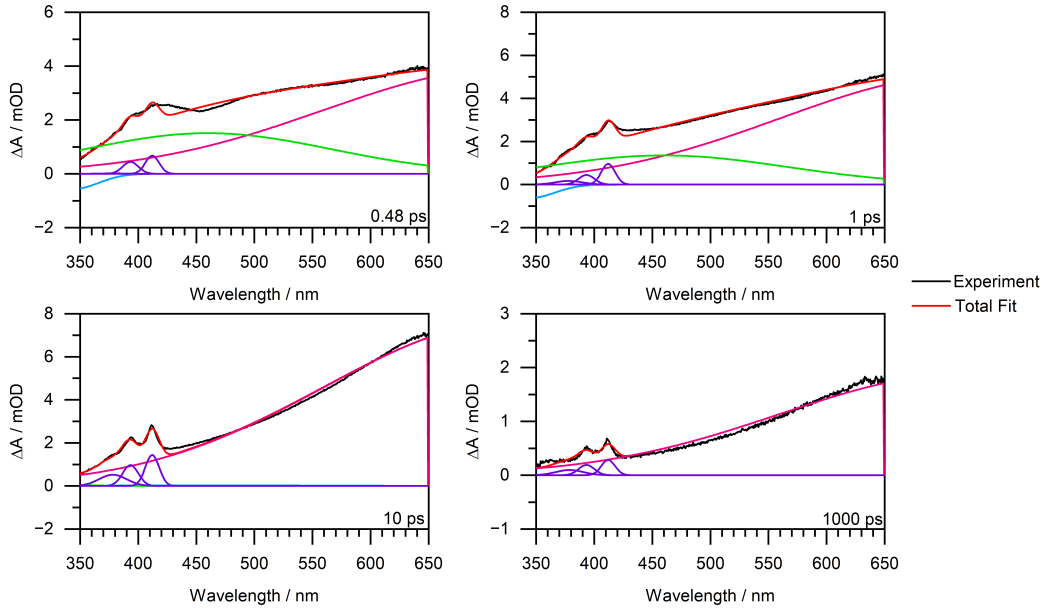

Figure 4.3.12: 350–650 nm transient absorption spectra of 20 mM aqueous 3-methylphenolate at 2.7 ps pump-probe delay following photoexcitation at 282 nm. Black line is the experimental data and the pink is the total fit made up from each other feature; S_1 (430 nm), SE (349 nm), $PhO^{\cdot}$ (378.1 nm), $PhO^{\cdot}$ (393.3 nm), $PhO^{\cdot}$ (412 nm), and $e_{(aq)}$ (719 nm). Each feature was modelled by a Gaussian function.

The kinetic traces corresponding to the fit to the data (see Figure 4.3.12) are extracted for each feature. These traces are then analysed to determine the timescales of each process. The data in KOALA was fit to in two parts; from 0–20 ps and 10–1000 ps. In the longer time fit it is known there is no contribution from S_1 as the fluorescence lifetime is 9 ps at a pump wavelength of 275 nm (see Section 4.2.2). Therefore, from 20 ps S_1 was not modelled in the KOALA fit as there will not be any contribution. Figure 4.3.13 displays the fit to the S_1 and shows the kinetic for the SE contribution. The S_1 lifetime was fixed to be 9 ps, which provided a fit with a R^2 value of 0.98. The SE kinetic extracted from the KOALA fit was normalised to be between 0 and 1 and fitted with a monoexponential with a fixed lifetime of 9 ps, providing a fit with a R^2 value of 0.94 .

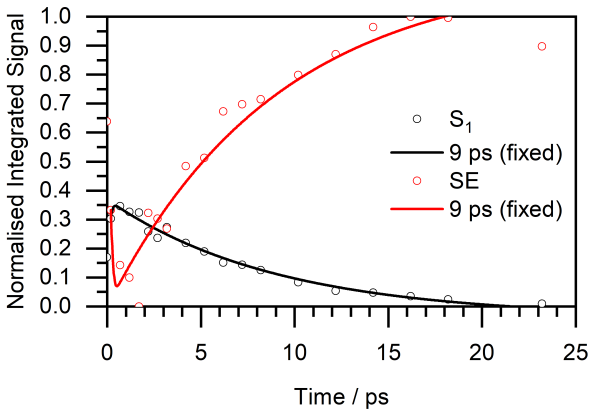

Figure 4.3.13: The S_1 signal (black circles) is fit (black line) with an exponential with a fixed lifetime of 9 ps, convoluted with the instrument response function (IRF) of 0.25 ps. The fit provides an R^2 value of 0.98. The S_1 amplitude is normalised relative to the solvated electron signal in the KOALA fit. The SE kinetics (red circles) extracted from KOALA was normalised between 0 and 1, as it's amplitude contribution in the fit is small. For clarity, the SE was fit an exponential with a fixed lifetime of 9 ps, convoluted with the IRF of 0.25 ps. The fit provides an R^2 value of 0.94

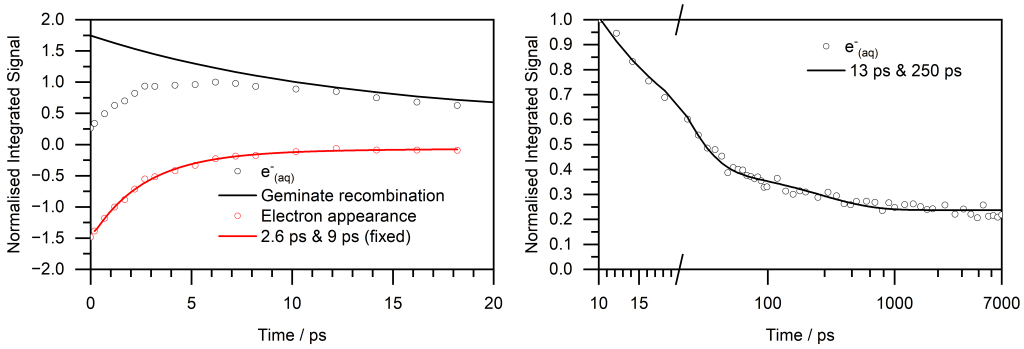

Figure 4.3.14: Left: Black circles are the solvated electron signal extracted from the $0-20$ ps fit. The black line in the geminate recombination interpolated to early times. The geminate recombination contribution is subtracted from the solvated electron signal (black circles), from the early time KOALA fit (0–20 ps). This leaves the electron appearance (red circles) dynamics which are fit to with a biexponential (convoluted with the instrument function) with lifetimes of 2.6 ± 0.4 ps and 9 ps. The 9 ps lifetime is fixed during the fitting. **Right:** The black circles are the modelled solvated electron signal from the long time KOALA fitting (10–1000 ps) and the dynamics are fit with a biexponential function with lifetimes of 13 ± 0.8 ps and 250 ± 40 ps, to describe geminate recombination.

Figure 4.3.14 displays the fitting of the solvated electron signal to extract the gemi-

nate recombination and electron appearance timescales. Figure 4.3.14 (left) shows the fit to extract the electron appearance timescales. The black circles are the solvated electron signal extracted from the early time fit (0–20 ps). The geminate recombination dynamics (black line) are subtracted from the solvated electron signal, leaving the electron appearance signal (red circles). The electron appearance dynamics are fit to with a biexponential to describe the contributions from hot and cold S_1. One of the lifetimes is fixed to be 9 ps, to describe the electron formation from cold S_1. The second time constant is 2.6 $\pm$ 0.4 ps. This fit provides an R^2 value of 0.99. Figure 4.3.14 (right) shows the solvated electron signal from the long time fit (10–1000 ps), this is fit to with a biexponential to extract the timescales for geminate recombination.

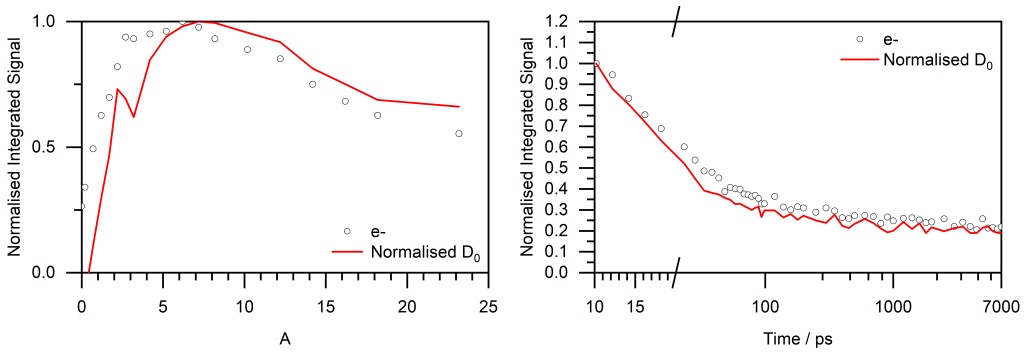

Figure 4.3.15: Left: The early time (0–20 ps) KOALA extracted trace of the average phenoxy radical signal. The Phenoxy radical signal is normalised to the solvated electron signal. **Right:** The long time (10–1000 ps) kinetics of the solvated electron (black circles) are presented and the average phenoxy radical signal is normalised to the solvated electron signal.

Figure 4.3.15 displays the kinetics extracted from the KOALA software for the average phenoxy radical (red line) and the solvated electron (red circles). The phenoxy radical signal is normalised to the solvated electron signal. The plot on the left displays the data extracted from the early time fits (0–20 ps) and the right displays the long time fits (10–1000 ps). The dynamics of the radical are expected to be the same as the solvated electron. Both the early and late time dynamics resemble the

solvated electron dynamics well.

4.3.5 4-Methylphenolate

Figure 4.3.16 shows four frames of the fitting done to the transient absorption spectrum across all times to extract the kinetic profiles associated with each transient feature. These frames at are 0.48 ps (top left), 1 ps (top right), 10 ps (bottom left) and 1000 ps (bottom right).

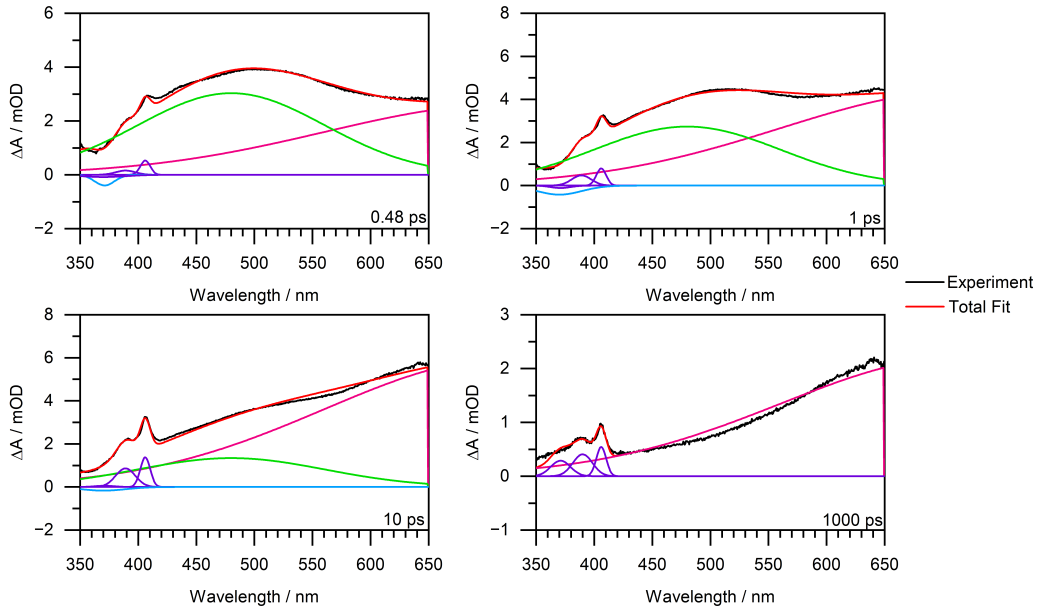

Figure 4.3.16: 350–650 nm transient absorption spectra of 20 mM aqueous 4MP, following 278 nm photoexcitation, at 0.48 ps (top left), 1 ps (top right), 10 ps (bottom left) and 1000 ps (bottom right) pump-probe time delays following photoexcitation at 287 nm. Black line is the experimental data and the red is the total fit made up from each other feature; S_1 (480 nm), SE (370 nm), $PhO^{\cdot}$ (371 nm), $PhO^{\cdot}$ (390 nm), $PhO^{\cdot}$ (406 nm) and $e_{(aq)}$ (719 nm). Each feature was modelled by a Gaussian function.

The kinetic traces corresponding to the fit to the data (see Figure 4.3.16) are extracted for each feature. These traces are then analyzed to determine the timescales of each process. The data in KOALA was fit to in two parts; from 0–20 ps and 20–1000 ps. In the longer time fit it is known there is no contribution from S_1 as the fluorescence lifetime is 20 ps at a pump wavelength of 278 nm (see Section 2.2.2). Therefore, from 20 ps S_1 was not modelled in the KOALA fit as there will not be any contribution. Figure 4.3.17 displays the fit to the S_1 and shows the kinetic for

the SE contribution. The S_1 lifetime was fixed to be 20 ps, which is in provided a fit with a R^2 value of 0.98. The quality of this fit was improved by floating the value and this provided a time constant of 12.4 ps with a R^2 value of 0.99. The SE kinetic extracted from the KOALA fit was normalised to be between 0 and 1 and fitted with a monoexponential with a fixed lifetime of 14 ps, providing a fit with a R^2 value of 0.77 .

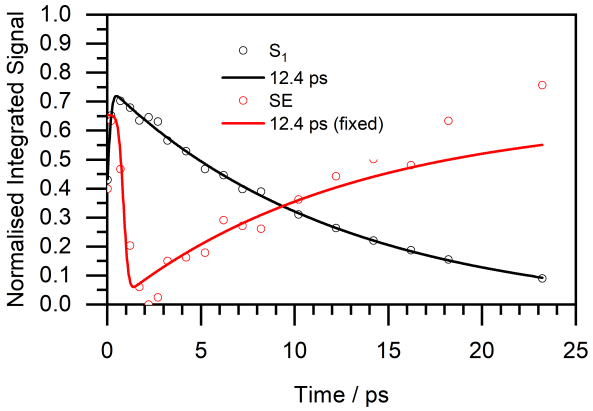

Figure 4.3.17: The S_1 signal (black circles) is fit (black line) with an exponential with a lifetime of 12.4 $\pm$ 1 ps, convoluted with the instrument response function (IRF) of 0.30 ps. The fit provides an R^2 value of 0.99. The S_1 amplitude is normalised relative to the solvated electron signal in the KOALA fit. The SE kinetics (red circles) extracted from KOALA was normalised between 0 and 1, as it's amplitude contribution in the fit is small. The SE was fit an exponential with a fixed lifetime of 12.4 ps, convoluted with the IRF of 0.30 ps. The fit provides an R^2 value of 0.77.

Figure 4.3.18 displays the fitting of the solvated electron signal to extract the geminate recombination and electron appearance timescales. Figure 4.3.18 (left) shows the fit to extract the electron appearance timescales. The black circles are the solvated electron signal extracted from the early time fit (0–20 ps). The geminate recombination dynamics (black line) are subtracted from the solvated electron signal, leaving the electron appearance signal (red circles). The electron appearance dynamics are fit to with a biexponential to describe the contributions from hot and cold S_1. One of the lifetimes is fixed to be 12.4 ps, to describe the electron formation from cold S_1. The second time constant is 2.0 $\pm$ 0.2 ps. This fit provides an R^2 value of 0.99. Figure 4.3.18 (right) shows the solvated electron signal from the long

time fit (20–1000 ps), this is fit to with a biexponential to extract the timescales for geminate recombination.

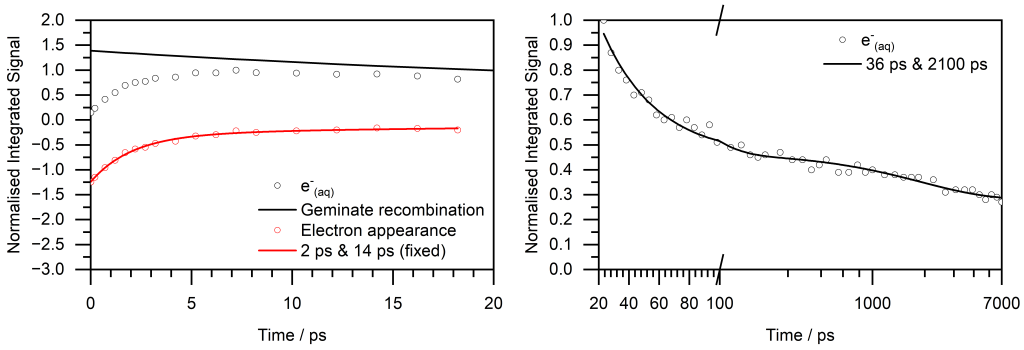

Figure 4.3.18: Left: Black circles are the solvated electron signal extracted from the 0–20 ps fit. The black line in the geminate recombination interpolated to early times. The geminate recombination contribution is subtracted from the solvated electron signal (black circles), from the early time KOALA fit (0–20 ps). This leaves the electron appearance (red circles) dynamics which are fit to with a biexponential (convoluted with the instrument function) with lifetimes of 2.0 ± 0.2 ps and 12.4 ps. The 12.4 ps lifetime is fixed during the fitting. **Right:** The black circles are the modelled solvated electron signal from the long time KOALA fitting (10–1000 ps) and the dynamics are fit with a biexponential function with lifetimes of 36 ± 3 ps and 2100 ± 500 ps, to describe geminate recombination.

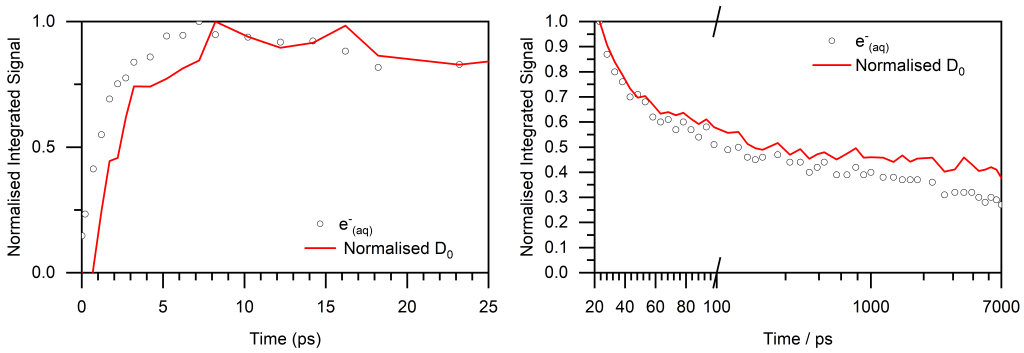

Figure 4.3.19: Left: The early time (0–20 ps) KOALA extracted trace of the average phenoxy radical signal. The Phenoxy radical signal is normalised to the solvated electron signal. **Right:** The long time (20–1000 ps) kinetics of the solvated electron (black circles) are presented and the average phenoxy radical signal is normalised to the solvated electron signal.

Figure 4.3.19 displays the kinetics extracted from the KOALA software for the average phenoxy radical (red line) and the solvated electron (red circles). The phenoxy radical signal is normalised to the solvated electron signal. The plot on the left displays the data extracted from the early time fits (0–20 ps) and the right displays the long time fits (20–1000 ps). The dynamics of the radical are expected to be the same as the solvated electron. Both the early and late time dynamics resemble the solvated electron dynamics well.

4.3.6 Calculations

The calculations presented here were carried out by Anton Boichenko and Anastasia Bochenkova at the University of Moscow. Calculations were performed at the XMCQDPT2[5]/SA(5)-CASSCF(8,10)/(aug)-cc-pVDZ(+) level of theory. The gas-phase and condensed-phase vertical detachment energies are summarised in Table 4.3.1.

Table 4.3.1: Summary of results obtained from calculations performed at the XMCQDPT2[5]/SA(5)-CASSCF(8,10)/(aug)-cc-pVDZ(+) level of theory. The structures used fir calculating the VDEs are optimised using a mixed DFT/EFP/MD method.

	VDE, eV solavated (XMCQDPT2/EFP)	VDE, eV Gas phase DFT
P	6.9	2.25
2MP	6.5	2.18
3MP	6.9	2.22
4MP	6.5	2.12

Figure 4.3.20 displays the solvated systems. Four water molecules were included quantum mechanically in each system. For P, 3MP and 4MP, all 4 water molecules are hydrogen bonded to the O atom of phenolate. In contrast, for 2MP, only 3 of the water molecules are hydrogen-bonded to the O atom and the fourth water molecule is H-bonded to the 3 other water molecules. This appears to create a 'hydrophobic cavity' due to the proximity of the methyl group to the O atom of phenolate.

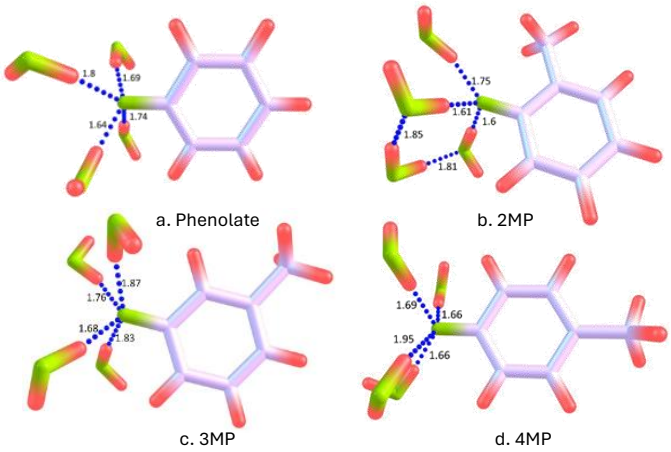

Figure 4.3.20: Displays microsolvation snapshots of P, 2MP, 3MP and 4MP chemical structures with the four water molecules were included quantum mechanically.

In comparison to P, for the solvated systems, the 2MP and 4MP have a significant lowering in the VDE. The observed difference between the VDE of P and, 2MP and 3MP is more significant for the solvated than the gas-phase systems. The degree of anion stabilisation by the solvent molecules varies with system. The 2MP anion has a lesser degree of stabilisation by the nearest water molecules that form direct hydrogen bonds with the anion. The methyl-group on the *ortho* position (2MP) results in an area which is not accessible by water molecules. The 4MP anion also has less stabilisation in comparison to phenolate due to its asymmetric solvation and the area excluded by the methyl group on the *para* position. However, the stabilisation of the neutral radical by the methyl-group is highest for 4MP due to the presence of the quinoid-like structure. The methyl-group acts as an inductive electron donor, destabilising the 2MP and 4MP anions. However, the radicals are stabilised by the presence of the methyl groups. The 3MP anion is the most similar to phenolate, which is practically not perturbed by the methyl-group.

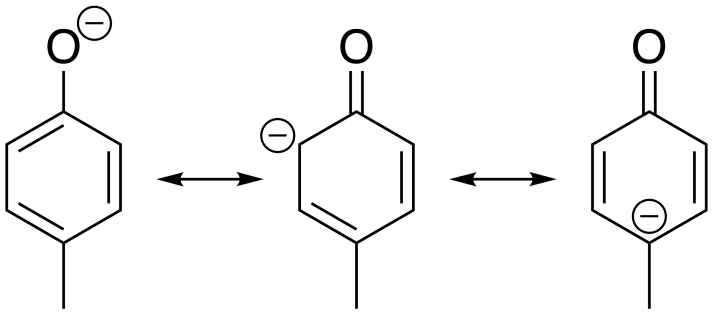

Figure 4.3.21: Resonance structures for 4-methylphenolate.

To summarise, the vertical detachment energies of 2MP and 4MP are lower than 3MP and P and this is amplified more in solution in comparison to the gas-phase phase. The VDEs are summarised below in Figure 4.3.22.

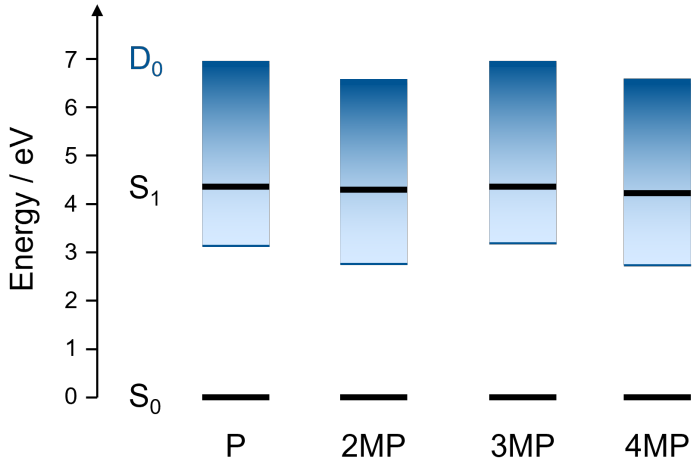

Figure 4.3.22: Summary of the vertical detachment energies for each molecule calculated using XMCQDPT2[5]/SA(5)-CASSCF(8,10)/(aug)-cc-pVDZ(+)/EFP level of theory.

4.3.7 Summary of Results

Table 4.3.2 summaries the time constants obtained from fitting to the kinetic traces obtained from KOALA.

Table 4.3.2: Time constants (in ps) obtained from fits to the kinetic traces $\tau_{S'_n \rightarrow e^-(aq)}$ is the timescale of $e^-_{(aq)}$ formation from directly populated 'hot' S_1 and $\tau_{S_1 \rightarrow e^-(aq)}$ is the timescale of $e^-_{(aq)}$ formation from 'cold' S_1. τ_{r1} and τ_{r2} describe the decay of $e^-_{(aq)}$ by geminate recombination.

	$\tau_{S'_n \rightarrow e^-(aq)}$	A_1	$\tau_{S_1 \rightarrow e^-(aq)}$	A_2	τ_{r1}	A_1	τ_{r2}	A_2
P	2.9 ± 0.2	0.47	19 ± 0.9	0.53	35 ± 4	0.85	450 ± 200	0.15
2MP	1.9 ± 0.5	0.68	7 ± 2	0.32	6.4 ± 0.6	0.98	230 ± 40	0.02
3MP	2.6 ± 0.4	0.90	9 ± 2	0.10	13 ± 0.8	0.89	250 ± 40	0.11
4MP	2.0 ± 0.2	0.90	12 ± 1	0.10	36 ± 3	0.90	2100 ± 500	0.10

The electron ejection timescale appears to be relatively independent of the methyl-group's position on the molecule. However, it is important to note there is a small variation in the vertical detachment energies (VDEs) among the different methyl-substituted phenolates, with the order being 2MP $<$ 4MP $<$ 3MP $<$ P. For 2MP and 4MP, where the VDEs are lower, the timescale for fast electron formation is notably shorter than for 3MP and phenolate (see Table 4.3.2). The lower VDE clearly facilitates quicker electron formation, which is responsible for the faster timescales observed in 2MP and 4MP, with values of 1.9 ps and 2 ps, respectively. Due to the higher VDE in 3MP and P the timescales are longer, 2.6 ps and 2.9 ps respectively. This observation is consistent with a Marcus picture for electron emission, where the electron tunneling rate depends on the barrier height. For 2MP and 4MP, the lower VDE reduces the barrier height, leading to faster electron tunneling and the observed shorter timescales. Figure 4.3.23 shows an illustration of this model.

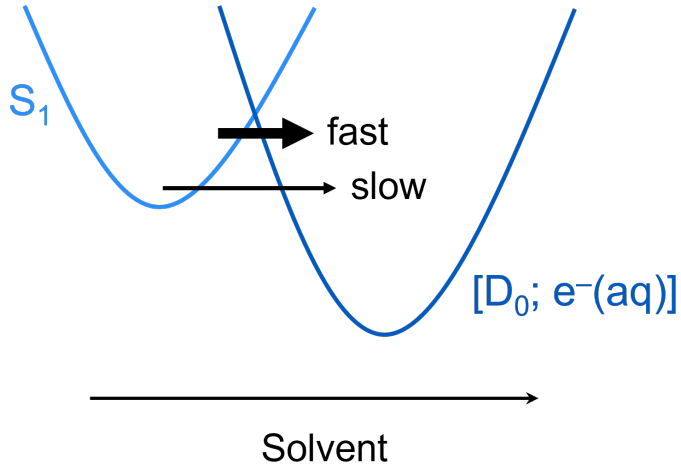

Figure 4.3.23: Marcus like picture for electron emission. Shows the electron emission from vibrationally hot and cold S_1 along the solvent coordinate. Electron emission is faster the higher above the barrier.

Moving on to the timescales for electron emission from the vibrationally cold S_1 state, the emission rate increases as the methyl group is positioned closer to the O^- atom. Although the timescales for 4MP and P from the TA fitting differ slightly from the TCSPC measurements, the overall trend remains consistent. The discrepancies may be attributed to the fact that the TCSPC measurements were performed near the resolution limit of the experiment, potentially explaining the variations. Therefore, the timescales obtained from fitting the TA data, as shown in Table 4.3.2, will be used for further discussion. This might suggests that methyl substitution closer to the O^- atom increases the efficiency of the non-radiative relaxation processes from S_1, which is consistent with the particularly low fluorescence quantum yield for 2MP. Finally, the slower timescale (τ_{r1}) for geminate recombination of the electron is also significantly faster as the methyl-group moves closer to the O^- atom. This could indicate that the local solvation environment has an important role in the electron recombination. As displayed in Figure 4.3.20 the microsolvation snapshots show that 2MP has fewer hydrogen bonds to the O^- atom than the other molecules. Figure 4.3.24 summaries the timescales (see Table 4.3.2) from the kinetic fitting of the TA data. This illustrates clearly the trend of the slow electron emission timescales and fast electron recombination timescales with the position of the O^- atom.

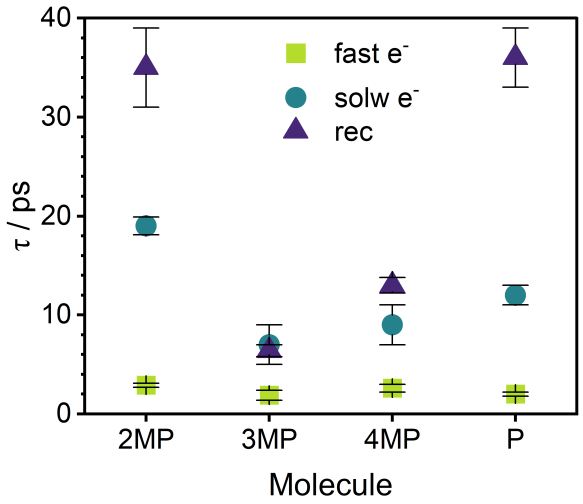

Figure 4.3.24: Summary of timescales for each molecule extracted by kinetic fitting. The error bars for the fast electron emission from vibrationally hot S_1 (green squares) as significantly smaller than the symbol used to plot the timescales.

4.4 Conclusions

To conclude, the photooxidation mechanism of 2MP, 3MP, 4MP and phenolate was investigated following excitation at the peak of the S_0-S_1. It was concluded the VDE energies of the molecules influence the fast electron formation timescales from vibrationally hot S_1. Therefore, due to 2MP and 4MP having the lowest VDEs the fast electron formation timescales are observed here. The electron recombination timescales are quickest for the 2MP, where the methyl-group is the closest to the oxygen atom. It is not possible to be completely sure why the recombination timescales vary. Although, the argument of the electron being trapped when the methyl-group is closer and therefore, the electron recombination is faster more evidence would be required to confirm this. This could be confirmed by the support of electron transport calculations, that can provide information about the electrons trajectory after its formation. An example of these calculation were conducted by Jordan *et al.* were they look at the solvated electrons trajectory at the liquid/vacuum interface [96]. Experimentally, the early sub-picosecond timescale for solvated electron formation could be closely examined using a nIR probe in a TA experiment. By focusing on the early-time relaxation of the solvated electron, com-

parisons can be made across different molecules. As the solvated electron relaxes, its absorption spectrum is expected to shift to shorter wavelengths. By monitoring this spectral shift, a timescale for the relaxation process can be extracted for each molecule, providing further insight into the dynamics of solvated electron formation and relaxation.

Chapter 5

Towards Time-Resolved Liquid-Microjet Photoelectron Spectroscopy of Aqueous Phenolate

This chapter presents the first time-resolved photoelectron spectroscopy (TRPES) data recorded on the UCL liquid microjet spectrometer. This study focuses on aqueous phenolate following $1+1$ resonance-enhanced photodetachment with a $\lambda_{\text{pump=287 }nm}$ and $\lambda_{\text{probe=267 }nm}$. The pump is resonant with the maximum of the S1 absorption band. Following photoexcitation, two features were observed in the photoelectron spectrum. The higher binding energy component was assigned to the solvated electron, while the lower binding energy component was attributed to the $1^1\pi\pi^*$-D_0 state. The total photoelectron signal across all pump-probe delay times was well described by a biexponential decay with lifetimes of 0.2 ± 0.03 ps and 33 ± 4 ps. This behavior is faster than that observed in the corresponding transient absorption data from Chapter 3, suggesting that the mechanism at the surface could differ from that in the bulk solution.

5.1 Motivation

The comparison of different experimental techniques is highly advantageous and, as shown in Chapter 3, can help resolve complex chemical dynamics of molecular systems. This Chapter presents preliminary data recorded during the development

of the capabilities of recording time-resolved liquid microjet photoelectron spectra. These experiments represent the first time-resolved recorded using the liquid microjet setup in the Fielding laboratory. The system selected for study is aqueous phenolate. Phenolate was chosen because there is already a comprehensive understanding of the photoinduced relaxation dynamics from the corresponding transient absorption spectroscopy (TAS) measurements, as detailed in Chapter 3. The ultimate goal is to compare the dynamics observed from femtosecond transient absorption spectroscopy (fs-TAS) (Chapter 3) with the dynamics extracted from the photoelectron experiments.

Both TR-PES and TAS have their unique advantages and can provide valuable information of the photoinduced dynamics of a chemical system. fs-TAS allows excited state dynamics to be followed by measuring the difference in absorption between the ground and the excited state. This facilitates the extraction of the kinetics of different absorption features, although typically these features are hard to resolve due to the high likelihood of them all overlapping. In contrast, TR-PES offers a more direct view of the excited-state potential energy surface by tracking the kinetic energy distribution of the photoelectrons as a function of time. Specifically, with UV pump/UV probe TR-PES, one can monitor the dynamics within excited states. However, when using a UV pump combined with an extreme ultraviolet (EUV) probe, TR-PES can also follow the system's return to the electronic ground state, offering a comprehensive view of the entire photochemical process. This method provides valuable information about the electronic structure and the evolution of the system's electronic states, making it a powerful tool for understanding the excited-state landscape.

The previous literature on aqueous phenolate, specifically regarding fs-TAS, has been discussed in detail in Chapter 3. In terms of photoelectron spectroscopy studies of aqueous phenolate, Ghosh *et al.* recorded valence photoemission spectra of aqueous 0.75 M phenolate with photon energy of 200 eV (see Figure 5.1.1). Their

spectra could be modelled by two Gaussians, centred at 7.1 $\pm$ 0.1 and 8.5 $\pm$ 0.1 with an average full width half maximum at $\sim$ 1 eV. The detachment energies are assigned to the first two states in the phenoxy radical [22]. This experimental work was supported by equation-of-motion ionisation potential (EOM-IP-CCSD) and effective fragment potential (EFP) methods. The computed vertical detachment energy (VDE) was found to be 7.7 eV.

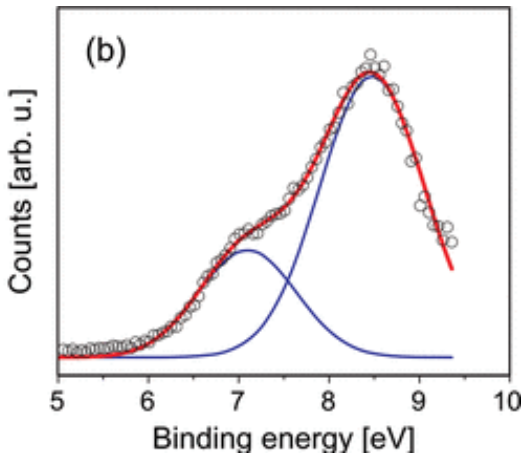

Figure 5.1.1: Reprinted (adapted) with permission from [22]. Copyright 2012 American Chemical Society. Experimental valence photoelectron spectra of 0.75 M aqueous phenolate.

Recently, Boichenko *et al.* developed a new method for calculating the VDEs of anionic biologically relevant chromophores [82]. In this work the first VDE aqueous phenolate was calculated to be 7.3 $\pm$ 0.1 eV. To date this value matches the experimental value (7.1 ev $\pm$ 0.11 ev) the closest. Static UV liquid microjet photoelectron measurements of aqueous phenolate have also been conducted by Scholz *et al*, following excitation at various wavelengths [54]. This study employed photon energies resonant with S_1, but maintained low enough power minimising contributions from bulk water. The ability to use these low powers is a major advantage of UV pump and probe liquid microjet photoelectron spectroscopy in comparison to using higher energy photons, such as extreme UV (EUV). The first VDE in this work was found to be 7.02 $\pm$ 0.09 ev, which is in good agreement with the x-ray mea-

surement [22]. It was also found that the experimental data are only overestimated by around 0.1 eV due to inelastic scattering. This is less than the overestimate observed in liquid water as in the case of phenolate the photoelectrons originate within a nanometer of the surface of the liquid stream, and thus undergo minimal scattering events. UV liquid microjet measurements of aqueous phenolate were also conducted in the work presented in Chapter 3. Briefly, measurements were conducted following photoexcitation at 285 nm (S_1 absorption maximum), 266 nm (high energy edge of S_1 absorption band), 257 nm (between S_1 and S_2absorption bands), and 235 nm (S_1 absorption maximum). The photoelectron spectra resonant with S_1 (285 nm and 266 nm) corresponded to S_1-D_0 detachment. The situation was found to be much more complex for the higher photon energy spectra (257 nm and 235 nm), with multiple detachment continua accessible.

The phenolate anion has also been studied at the aqueous/air interface by Jordan *et al.* [96, 97] and they observed a difference in the dynamics at the surface in comparison to bulk solution. From transient absorption measurements (bulk) [79] geminate recombination results in the solvated electron and a fraction also dissociates. The loss of the solvated electron signal is correlated with the loss in the phenoxy radical. In contrast, at the aqueous/air interface the solvated electron signal decays on a timescale that is an order of magnitude quicker the the phenoxy radical, therefore excluding geminate recombination as a major component of the mechanism. They concluded the electron at the aqueous/air interface is fully solvated, and only a fraction of the electron density is exposed to the vapor phase. This result is compared to liquid-microjet photoelectron experiments spectroscopy of the solvated electron (LJ-PES) where the electron is observed to be at the interface for longer [25, 38, 98, 99].

The aim of the preliminary study presented in this chapter was to measure the timescale for electron emission and recombination in aqueous phenolate using TRPES in a liquid-jet to compare with the detailed literature TAS measurements

[77–80] and the recent sum frequency generation (SFG) measurements at the aqueous/air interface [97].

5.2 Experimental Details

Preliminary time-resolved LJ-PES experiments of aqueous phenolate are presented in this chapter. The details of the experiment are described in detail in Chapter 2. 0.1 mM solutions of aqueous phenolate were prepared in 1.8 mM sodium hydroxide solutions. A high-performance liquid chromatography pump (HPLC), operating at a flow rate of $\sim$ 0.6 mL/min, pumped the aqueous phenolate into the interaction chamber. A 20 μm fused silica nozzle delivered the sample into the vacuum chamber and the liquid maintains laminar flow for around 3-4 mm. Typically this liquid is then removed from the chamber by a heated catcher with a 500 μm position below the nozzle, as described in Chapter 2. Due to a motor problem with the catcher system, the preliminary experiments reported here made use of a cold-trap instead. The liquid sample was captured in the cold-trap and then frozen with liquid nitrogen. The streaming potential (described in Chapter 2) was recorded at the beginning and end of each measurement to determine the value of the vacuum level offset and to check that it had not drifted significantly during the course of the measurements (typically a period of 6 hours). A pump wavelength of 287 nm was used to excite at the maximum of the S_0-S_1 absorption band and a probe of 267 nm was employed to initiate 1 + 1 photodetachment of aqueous phenolate. This accessed 1.54 eV above the lowest detachment threshold. The probe also has sufficient energy to detach the solvated electron. Once fully relaxed the binding energy of the solvated electron is expected to be 3.7 eV [26], therefore the maximum kinetic energy of the fully solvated electron would be expected to be seen at 0.94 eV. Figure 5.2.1 displays a schematic energy diagram illustrating the pump and probe energies and the accessible states. Chapter 2 described the time-resolved beam-line in greater detail.

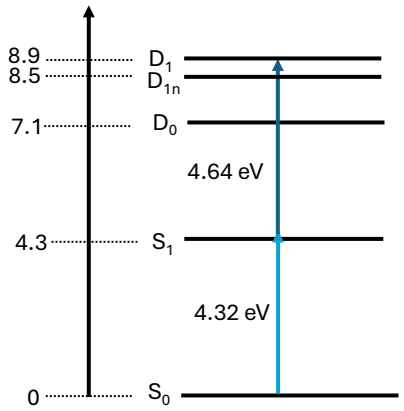

Figure 5.2.1: Schematic energy level diagram illustrating the pump and probe photon energies and the states they can access. The S_1 value is the λ_{max} from the steady-state absorption spectrum. The D_0 and D_1n values are from the x-ray measurements [22].

5.3 Results and Discussion

The data present in this Chapter is the first time-resolved liquid microjet photoelectron data from the Fielding group and will be rerecorded to achieve better quality and more spectra at more pump-probe delay times. This section presents the preliminary data and an initial interpretation that will be revisited when more data has been acquired. The streaming potential before the measurement was found to be -0.024 eV and this decreased by < 0.05 eV during the measurement to -0.070 eV at the end of the measurement. The vacuum level offset before was 0.09 and 0.21 eV after the measurement. Figure 2.5.11 shows the total photoelectron normalised signal over all pump-probe delays until the photoelectron signal disappeared. The signal is best described by a biexponential convoluted with the instrument response function (IRF). The would typically be determined by recording a pump-probe delay scan of Xe at a non-resonant wavelength or of the solvent (in this case water). When the final data is recorded the IRF will be measured, but for now value will be

constrained to be 250 fs as it provided the most reasonable fit with an R^2 of 0.96. 200 fs and 300 fs were also fitted and the provided worse R^2 values of 0.90 and 0.95, respectively. The biexponential has time constants of 0.042 $\pm$ 0.04 ps and 26 $\pm$ 4 ps. The fit has an R^2 value of 0.95. This will be improved in the future by recording more data to reduce any signal fluctuations, but we will continue the discussion using these timescales as a reasonable approximation. It should be noted the shorted time constant is smaller than the value determined for the IRF therefore it is likely there is a fast component to the decay but there is not a large amount of accuracy in this number. Chapter 3 presents our previous transient absorption spectroscopy work [80] and from this we know at 287 nm the solvated electron is formed on two timescales 2.6 $\pm$ 0.1 ps and 23 $\pm$ 1 ps, from vibrationally hot S_1 and vibrationally cold S_1, respectively. The solvated electron has two timescales for geminate recombination and they are: 39 $\pm$ 2 ps and 660 $\pm$ 500 ps . Figure 5.3.1 displays the transient absorption signal (left) integrated over all probe wavelengths and the total photoelectron signal (right). The decay of the photoelectron signal is clearly much faster the the TA data. The TA data has an initial 10 ps rise, whereas the photoelectron signal is at its maximum immediately.

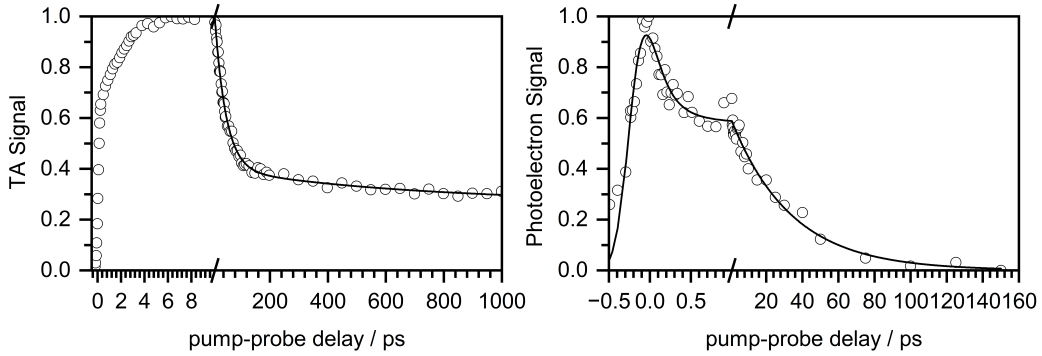

Figure 5.3.1: Left: TA signal of aqueous phenolate following photoexcitation at 287 nm integrated across all probe wavelengths. Biexponential if fit from 10-1000 ps with time constants 39 $\pm$ 2 ps and 660 $\pm$ 500 ps. The fit has an R^2 value of 0.99. **Right:** Pump-probe delay scan following 1+1 resonant detachment of 0.1 mM aqueous phenolate with 1.8 mM NaOH present to deprotonate phenol and minimise the streaming potential. $\lambda_{\text{pump}} = 287$ nm and $\lambda_{\text{probe}} = 267$ nm. The data is fit to a biexponential with lifetimes of 0.042 ± 0.04 ps and 26 ± 4 ps convoluted with the IRF of 0.25 ps. The fit has an R^2 value of 0.96.

In order to understand the timescales observed from our pump-probe delay scan the static spectra at different pump-probe delay times need to be analysed. This will tell us how the kinetic energy distribution changes as a function of pump-probe delay time. Only five spectra were obtained, including the one at time-zero. In order to fully understand the dynamics more spectra at different pump-probe delay times will be recorded in the future. Figure 5.3.2 displays the near time-zero pump plus probe spectrum (black), pump-only spectrum (blue), probe-only spectrum (green), and the isolated two-colour signal (purple).

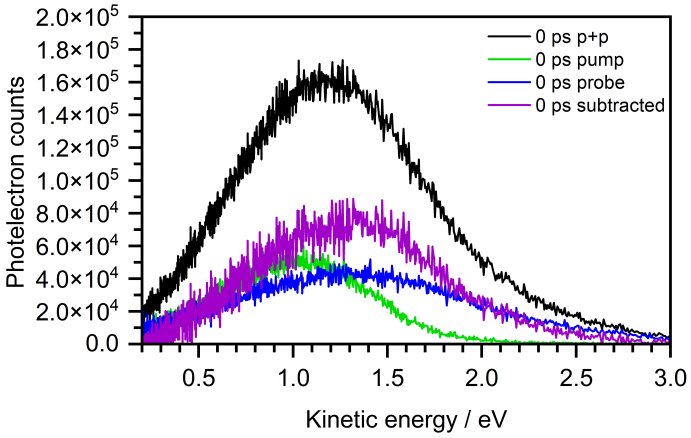

Figure 5.3.2: Near time-zero spectra: pump plus probe spectrum (black), pump-only spectrum (blue), probe-only spectrum (green), and the isolated two-colour signal (purple). $\lambda_{\text{pump}} = 287$ nm and $\lambda_{\text{probe}} = 267$ nm.

Figure 5.3.3 displays the photoelectron spectrum at near zero pump-probe delay time. The static resonance enhanced 266 nm (blue) spectrum and the static 287 nm spectrum are also displayed. The two-colour spectrum (black) resembles the shape of the 266 nm probe-only spectrum and both have approximately the same maximum eKE. In our previous work on the resonant enhanced 1+1 photodetachment of aqueous phenolate at 285 nm (*via* S_1) [80], the feature was fit with a single Gaussian function with maximum eKE at 1.06 $\pm$ 0.07 eV and was assigned to be S_1-D_0 detachment. The same was said for resonant enhance 1+1 photodetachment at 266 nm, with a maximum eKE at 1.25 $\pm$ 0.07 eV. The two-colour spectrum is not as broad as the probe-only and at near-time zero there are three possible contributions to the spectrum. They are: two photon absorption of the pump, two photon absorption of the probe and absorption of one photon of pump and probe. All these possibilities are resonant with S_1. Figure 5.3.4 illustrates all these possibilities.

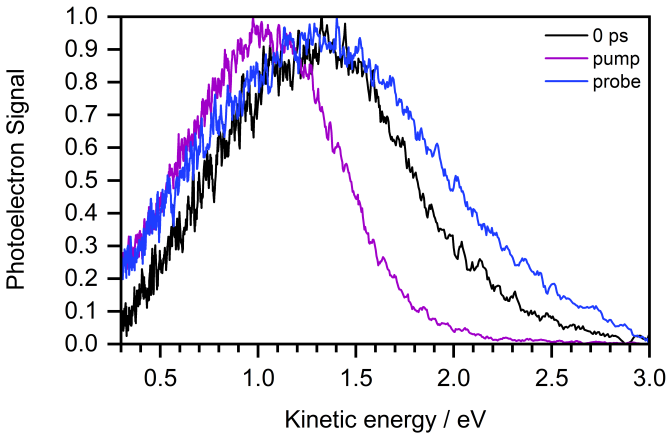

Figure 5.3.3: Two colour photoelectron spectrum of 0.1 mM phenolate with 1.8 mM NaOH at 0 ps pump-probe delay time (black). One colour photoelectron spectra of of 0.1 mM phenolate with 1.8 mM NaOH after 287 nm (purple) photoexcitation and 266 nm (blue) are plotted for comparison purposes.

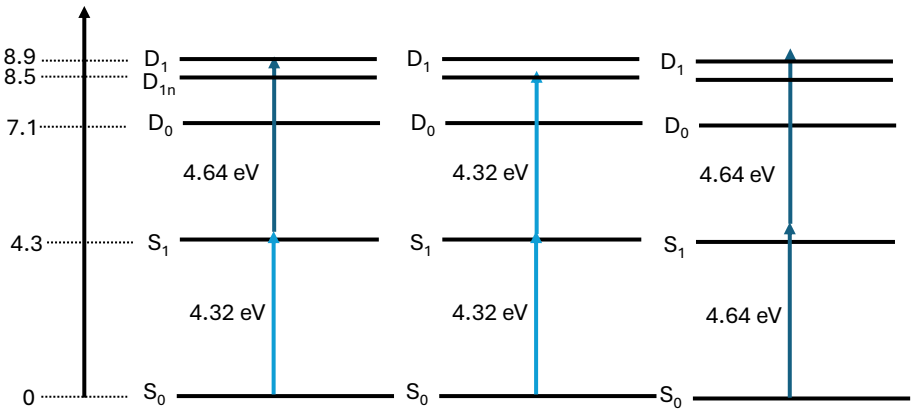

Figure 5.3.4: Schematic energy level diagram showing all the possible contribution to the phototelectron spectrum of aqueous phenolate at time zero. **Left:** Illustrates the process of resonant photodetachment when there is one pump photon (light blue) and one probe photon (dark blue). **Middle:** Illustrates the process of resonant photodetachment when there is two pump photons. **Right:** Illustrates the process of resonant photodetachment when there is two probe photons.

Figure 5.3.5 displays the two colour photoelectron spectrum of aqueous phenolate at a 0 ps pump-probe delay time. Recorded following photoexcitation with $\lambda_{pump} = 287$ nm and $\lambda_{probe} = 267$ nm. The pump energy is resonant with the S_0-S_1 transition. The spectrum is fit to two Gaussian functions providing a R^2 value of 0.98. The Gaussians are centred at 0.78 and 1.35 eV and have FWHM values of 0.47 and 0.87 eV, respectively. The values are summarised in Table 5.3.1 and 5.3.2 .

Table 5.3.1: Summary of the one-photon binding energies at 0 ps, data displayed in Figure 5.3.5.

λ_{pump} / nm (hν)	λ_{probe} / nm (hν)	eKE	FWHM	hν_{probe} - eKE	hν_{pump} - eKE
287 (4.32)	266 (4.66)	0.79	0.47	3.87	3.53
287 (4.32)	266 (4.66)	1.34	0.87	3.30	2.98

Table 5.3.2: Summary of the two-photon binding energies at 0 ps, data displayed in Figure 5.3.5.

eKE	(hν_{probe}+hν_{probe}) - eKE	(hν_{pump} +hν_{pump}) - eKE	(hν_{pump}+hν_{probe}) - eKE
0.79	8.53	7.85	8.19
1.34	7.98	7.30	7.64

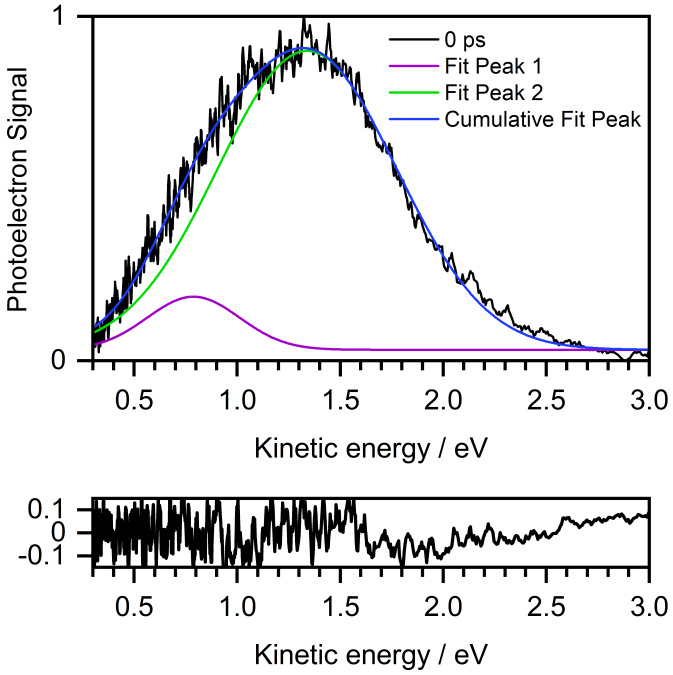

Figure 5.3.5: Top: Two colour photoelectron spectrum 0.1 mM Phenolate with 1.8 mM NaOH at 0 ps pump-probe delay time. The spectral line shape is reproduced by fitting two Gaussian functions. **Bottom:** Displays the residual of the fit.

Figure 5.3.6 is an energy level diagram of aqueous phenolate. At time zero due to the possibility of two photon absorption of the pump, two photon absorption of the probe, and absorption of one photon of the pump and the probe, the spectrum is quite complex. Looking at table 5.3.2 the higher kinetic energy feature, for all combinations of pump/probe, the binding energies are all higher than the threshold for detachment from D_0. Whereas, the lower kinetic energy feature, if two probe pulses are absorbed, could be enough energy for D_{1n} detachment.

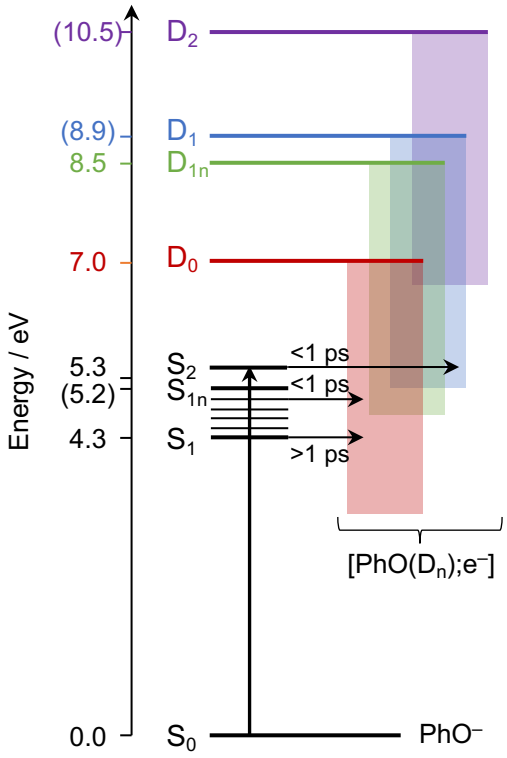

Figure 5.3.6: Schematic energy level diagram illustrating the different photooxidation pathways in aqueous phenolate and the timescales obtained from TAS in our previous work [80]. The numbers not in parenthesis are the λ_{max} values obtained from the steady-state absorption spectrum and the VDEs obtain from UV (D_0) and X-ray (D_{1n}) liquid microjet photoelectron spectroscopy measurements. [22, 54] Values in parenthesis are calculated VDEs and VEEs. [80, 82]

Now that the t= 0 *ps* spectrum has been considered the spectra at different pump-probe time delay can be examined to understand how the kinetic energy distribution changes with time. Figure 5.3.7 displays the two colour photoelectron spectrum 0.1 mM Phenolate with 1.8 mM NaOH at four pump probe delay times.

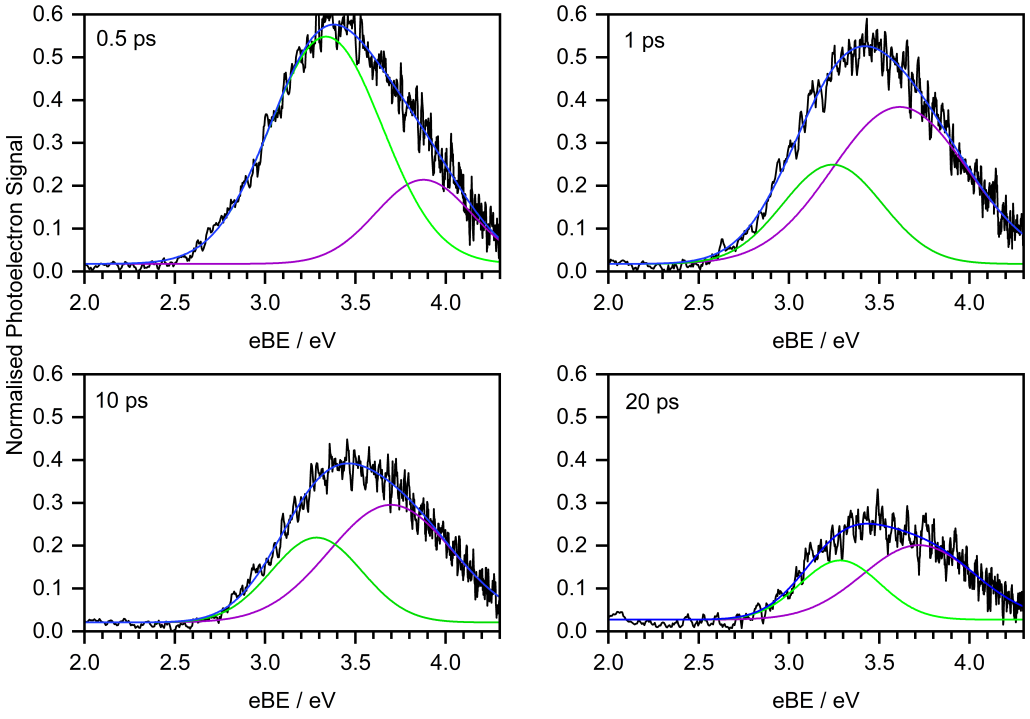

Figure 5.3.7: Two colour photoelectron spectrum 0.1 mM aqueous phenolate with 1.8 mM NaOH at four pump probe delay times. $\lambda_{\text{pump}} = 287$ nm and $\lambda_{\text{probe}} = 266$ nm.

With increasing pump-probe delay time the feature with the lower binding energy (eBE) decays and as it does the eBE remains constant and the width of the lower eBE peak narrows. The width of the entire photoelectron spectrum increases with pump probe delay time. The higher binding energy peak within the first picosecond increases in amplitude while shifting to lower eBE and broadening. After 1 ps this feature amplitude then decays the eBE remains constant. This is summarised in Figure 5.3.8, where the eBE each feature is plotted as a function of time.

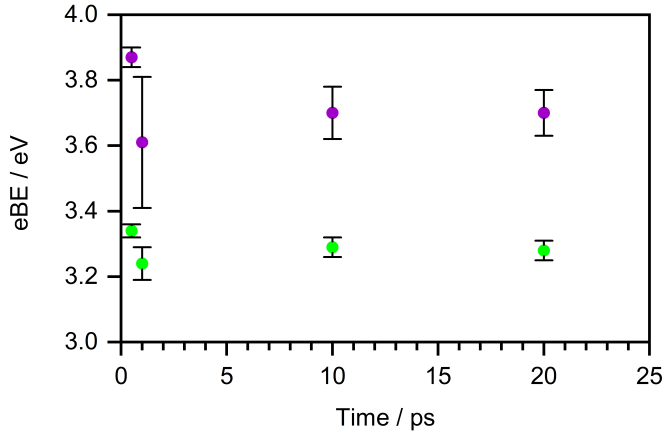

Figure 5.3.8: Plot of the eBE of each contribution to the photoelectron spectrum 0.1 mM Phenolate with 1.8 mM NaOH as a function of pump-probe delay time.

The binding energy of the solvated electron once equilibrated is known to be $\sim$ 3.7 eV [26, 100]. Although, the eKE of the solvated electron would shift from higher eKE to lower and therefore, lower eBE to higher. The eBE of the higher eBE contribution possibly could be from the solvated electron, although to be certain further experiments should be completed acquiring more data points and also making use of the strong electron quencher KNO_3. The lower eBE contribution matches the previously reported one photon binding energies after resonance enhanced detachment with 285 nm [54]. This feature was assigned to $1^1\pi\pi^*$-D_0 .

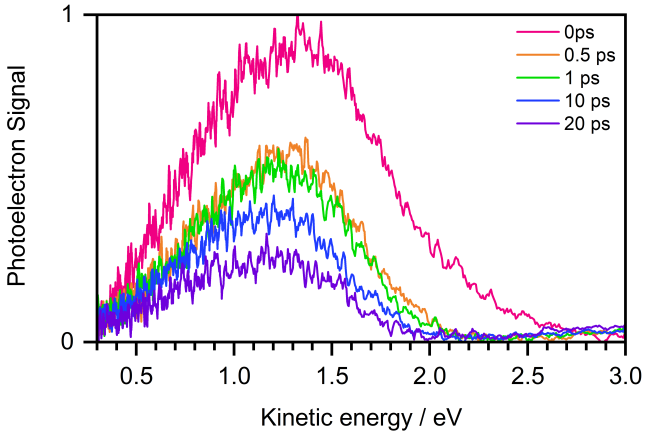

Figure 5.3.9: Static spectra of 0.1 mM Phenolate with 1.8 mM NaOH at varying pump-probe delay times. Pump only and probe only signal have been subtracted. Spectra are smoothed with a 5 point moving average.

Figure 5.3.9 displays all the recorded 1+1 resonance enhanced photoelectron spectra of 0.1 mM Phenolate with 1.8 mM NaOH at varying pump-probe delay times. The data is plotted as a function of electron kinetic energy.

5.4 Conclusions and Outlook

In summary, these were the first ever time-resolved photoelectron spectroscopy experiments conducted on the liquid microjet spectrometer at UCL. While the data collected is not sufficient to draw definitive conclusions, the quality is high, and the preliminary results are promising.

While this is still a work in progress, the results suggest that the overall dynamics in a liquid microjet are significantly faster than those observed in bulk aqueous solution. The total photoelectron signal as a function of pump-probe delay was described by a biexponential decay with time constants 0.042 $\pm$ 0.04 ps and 26 $\pm$ 4 ps. In contrast, the corresponding TAS experiments showed timescales for geminate recombination of 50 $\pm$ 3 ps and 490 $\pm$ 200 ps. The substantial difference in timescales between the two experiments may indicate significantly different photochemical processes at the surface. Jordan *et al.* observed at the aqueous/air interface that the solvated electron signal decayed an order of magnitude faster than the phenoxy radical signal, excluding geminate recombination as the mechanism for the loss of electron signal [97]. Molecular dynamics simulations by Scholz *et al.* have shown that phenolate in aqueous solution resides more on the surface than in bulk solution [54]. This, combined with previous findings, suggests that the differing dynamics observed in our experiments may be attributed to phenolate's tendency to sit on the solution's surface. Recording additional static spectra at various pump-probe delay times could provide further insights into these dynamics and help clarify the underlying mechanisms.

Despite more data being required to reach definitive conclusions, it seems highly likely that the two components of the photoelectron spectra correspond to the lower

eBE component originating from the $1^1\pi\pi^*$-D_0 state and the higher eBE component from the solvated electron. The eBE is consistent with the literature value for the solvated electron [26] and $1^1\pi\pi^*$-D_0 is consistent with previous work in the group.

The contribution of the solvated electron to the photoelectron spectrum can be confirmed by using a strong electron quencher, such as potassium nitrate. To fully understand the dynamics and enable a proper comparison with the TAS data, photoelectron spectra should be recorded at many more pump-probe delay times.

Chapter 6

Unravelling the Electronic Relaxation Dynamics of Model Firefly Bioluminescent Emitters

The Firefly has one of the brightest bioluminescence reactions with a quantum yield of $\phi = 0.41$ [13]. Oxidation of D-luciferin, the small molecule that lies at the heart of firefly bioluminescence, is catalysed by oxygen in the presence of ATP and the Mg^{2+} ion forming the chemiluminescent product keto-oxyluciferin. The high quantum yield has made oxyluciferin a valuable tool for bioluminescent imaging. Naturally, oxyluciferin can exist in six different chemical forms due to keto/enol tautomerisation and deprotonation of the phenol and enol groups. Among these forms, the phenolate-keto form of oxyluciferin is of particular interest because it exhibits the longest wavelength emission [101]. Consequently, the work described in this chapter will focus on that specific form. Bioluminescent probes have applications in *in vivo* imaging in medicine [102]. To design new probes for deeper tissue imaging, the emission maximum needs to be red-shifted further and made brighter. This shift would be advantageous for *in vivo* imaging because, in this spectral region, biological tissues exhibit less signal attenuation due to hemoglobin and melanin. Here, we use femtosecond transient absorption spectroscopy to investigate dynamics of the emission of the anionic forms of oxyluciferin and infraoxyluciferin in aqueous buffer. Infraoxyluciferin is an analogue of oxyluciferin with red-shifted emission

maximum. We compare the dynamics of each molecule with an aim to understand why oxyluciferin is a much more efficient emitter than infraoxyluciferin. By improving our detailed understanding of the electronic relaxation of the molecular unit that lies at the heart of this important bioluminescence system, we will learn how to design new efficient tools for bioluminescent imaging.

6.1 Motivation

Bioluminescence is a phenomenon that occurs within living organisms, resulting in the production and emission of light. This phenomenon has been observed in several species of jellyfish, worms, and squid [13, 71, 101, 103–107]. The reaction is a form of chemiluminescence meaning the production of light is catalysed by a chemical reaction. The enzyme present, luciferase, catalyses the oxidation of the substrate, luciferin, in the presence of adenosine triphosphate (ATP).

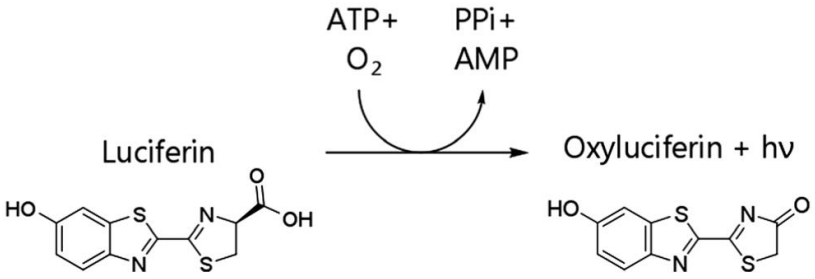

Figure 6.1.1: The process of forming oxyluciferin from luciferin. The reaction is catalysed by oxygen in the presence of ATP and the Mg^{2+} ion. Reproduced from Ref [108] with permission from the Royal Society of Chemistry.

The North American *Photinus pyralis* firefly has one of the brightest bioluminescence reactions, with a quantum yield of $\Phi = 0.41$ [13]. In the case of fireflies, the adenylation and oxidation of D-luciferin is catalysed by oxygen in the presence of ATP and Mg^{2+} ion, see Figure 6.1.1. In the aqueous solution, the firefly oxyluciferin can exist in six chemical forms as a result of keto-enol tautomerisation and deprotonation of the hydroxyl groups [101, 104, 109, 110]. The keto and enol forms

exist in an equilibrium with one another. Figure 6.1.2 displays the structures of the keto and enol forms of oxyluciferin.

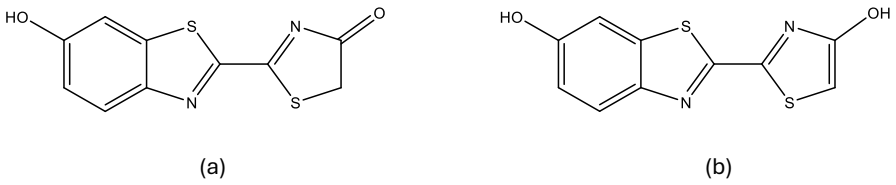

Figure 6.1.2: Displays the (a) keto (b) enol structures of oxyluciferin.

This chapter will focus solely on the phenolate-keto form of oxyluciferin, as it has been previously reported to have the most red-shifted emission [101, 103]. Infraoxyluciferin (iOL^-) will also be investigated which is an analogue of oxyluciferin with an extended alkene chain. Previously, infraluciferin has been synthesised by Anderson *et al.* [111] and it was found to have a bioluminescent emission at > 700 nm. iOL^- is an ideal candidate for *in vivo* and *in vitro* imaging, due to its near infra-red emission (nIR) wavelength. The use of luciferins is desirable in applications such as bioluminescent imaging, due to their high quantum yield. Bioluminescent imaging is advantageous over other fluorescence imaging techniques as there are no background counts, since no external light source is required. Subsequently, bioluminescent imaging has a higher signal-to-noise ratio than other similar techniques. To further advance bioluminescent imaging, brighter probes with emission wavelengths in the near-infrared are required, to improve *in vivo* tissue penetration [112]. In the case of luciferin its $\lambda_{max} = 558$ nm [13] which unfortunately is absorbed by haemoglobin and melanin, thus reducing the image resolution [113]. Although, the emission maximum of infraluciferin is red-shifted, the fluorescence quantum yield is much lower with a value of 0.27 [111]. Figure 6.1.3 displays the chemical structures of phenolate-keto oxyluciferin (OL^-) and phenolate-keto infraoxyluciferin iOL^-, the two molecules that are the focus of this chapter. Both molecules are synthesised by Dr. Marlowe Graham in Prof. James

Anderson's group at UCL and a cyclopropyl group is added to the thiazole group to block the keto-enol tautomerisation in the excited state.

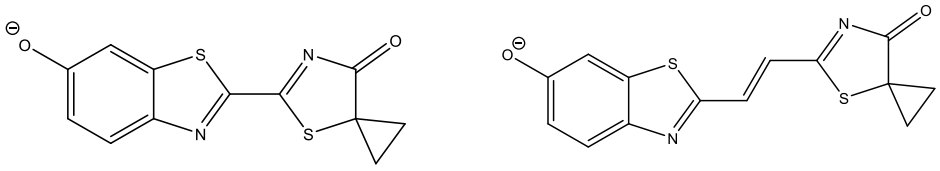

Figure 6.1.3: Chemical structure of (a) phenolate-keto oxyluciferin and (b) phenolate-keto infraoxyluciferin.

The microenvironment plays a large role in the efficiency of luminescence [103, 104] and is thus essential in defining the electronic properties of luciferin. For example, in bioluminescent beetles, the color of emission can vary from green to red even though all species use the same luciferin [108, 114, 115]. Previous studies have altered luciferins to shift the emission further into the near-infrared, but consequently, the quantum yield of the emission was reduced [116]. For the logical design of new red-shifted bioluminescent probes, understanding the fundamental electronic structure and relaxation dynamics of the luciferins is crucial. Anderson *et al.* synthesised infraluciferin, an alkene-linked analogue of luciferin, which has an emission maximum of > 700 nm [111]. They observed a reduction in emission by 3–4 orders of magnitude and identified two peaks in the emission spectrum. The major peak was slightly blue-shifted compared to the emission observed with luciferin, while the minor peak was around 800 nm.

There have been several previous gas-phase spectroscopic studies investigating luciferins [104, 108, 117]. Støchkel *et al.* employed action spectroscopy to study the isolated firefly luciferin *in vacuo* and also with one water molecule present [117]. It

was determined a single water molecule strongly perturbs the electronic structure, such that the absorption spectrum was significantly altered. For luciferin *in vacuo*, a broad absorption maximum was observed at 548 ± 10 nm. When a water molecule was present, this absorption maximum was blue-shifted by 50 nm. In addition to the experimental work, molecular dynamics simulations and time-dependent density functional theory calculations could reproduce these experimental peaks and indicated that the preferred binding site for the water molecule is on the phenolate oxygen of the anion. Woodhouse *et al.* investigated the excited-state dynamics of luciferin and infraluciferin using photoelectron spectroscopy and quantum chemistry calculations [108]. It was observed that following photoexcitation in the range of 357–230 nm, internal conversion to the S_1 ($^1\pi\pi^*$) state from higher-lying electronic excited states competes with electron detachment. In comparison, in infraluciferin, it was additionally found that decarboxylation also competes with internal conversion and electron detachment. The experimental work was supported by calculations (EOM-IP-CCSD) to determine the VDEs and VEEs. Luciferin and infraluciferin were found to have similar VDEs, although the vertical excitation energies of the electronically excited states of infraluciferin were found to be more red-shifted. It was also observed for both molecules that resonant excitation of S_3 ($^2\pi\pi^*$) led to rapid IC back to S_1 ($^1\pi\pi^*$), followed by electron detachment. In infraluciferin, decarboxylation also competed with this process. Patel *et al.* conducted a photoelectron spectroscopic study to investigate the electronic structure and relaxation dynamics of three model oxyluciferin anions supported by electronic structure calculations [104]. Various deprotonated forms were investigated through systematic methylation, revealing that the deprotonation site significantly impacts the relaxation mechanism following electronic excitation. The keto form was observed to undergo IC to the fluorescent S_1 state, whereas evidence suggested that the enol and enolate forms undergo internal conversion to a dipole-bound state.

There have been several time-resolved spectroscopic studies of oxyluciferin in the condensed phase. Snellenburg *et al.* [9] investigated oxyluciferin in the firefly

enzyme luciferase *via* time-resolved fluorescence spectroscopy. This study aimed to understand interactions between oxyluciferin and the active site. Steady-state absorption and emission spectra of oxyluciferin in an aqueous buffer solution of luciferase at pH 6.8, 7.0 ,7.8 and 8.3 were recorded. As observed in aqueous solution, the absorption maximum red-shifts with increasing pH due to the deprotonation of oxyluciferin. At neutral pH in aqueous solution, oxyluciferin exhibits two emission bands: a weak shoulder around 450 nm corresponding to the neutral species, and a major peak at 550 nm associated with the conjugate base formed by excited-state proton transfer. This behaviour was also observed in enzyme. Increasing the pH resulted the presence of the 450 nm reducing, due to the deprotonation of the ground state. Time-resolved fluorescence spectra of oxyluciferin in enzyme were recorded at pH 6.8, 7.0 ,7.8 and 8.3, following 372 nm and 467 nm photoexcitation. The spectra were globally analysed due to the large number of kinetics contributing to the total signal. The analysis showed contributions from the multiple chemical forms of oxyluciferin. Presiado *et al.* [118] recorded time-resolved and steady-state emission spectra to study dehydroluciferin to model the enol from and D-luciferin to model the keto form. The excited state proton transfer (ESPT) rates were investigated in water/ethanol mixtures and with increasing methanol concentration the rate decreases. They also investigated dehydroluciferin in aqueous solution with HCl and found that the acid affected the emissions of both the protonated and deprotonated forms. The first TA study of the substrate luciferin was carried out by Cherednikova *et al.* and had picosecond time resolution [119]. They observed the emission signal reaching its maximum after 100 ps and suggested that luciferin existed in two chemical forms in the excited state. A more recent and the only other TA study to our knowledge by Gosset *et al.* [101] employed femtosecond-TAS and time-resolved fluorescence spectroscopy to study the excited-state proton transfer (ESPT) reactions and display the keto-enol conversion of oxyluciferin as a function of pH. Figure 6.1.4 shows the four model compounds they studied to mimic the keto and enol forms. The pathway in competition is synthetically blocked.

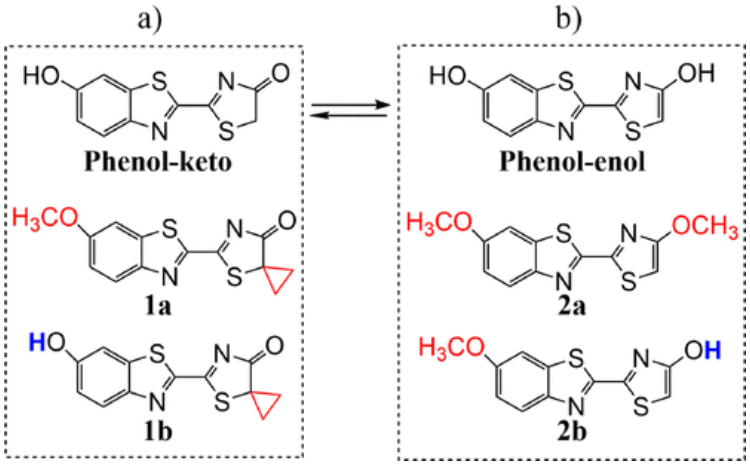

Figure 6.1.4: Reprinted (adapted) with permission from [101]. Copyright 2020 American Chemical Society. The four compounds studies by Gosset *et al.* to mimic the keto and enol forms of oxyluciferin.

All experiments were performed in pH 5 and pH 11 aqueous buffers to avoid both the protonated and deprotonated forms existing. Molecules 1a and 1b were chosen to mimic the keto form. Molecule 1a represents the phenol form as the hydroxyl group is replaced with a methoxy group (see Figure 6.1.4, in red) and thus deprotonation in S_0 and S_1 is prevented. In contrast, molecule 1b allows the investigation of the deprotonation and protonation of the phenol group. The same can be said for molecules 2a and 2b, except they are the enol forms. Our studies will focus on the molecule in the form of 1b at pH 11. The absorption and emission maxima of 1a are 388 nm and 525 nm, respectively. In 1b at pH 11 the absorption maximum is red-shifted to 482 nm and the emission to 640 nm. The emission maximum at pH 5 for 1b is also a maximum at 640 nm, thus suggesting it is the same emissive state. Following photoexcitation at 400 nm between the first and second absorption bands two transient features were observed. The first, is an ESA centered at 550 nm and the second is SE centred at 640 nm. These are said to be the S_1 signatures of the phenolate-keto form of oxyluciferin. The transient absorption spectrum is displayed in Figure 6.1.5.

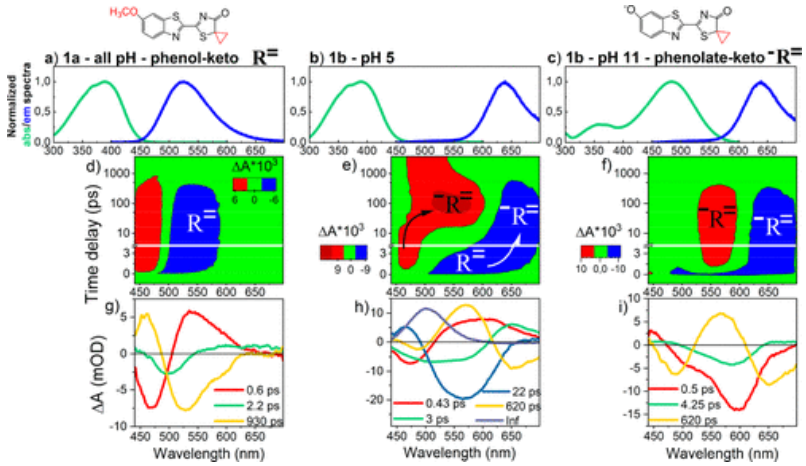

Figure 6.1.5: Reprinted (adapted) with permission from [101] Copyright 2020 American Chemical Society. Spectra on the right are for the phenolate-keto oxyluciferin in aqueous buffer solution at pH 11 **Top:** (c) Steady-state absorption (green) and emission (blue) spectra of phenolate-keto oxyluciferin in aqueous buffer solution at pH 11. **Middle:** (f) TAS spectrum of phenolate-keto oxyluciferin in aqueous buffer solution at pH 11, following 400 nm photoexcitation. **Bottom:** (i) Decay associated spectra extracted from global analysis of the transient absorption spectrum.

Through a detailed global analysis of the TA data three time scales were determined for the phenolate-keto form of oxyluciferin. The first was 620 ps, obtained from fluorescence decay measurements, and was fixed in the global analysis. There was also two shorter time constants, 0.5 and 4.25 ps, and they were assigned to spectral relaxations they assumed were likely due to vibrational and solvent relaxation.

Ghose *et al.* systematically studied the steady-state and time-resolved emission spectra of oxyluciferin in aqueous solution [103]. Their investigation identified the emission spectra for each distinct form of the molecule, as presented in Figure 6.1.6.

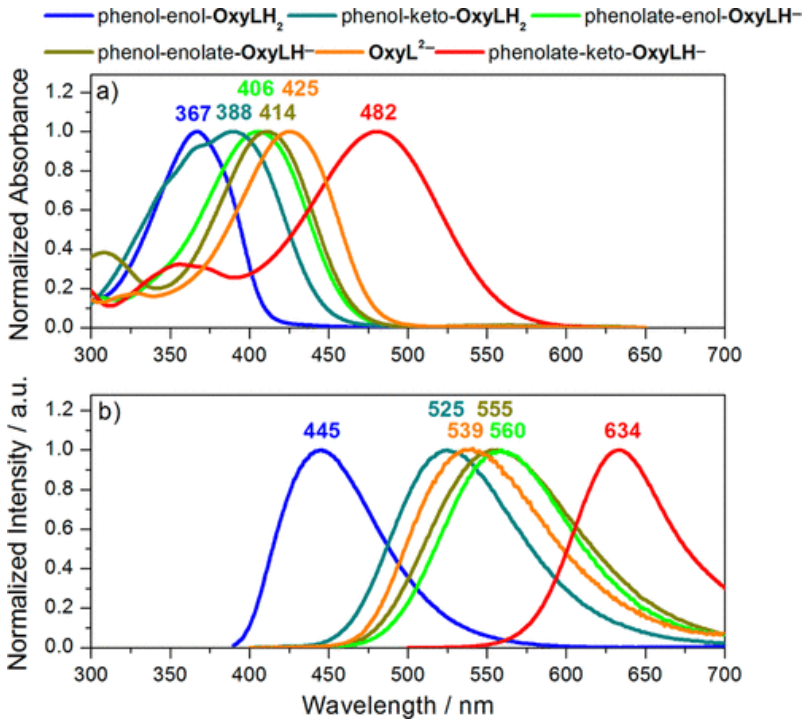

Figure 6.1.6: Reprinted (adapted) with permission from [103]. Copyright 2015 American Chemical Society. Absorption (top) and emission (bottom) spectra of all the forms of the firefly oxyluciferin.

This work confirmed that the phenolate-keto form of oxyluciferin has the most red-shifted emission maximum at 634 nm. They also studied the time-resolved fluorescence behavior of all chemical forms. It was found that by monitoring the 640 nm emission in pH 10 aqueous buffer of the phenolate-keto form, the fluorescence lifetime was 0.6 ns. This is several times faster than the phenolate-enol emission which has a 4.9 ns lifetime.

This chapter will present the steady-state absorption, emission and TA spectra of OL^- and iOL^-. By studying the excited state dynamics of both molecules we hope to understand why the fluorescence quantum yield of iOL^- is significantly less than that of OL^-. Understanding the excited state-dynamics could aid the design of new nIR bioluminescent probes. Our investigations will be isolated to the phenolate-keto form of oxyluciferin, due to the maximum of the emission wavelength being the most red-shifted [103] and it has been considered the most plausible form as an emitter [103, 120, 121].

6.2 Experimental Details

6.2.1 Transient-Absorption Spectroscopy

TA spectra were obtained using the experimental set-up outlined in Chapter 2, Section 2.2. Briefly, TA spectra were recorded following photoexcitation at 481 nm and 551 nm for iOL^- and for OL^- after photoexcitation at 349 nm and 476 nm. Each pump wavelength was generated from the optical parametric amplifier (OPA) and then attenuated at the sample using a neutral density filter to achieve a pulse energy of approximately 100 nJ. This Chapter presents experiments that use both the visible and UV probes to give a combined probing wavelength range of 350-720 nm. The visible probe was used for iOL^-, while the UV probe was employed for OL^- because iOL^-'s steady-state emission falls outside the UV probing region. The relative polarisations of the pump and probe beams were set to be at the magic angle (54.7°). This ensures effects from rotations are not measured. Experiments were carried out at pH 10 and a concentration of 870 μM of iOL^- was used and 9.7 μM of OL^-. A 2 mm cuvette was used and this was rastered and the sample was also stirred with a magnetic stirrer bar. A cuvette was used instead of a Harrick flow cell due to limitation in sample volume available because the molecules were specially synthesised and solutions prepared by Dr Marlow Graham from Professor Jim Anderson's group on the morning before each measurement. Moreover, the sample could only be used for a short period before deteriorating. This could be monitored by recording a steady-state emission spectrum.

6.3 Results and Discussion

6.3.1 Steady-State Absorption

Fig. 6.3.1 displays the normalised steady-state absorption spectra of 10.3 μM OL^- (pH 10) and 870 μM iOL^- (pH 10). Both molecules have an absorbance maxima around 480 nm. The first absorption band of iOL^- is $\sim$ 30% broader than the equivalent in OL^-.

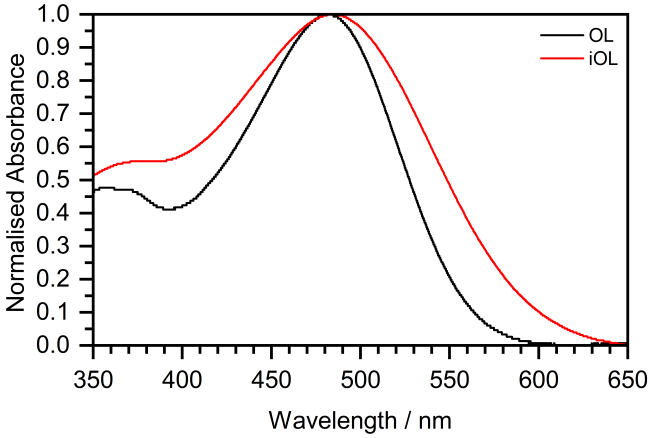

Figure 6.3.1: Normalised steady-state absorption spectra of 10.3 μM OL^- at pH 10 (black) and 870 μM iOL^- at pH 10 (red).

6.3.2 Steady-State Emission Data

Figure 6.3.2 displays the steady-state emission spectra of oxyluciferin at two pump wavelengths, 482 nm (maxima of the first absorption band) and 355 nm (maxima of the second absorption band). Based on the work of Ghose *et al.* [103], we know that the absorption spectrum of OL^- exhibits a dependence on pH. Our recorded spectrum at pH 10 matches their spectrum.

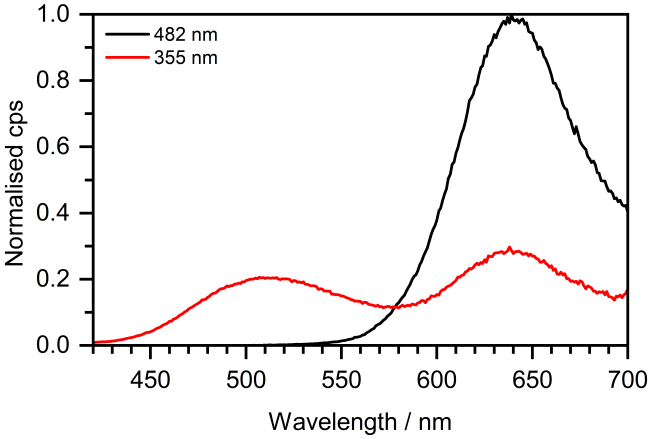

Figure 6.3.2: steady-state emission spectra of 0.97 μM OL^- at two pump wavelengths 482 nm (black) and 355 nm (red). Spectra are normalised relative to the 482 nm emission. All spectra were recorded with a 2 nm slit size.

Following photoexcitation of OL^- at 482 nm (close to the maximum of the first absorbance band), a single emission band is observed, centered around 640 nm. Following photoexcitation of OL^- at 349 nm (close to the maximum of the second ab-

sorbance band) a second emission maxima is revealed, centered around 510 nm. To determine the specific excitation wavelengths responsible for each emission an excitation scan was conducted, see Figure 6.3.3. The scans of excitation wavelengths reveal the longer wavelength emission is present at all excitation wavelengths, but is most prominent on the red-edge of the first absorption band. While the shorter wavelength emission is only present when excited on the blue edge of the absorption spectrum.

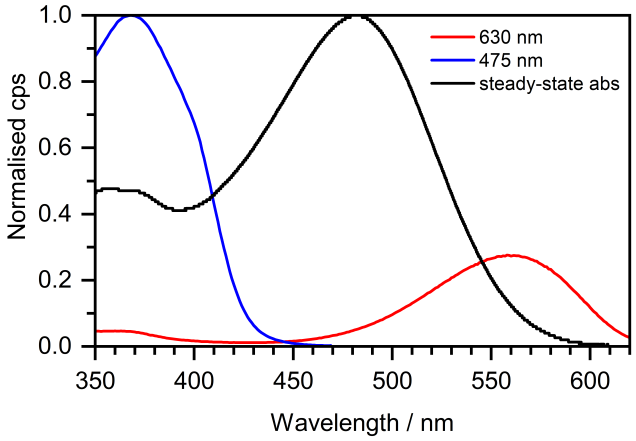

Figure 6.3.3: Excitation scans of 0.97 μM OL^- monitoring two emissions 475 nm (blue) and 630 nm (red). The steady-state absorption spectra is plotted for comparative purposes (black). Excitation scans were recorded with a 2 nm slit size.

First, it should be considered whether the neutral molecule is in equilibrium with the anion at pH 10 and could thus be responsible for the second emission band. The pK_a of OL^- is 7.8 ± 0.1 [103], indicating that there should be less than 1% of the neutral molecule present at pH 10, with a concentration of 0.97 μM. The second emission band around 530 nm has also been observed by Ghose *et al.* [103] and was assigned to be a photoproduct. This emission was observed to be more prominent in basic conditions and its emission maxima was centred at 530 nm in their measurement of oxyluciferin with the substituted cyclopropyl group. They assigned the photoproduct to be the dianionic species which is formed after isomerisation and hydrolysis. The purpose of the cyclopropyl group was to block the keto-enol tautomerisation and thus would prevent the formation of a dianionic species. Ghose *et al.* [103] state that the cyclopropyl group minimised this photoreaction and also

increased the global stability in the ground and excited state. Although, the dianionic species was found to have an emission maximum at 539 nm and in our work the emission is at approximately 510 nm. Additional experimental evidence may be necessary to confirm this assignment. Although, the steady-state emission spectra presented in our work following 355 nm excitation match those recorded by Ghose *et al.*. The scans of excitation wavelengths reveal the longer wavelength emission is present at all excitation wavelengths, while the shorter wavelength emission is only present when excited on the blue edge of the absorption spectrum.

Fig. 6.3.4 displays the steady-state emission spectra of iOL^-. The emission spectra displayed are also dependant on the excitation wavelength.

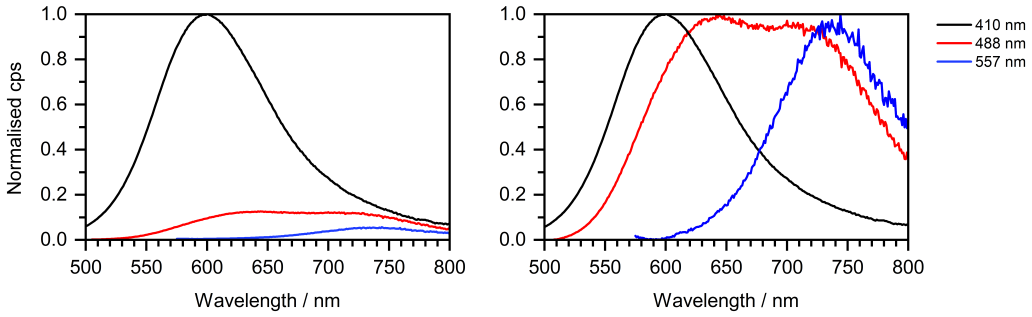

Figure 6.3.4: steady-state emission spectra of 870 μM iOL^- at three pump wavelengths 410 nm (black), 488 nm (red) and 557 nm (blue). **Left:** Spectra are normalised relative to the 410 nm spectrum. **Right:** All spectra are normalised to their maxima. All spectra were recorded with a 3 nm slit size.

As shown in Fig. 6.3.4, the most prominent emission is observed after photoexcitation on the high energy edge of the first absorption band and has an emission maximum at 598 nm. Following photoexcitation near the maxima of the first absorption band an emission spectra with dual peak structure (488 nm) is observed with maxima at approximately 640 nm and 720 nm. Finally, following photoexcitation at the low energy (long wavelength) edge of the first absorption band the emission maximum is observed to be around 740 nm. This is an unusual phenomenon to observe as according to Kasha's rule the emission of a photon will always be from the

lowest lying electronic excited state. The Kasha-Vavilov rule that follows on from Kasha's rule and states that the fluorescence emission spectrum should be independent of excitation wavelength.[122] A classic example of a violation of Kasha's rules is azulene, where fluorescence is observed to be from S_2 because of the large energy gap between S_1 and S_2 (1.5 eV) resulting in relatively slow S_2 to S_1 internal conversion (Type I anti Kasha) [122, 123].

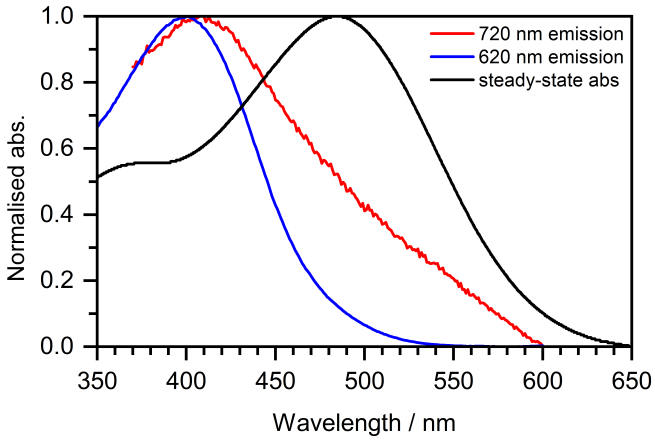

Figure 6.3.5: Excitation scans of 870 μM iOL^- monitoring two emissions 620 nm (blue) and 720 nm (red). The steady-state absorption spectra is plotted for comparative purposes (black). Excitation scans were recorded with a 3 nm slit size.

An alternative interpretation for the dual emission peaks could be that two electronic excited states are involved. As the emission spectra of OL^- are dependant on excitation wavelength and the excitation scans of the two emissions are different (see Fig 6.3.3.) this could possibly suggests that two electronic excited states are involved. The maximum 720 nm fluorescence signal and maximum 620 nm fluorescence signal are both observed at approximately the same excitation wavelength, with the maximum position of the 720 nm emission slightly red-shifted by about 20 nm. This could suggest that if there are two different emitting states then they are likely very close in energy. Upon re-examining the steady-state emission spectra (see Figure 6.3.2), the lowest energy excitation results in the most red-shifted emission peak, whereas the highest excitation energy predominantly produces the most blue-shifted emission peak, with minimal contribution from the redder one. This would indicate Type II or Type III anti-Kasha emission, see Figure 6.3.6. There is

also the possibly of a photoproduct, like previously suggested for OL^-, causing the second emission feature. However, an alternative interpretation involving two emitting states is also plausible for both molecules. The transient absorption spectra presented in the next Section will provide further insight into this photoluminescence behaviour.

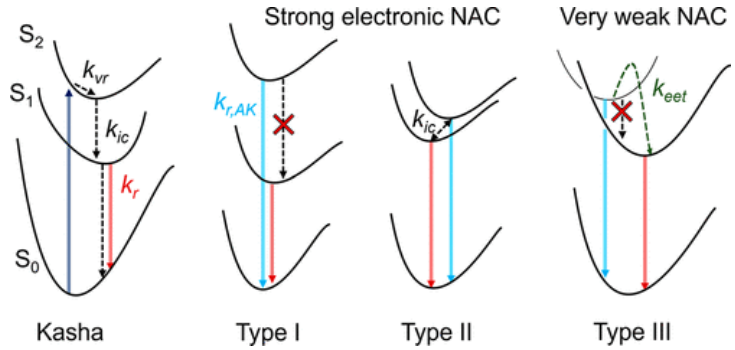

Figure 6.3.6: Reprinted with permission from [122]. Copyright 2022 American Chemical Society. Schematic diagram representing Kasha and anti-Kasha emission. k_{vr} is vibrational relaxation, k_{ic} is internal conversion, and k_{eet} is excitation energy transfer. NAC is non-adiacbatic coupling.

6.3.3 Transient Absorption Spectra of Oxyluciferin

Figure 6.3.7 displays the TA spectra of OL^- after 476 nm (close to the first absorption maxima) photoexcitation (left) and 348 nm (close to the second absorption maxima) photoexcitation (right). In both spectra, five features can be observed. First focusing on the 476 nm data (left), the two features on the reddest edge of spectrum have been assigned in the literature by Gosset *et al.* This was a TAS study of OL^- in aqueous buffer at pH 11 following photoexcitation between the two absorption maxima at 400 nm [101]. The negative feature with a maximum at approximately 640 nm is previously assigned to SE, this is in good agreement with the steady-state emission spectra (Fig. 6.3.2). The small ESA centred around 570 nm was previously assigned to the S_1 signature of the phenolate-keto form of OL^-, which we would be in agreement with. The negative feature around $\sim$ 480 nm matches well with the steady-state absorption spectrum and therefore, we have assigned this as a GSB. This feature was not observed in the previous study [101]. The probe employed in the previous study only went to 450 nm in the UV. Here we

have another 100 nm and in addition to revealing the GSB, it also this revealed two additional ESA features. The 349 nm (close to the second absorption maxima) data has the same five absorption features. The steady-state emission spectrum of the 349 nm data has an additional peak on the blue edge, this is not observed clearly in the TA data. The steady-state absorption spectra overlaps with the blue peak of the steady-state emission spectrum, therefore the GSB and SE bands will also be overlapped in the TA spectrum and thus are hard to separate.

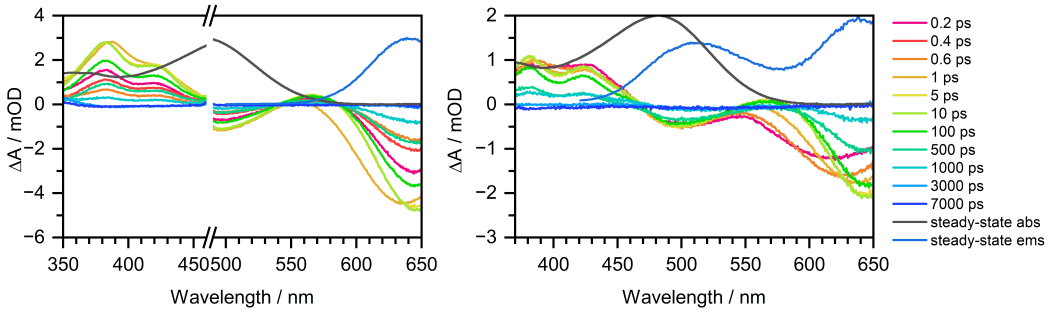

Figure 6.3.7: 9.7 μM TA spectra of OL^- displayed at various pump-probe time delays shown in the legend. **Left:** Spectrum after 476 nm photoexcitation. Steady-state absorption (black) and steady-state emission spectra are overlaid. They are normalised to have maxima at 3 mOD. **Right:** Spectrum after 355 nm photoexcitation. Steady-state absorption (black) and steady-state emission spectra are overlaid. They are normalised to have maxima at 2 mOD.

Figure 6.3.8 illustrates that at a pump-probe delay of 10 ps the 476 nm and 349 nm data look remarkably similar.

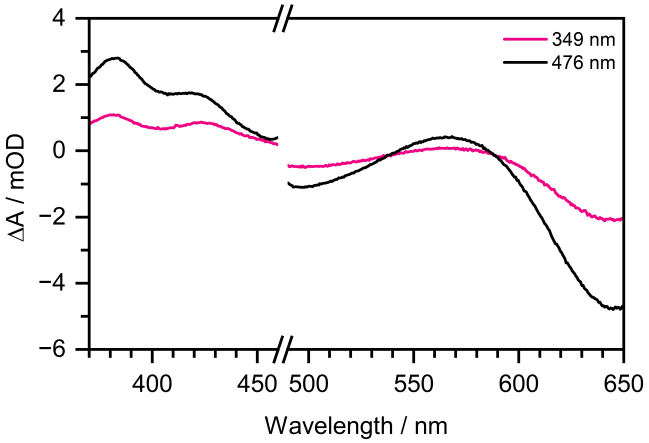

Figure 6.3.8: OL TA spectra at a pump-probe delay of 10 ps for 476 nm (black) and 349 nm (blue) photoexcitation.

476 nm Data

First, to obtain an overview, kinetic traces of each feature were extracted by averaging over a 5 nm window and plotting the average amplitude over all pump-probe time delays. Figure 6.3.9 displays the extracted kinetics.

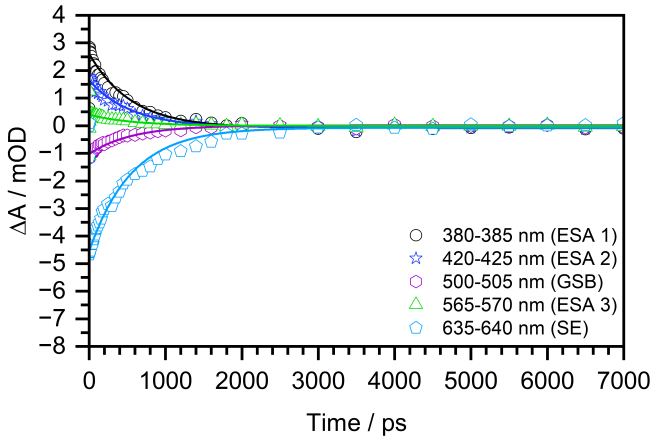

Figure 6.3.9: OL^- kinetic traces following photoexcitation at 476 nm, extracted for each feature in the TA spectrum. Kinetic traces were globally fit to an exponential function convoluted with the IRF of 0.11 ps (extracted from Surface Xplorer software, see Chapter 2). The lifetime of the exponential was found to be 550 $\pm$ 20 ps. The R^2 of the overall fit was 0.99.

As a first approximation this is a reasonable way to look at the data. It is clear every spectral feature decays on the same timescale, suggesting that they all originate from the same electronic state. One thing to note is it is clear from Figure 6.3.7

that at very early pump-probe time delays the SE appears to spectrally narrow and red-shift. There is an isobestic point at 575 nm arising from the superposition of ESA 3 and the SE. There is another isobestic point around 475 nm arising from the superposition of ESA 3 and the GSB. This is present immediately in the data following 476 nm photoexcitation, but not in the 349 nm data. Next, we chose to use the KOALA software to fit the five features of the spectrum. The data was fit in two halves: 350-540 nm (see Fig. 6.3.10) and 500-650 nm (see Fig. 6.3.11). This was done to avoid the scattered light from the pump laser in the middle of the TA spectrum.

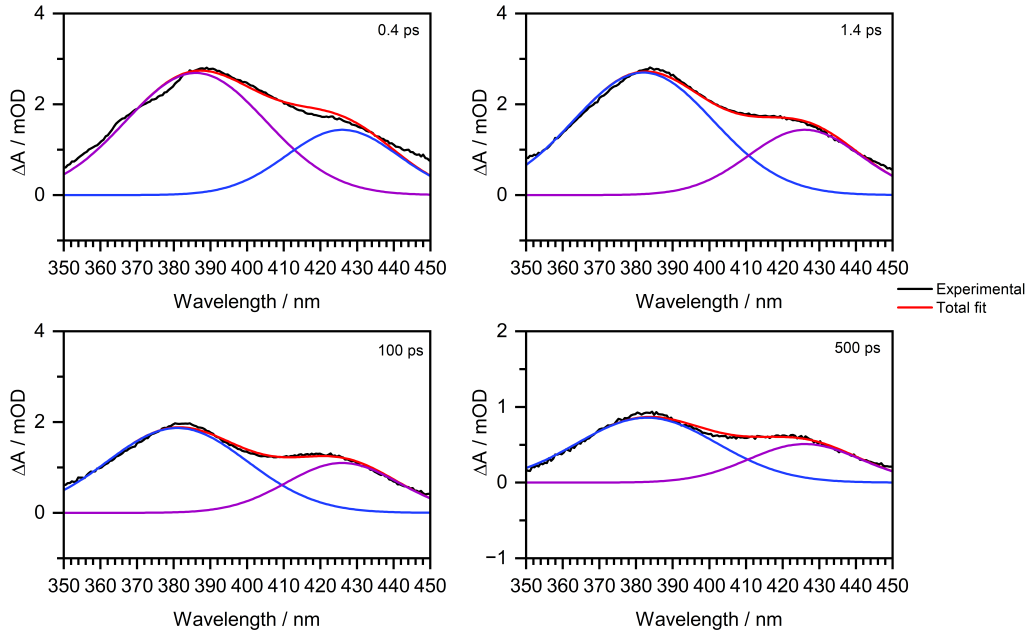

Figure 6.3.10: Spectral fitting of OL^- following photoexcitation at 476 nm from the KOALA software at four pump-probe delay times: 0.4 ps (top left), 1.4 ps (top right), 100 ps (bottom left), and 500 ps (bottom right). Experimental data is shown in black and total fit is in red. The features fitted are ESA 1 (blue) and ESA 2 (purple).

At very early times the longer wavelength fit (see Fig. 6.3.11) is not a good description of the data. The software is forcing ESA 3 to be negative, although it should be positive. This is only an issue sub-picosecond and the rest of the fit is good.

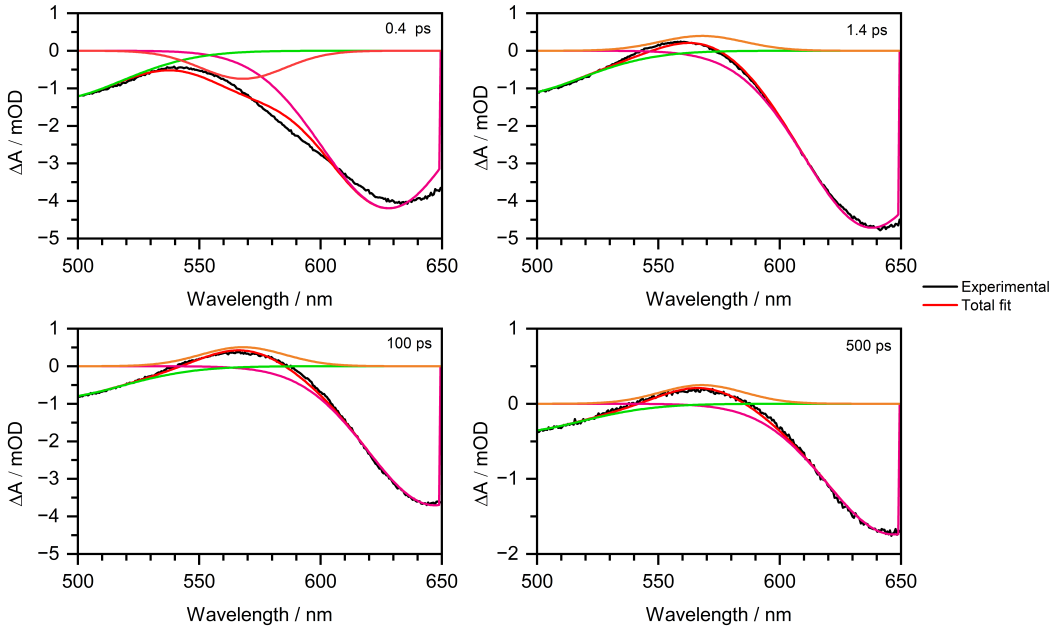

Figure 6.3.11: Spectral fitting of OL^- following photoexcitation at 476 nm, from the KOALA software at four pump-probe delay times: 0.4 ps (top left), 1.4 ps (top right), 100 ps (bottom left), and 500 ps (bottom right). Experimental data is shown in black and total fit is in red. The features fitted are GSB (green), ESA 3 (orange), and SE (pinK).

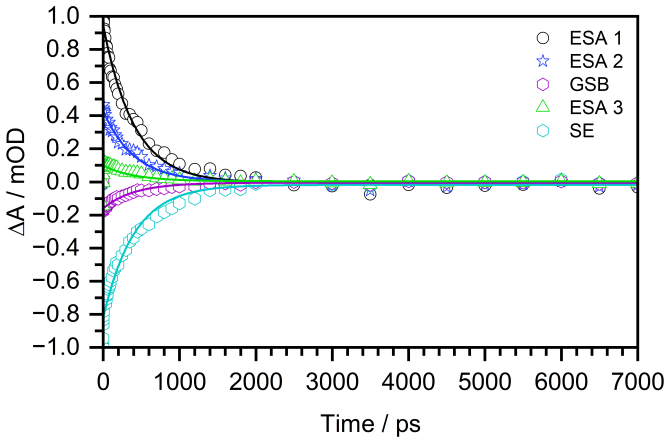

Figure 6.3.12: Kinetic traces of OL^- following photoexcitation at 476 nm, extracted for each feature in the TA spectrum. Kinetic traces were globally fit to an exponential function convoluted with the IRF of 0.11 ps (extracted from Surface Xplorer software, see Chapter 2). The lifetime of the exponential was found to be 400 $\pm$ 10 ps. The R^2 of the overall fit was 0.99.

Table 6.3.1 summarises the centre positions and FWHM of the Gaussian's used to fit to the 476 nm OL^- data. The position and width of each Gaussian was fixed

with the exception of the the width of the emission, as its centre position should not change.

Table 6.3.1: Summary of the center positions and FWHM of the Gaussian fits in the KOALA software, following photoexcitation of OL^- at 476 nm (Figure 6.3.10 and Figure 6.3.11). The FWHM value for SE is the starting value.

	centre / nm	FWHM / nm
ESA 1	381	45
ESA 2	426	36
GSB	488	71
ESA 3	568	41
SE	648	65

Table 6.3.2 summarises the amplitudes and residuals of the global fit displayed in Figure 6.3.12. The 400 ps timescale can be associated with the full recovery of the ground state as no other transient features remain/ grow in and all spectral features have decayed on the same timescale.

Table 6.3.2: Amplitudes and individual R^2 values for each component of the global fit to the data following 476 nm photoexcitation of OL^-, displayed in Figure 6.3.12.

	τ_1 / ps	R^2
ESA 1	400 ± 10	0.99
ESA 2	400 ± 10	0.99
GSB	400 ± 10	0.99
ESA 3	400 ± 10	0.84
SE	400 ± 10	0.98

349 nm Data

Again, as for the 476 nm data, initially kinetic traces of each feature were extracted by averaging over a 5 nm window and plotting the average amplitude over all pump-probe time delays. Figure 6.3.13 displays the extracted kinetics. The timescale extracted here is 640 ± 20 ps.

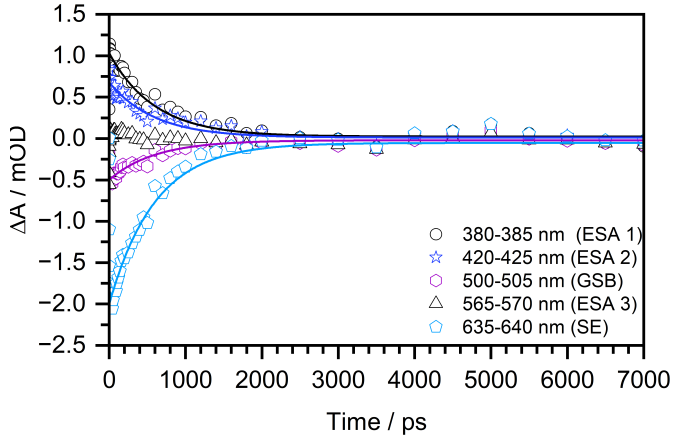

Figure 6.3.13: Kinetic traces of $^{-}$ following photoexcitation at 349 nm extracted for each feature in the TA spectrum. Kinetic traces were globally fit to an exponential function convoluted with the IRF of 0.24 ps (extracted from Surface Xplorer software, see Chapter 2). The lifetime of the exponential was found to be 640 $\pm$ 20 ps. The R^2 of the overall fit was 0.98.

Figure 6.3.14 displays four pump-probe time delays and at each the spectral fitting done in the KOALA software. As observed in the 476 nm data there are five spectral features, with the only difference being the second emission peak at 349 nm overlaps with the GSB. At early pump-probe delay times ESA 3 is negative although, it should be positive. This is only an issue sub-picosecond. At very long pump-probe time delays there is also some noise on the fit, especially ESA 3 where at some points its amplitude is negative again. This is due to the low (sub-mOD) signals at longer delay times.

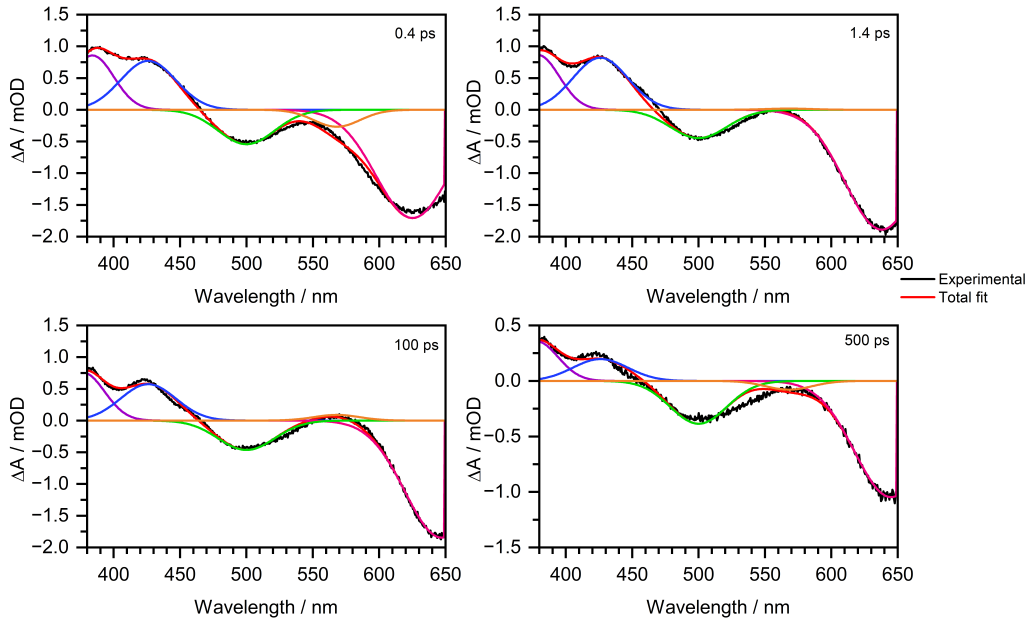

Figure 6.3.14: Spectral fitting of OL^- following photoexcitation at 349 nm from the KOALA software at four pump-probe delay times: 0.4 ps (top left), 1.4 ps (top right), 100 ps (bottom left), and 500 ps (bottom right). Experimental data is shown in black and total fit is in red. The features fitted are ESA 1 (blue), ESA 2 (purple), GSB/SE (green), ESA 3 (orange), and SE (pink).

Table 6.3.3 summarises the centre positions and FWHM of the Gaussian's used to fit to the 349 nm OL^- data. The position and width of each Gaussian was fixed with the exception of the width SE, as also done for the 476 nm. This is due to some early time red shifting. It is worth noting that these parameters are virtually identical to the parameters fit to the 476 nm data.

Table 6.3.3: Summary of the centre positions and FWHM of the Guassians fit in the KOALA software, following photoexcitation of OL^- at 349 nm (Figure 6.3.14).

	centre / nm	FWHM / nm
ESA 1	381	38
ESA 2	426	49
GSB/SE	500	50
ESA 3	568	41
SE	648	65

Figure 6.3.15 shows the kinetic traces extracted from the KOALA software for the

349 nm data. They are all globally fit to an exponential function convoluted with the IRF of 0.155 ps. The lifetime of the exponential was found to be 600 ± 20 ps. The R^2 of the overall fit was 0.99.

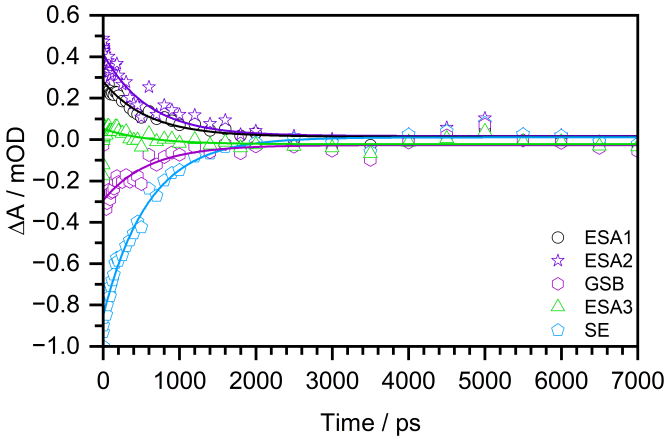

Figure 6.3.15: Kinetic traces of of OL^- following photoexcitation at 349 nm extracted for each feature in the TA spectrum. Kinetic traces were globally fit to an exponential function convoluted with the IRF of 0.24 ps. The lifetime of the exponential was found to be 600 ± 20 ps. The R^2 of the overall fit was 0.99.

Table 6.3.4 summarises the amplitudes and residuals of the global fit displayed in Figure 6.3.15. The 590 ps timescale can be associated with the full recovery of the ground state as no transient features other transient features remain/ grow in and all spectral features decay on the same timescale.

Table 6.3.4: Amplitudes and individual R^2 values for each component of the global fit following 349 nm photoexcitation of OL^-, displayed in Figure 6.3.15.

	τ_1 / ps	R^2
ESA 1	600 ± 20	0.97
ESA 2	600 ± 20	0.93
GSB/SE	600 ± 20	0.93
ESA 3	600± 20	0.19
SE	600 ± 20	0.99

The residual of the ESA 3 feature is low due to the previously discussed noise as it a very weak feature. Due to the GSB and SE feature overlapping it is not possible to distinguish the two features, but the monoexponential fits well to the data. It is possible the second SE feature could have decayed within the IRF or it is present

throughout the measurement. TCSPC measurements would be able to provide a more accurate representation of this.

6.3.4 Discussion of Oxyluciferin Results

First, we will examine and compare the early-time dynamics for both excitation wavelengths. Figure 6.3.16 shows the sub-picosecond dynamics following photoexcitation at 476 nm (left) and 349 nm (right).

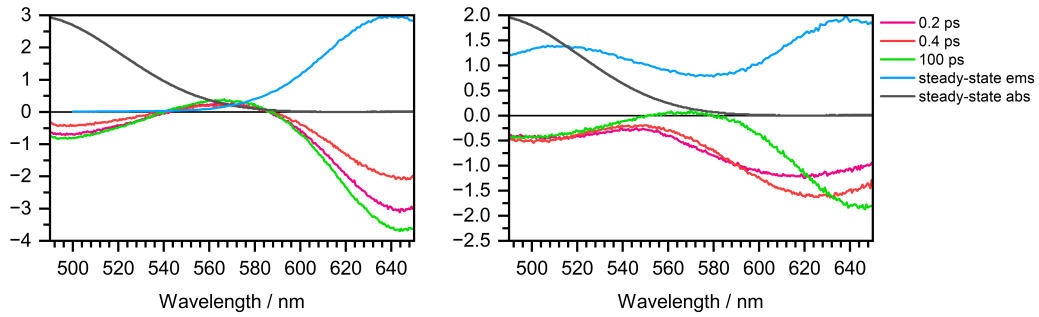

Figure 6.3.16: Sub-picosecond dynamics following photoexcitation at 476 nm (left) and 349 nm (right). 100 ps pump-probe delay time is also plotted for comparative purpose. Steady-state absorption and emission spectra are overlaid.

From the 349 nm (right) data, it is clear that the spectra at 0.2 ps and 0.4 ps closely match the steady-state emission spectrum following 349 nm excitation, whereas the spectrum at 100 ps resembles the emission data observed following 482 nm excitation. It should also be noted that ESA 3 (the S_1 signature) is absent in the sub-picosecond dynamics following 349 nm excitation. The 349 nm spectrum red-shifts, and the later time dynamics begin to resemble those observed with 476 nm excitation. This behavior is indicative of internal conversion back to the lower-lying electronic state within the first 1 ps. Figure 6.3.17 summarises the proposed mechanism.

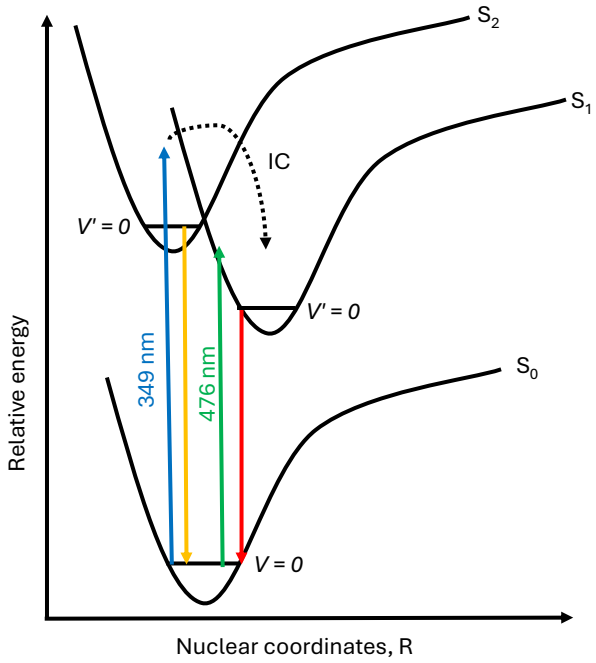

Figure 6.3.17: Schematic energy level diagram illustrating a summary of the proposed emission mechanism for OL^{-}.

Since it is evident that the early time dynamics of the 349 nm excitation involve contributions from the stimulated emission (SE) features of two different excited states, the Koala analysis was repeated to account for these contributions. This was conducted for a smaller probe wavelength range of just 465-650 nm as the additional SE features only have an impact in the longer wavelength region of the probe. The new Koala fits are displayed in Figure 6.3.18.

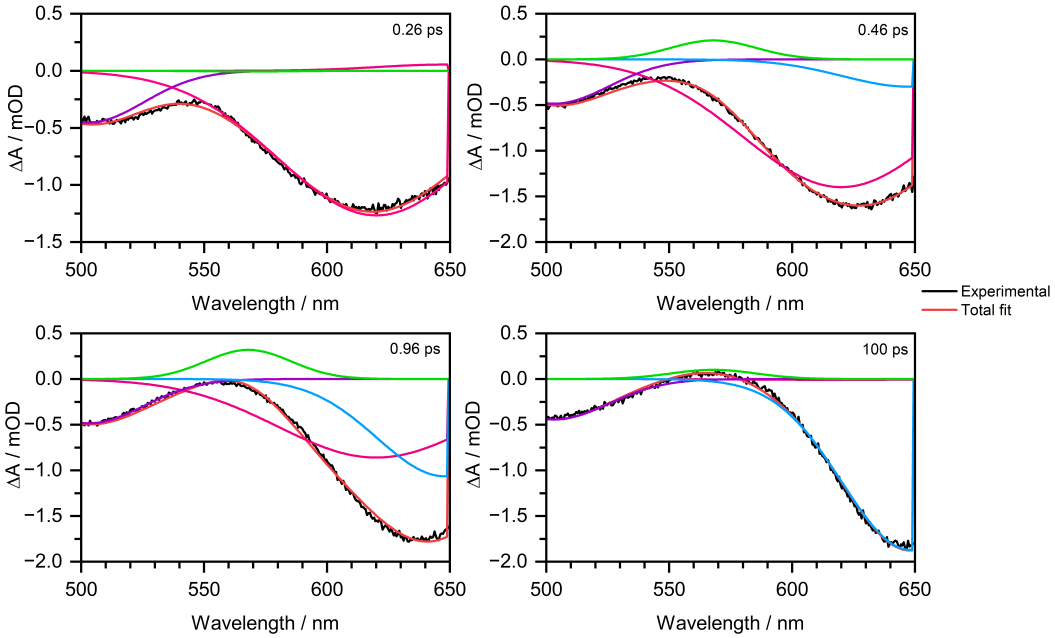

Figure 6.3.18: Spectral fitting of OL^- following photoexcitation at 349 nm from the KOALA software at four pump-probe delay times: 0.26 ps (top left), 0.46 ps (top right), 0.96 ps (bottom left), and 100 ps (bottom right). Experimental data is shown in black and total fit is in red. The features fitted are GSB/SE (S_2) (purple), SE (S_2) (pink), ESA 3 (green), and SE (S_1) (blue).

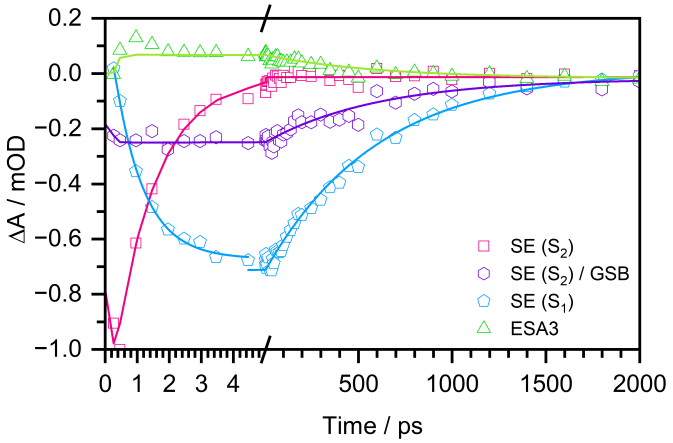

Figure 6.3.19: Kinetic fitting of OL^- following photoexcitation at 349 nm. Time constants are summarised in Table 6.3.5. All exponents are convoluted with the IRF of 0.24 ps.

The updated kinetic fitting, shown in Figure 6.3.19, demonstrates that contributions from both emissive states are present almost instantaneously. The higher energy emission (centred around 510 nm) overlaps with the position of the GSB thus sepa-

rating these features is not possible. Table 6.3.5 is a summary of the time constants extracted from the fitting.

Table 6.3.5: Amplitudes and individual R^2 values for each component of the global fit to the data following 349 nm photoexcitation of OL^-, as displayed in Figure 6.3.19. The decay time constants (τ_{decay}) were fixed during fitting to be the previously determined values, see Figure 6.3.15.

	τ_{grow} / ps	τ_{decay} / ps	R^2
SE (S_2)	-	1.3 ± 0.1	0.98
GSB/SE	-	600 ± 20	0.94
ESA 3	0.02 ± 0.04	600 ± 20	0.77
SE (S_1)	0.91 ± 0.1	600 ± 20	0.99

The new kinetic fitting supports the idea that there is ultrafast internal conversion back to the lower-lying electronic state within the first 1 ps, following photoexcitation at 349 nm (Figure 6.3.17). This would suggest Type II non-kasha photoluminescence behaviour (see Figure 6.3.6). Although, it was suggested previously this second emission was the result of a photoproduct [103] the TA spectrum does not show any evidence of this but we cannot completely rule out the possibility of this. The full recovery of the ground state occurs in a timescale of 600 ± 20. In contrast, following photoexcitation at 476 nm the full recovery of the ground state occurs faster on a timescale of 400 ± 10.

6.3.5 Transient Absorption Spectra of infraoxyluciferin

Figure 6.3.20 displays the two transient absorption spectra recorded after photoexcitation at 481 nm (near the first absorption maximum) and 551 nm (low energy edge of the first absorption maximum).

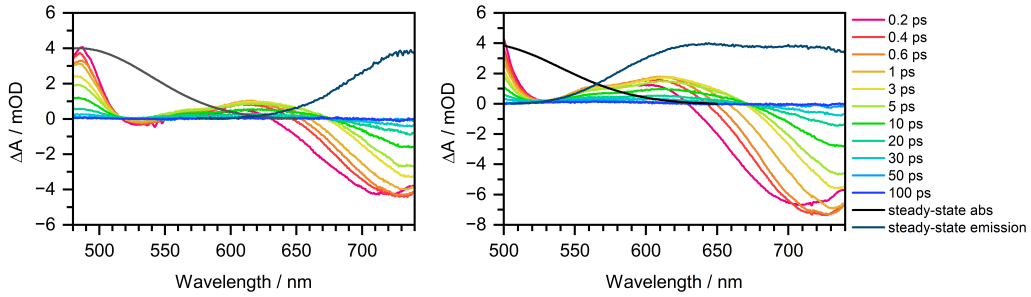

Figure 6.3.20: 870 μM TA spectra of iOL$^-$ at various pump-probe time delays displayed in the legend. **Left:** Spectrum after photoexcitation at 551 nm. Steady-state absorption (black) and relevant steady-state emission (blue) spectra are overlay. They are normalised to have a maximum mOD of 4. **Right:** Spectrum after photoexcitation at 481 nm. Steady-state absorption (black) and relevant steady-state emission (blue) spectra are overlaid. They are normalised to have a maximum mOD of 4.

The spectra at both pump wavelengths look remarkably similar and both have 4 different transient absorption spectral signatures. There are three ESA signatures on the redder edge of the spectrum centred at approximately 490 nm, 560 nm and 605 nm. There is one negative feature which is SE due to its location. There is a weak additional negative transient absorption signature in the 551 nm data. This is centred at 530 nm and its positions close to with the photoexcitation wavelength, suggesting it is a GSB. The negative GSB overlaps with the ESA and therefore is not observed over the entire absorption range.

551 nm Data Analysis

First, the kinetic traces of each feature were extracted by averaging over a 5 nm window and plotting the average amplitude over all pump-probe time delays. Figure 6.3.21 displays the extracted kinetics.

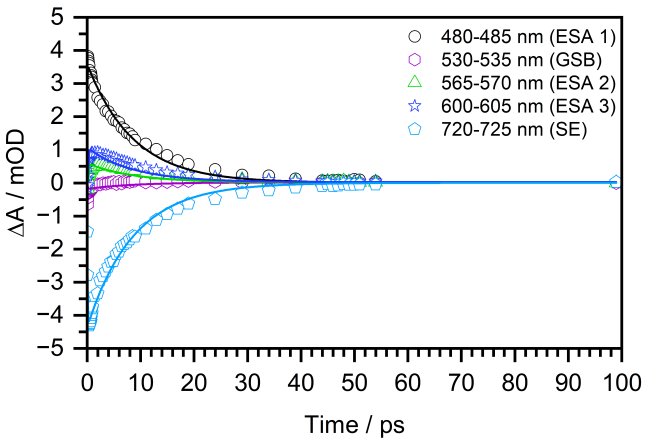

Figure 6.3.21: Kinetic traces of iOL^- following photoexcitation at 551 nm were extracted for each feature in the TA spectrum. Kinetic traces were globally fit to an exponential function convoluted with the IRF of 0.16 ps. The lifetime of the exponential was found to be 8.6 ± 0.2 ps. The R^2 of the overall fit was 0.99.

As a first approximation this is a reasonable way to look at the data. It is clear every spectral feature decays on the same timescale, suggesting that they all originate from the same electronic state. One thing to note is it is clear from Figure 6.3.20 that at very early pump-probe time delays the SE appears to spectrally narrow as ESA 3 grows in over its blue edge. There is an isobestic point at 675 nm arising from the superposition of ESA 3 and the SE. It should also be noted the negative feature near 530 nm is a GSB, due to its position matching well with the ground-state absorption spectrum. ESA 1 and ESA 2, clearly overlap with the rest of the GSB feature and therefore it can not be observed. The data was then analysed using the KOALA software, see Figure 6.3.22.

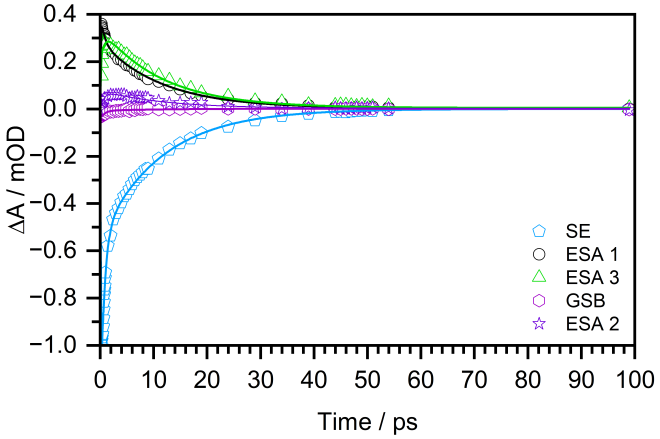

Figure 6.3.22: Kinetic traces of iOL^- following photoexcitation at 551 nm for were extracted by KOALA software for each feature in the TA spectrum. Kinetic traces were globally fit to a biexponential function convoluted with the IRF of 0.16 ps. The lifetimes of the biexponential were found to be 0.7 ± 0.02 ps and 11.4 ± 0.2 ps. The R^2 of the overall fit was 0.99.

Figure 6.3.23. shows the fitting carried out in the KOALA software at four pump-probe delay times.

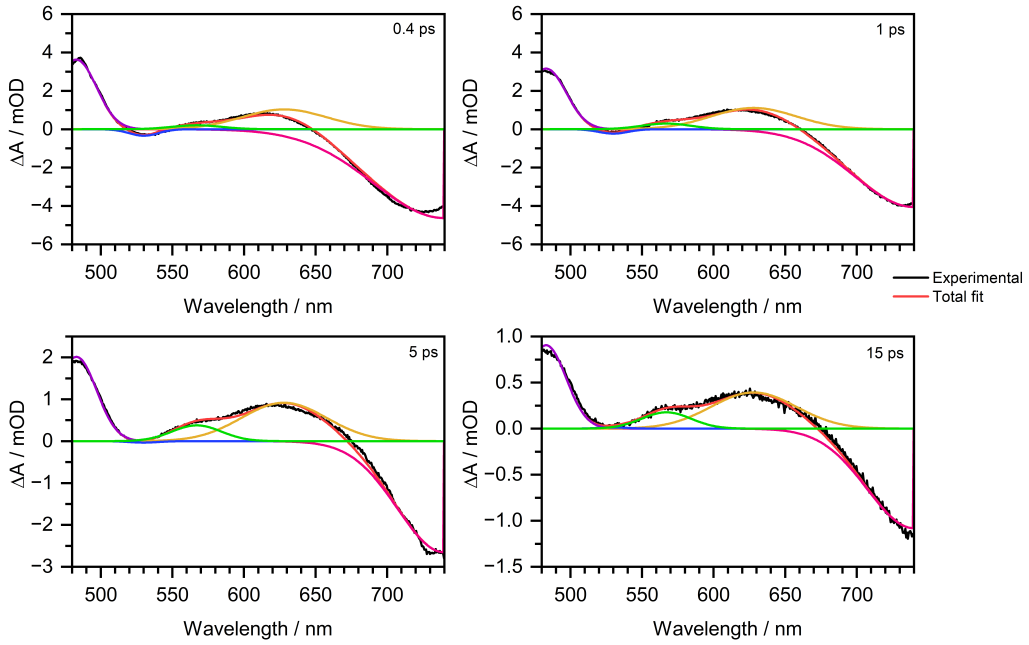

Figure 6.3.23: Spectral fitting of iOL^- following photoexcitation at 551 nm from the KOALA software at four pump-probe delay times: 0.4 ps (top left), 1 ps (top right), 5 ps (bottom left), and 15 ps (bottom right). Experimental data is shown in black and total fit is in red. The features fitted are ESA 1 (purple), GSB (blue), ESA 2 (green), ESA 3 (orange), and SE (pink).

Table 6.3.6 summarises the central positions and FWHM of the Gaussians fit in the KOALA software. All Gaussians widths and centres are fixed in the fitting procedure, apart from the width of the SE is floated. Only the width is floated as the emission maxima should not change. This is to account for at early pump-probe delay times the spectral band is narrowing, although this is is likely due to ESA 3 growing in over the top.

Table 6.3.6: Summary of the centre positions and FWHM of the Gaussian's fit in the KOALA software of iOL^- following photoexcitation at 551 nm, shown in Figure 6.3.23. The FWHM of SE is the starting position.

	centre / nm	FWHM / nm
ESA 1	483	33
GSB	530	24
ESA 2	567	41
ESA 3	628	70
SE	740	97

Table 6.3.7 summaries the amplitudes and residuals of the global fit displayed in Figure 6.3.22. A biexponential was fit rather than a monoexponential due to an increase in the R^2 of each feature and the overall value. The timescales will be discussed in the following section.

Table 6.3.7: Amplitudes and individual R^2 values for each component of the global fit of iOL^- following photoexcitation at 551 nm, displayed in Figure 6.3.22.

	A_1	τ_1 / ps	A_2	τ_2 / ps	R^2
ESA 1	0.26	0.7 ± 0.02	0.74	11.4 ± 0.2	0.95
GSB	-0.80	0.7 ± 0.02	0.2	11.4 ± 0.2	0.95
ESA 2	-0.49	0.7 ± 0.02	0.51	11.4 ± 0.2	0.98
ESA 3	-0.29	0.7 ± 0.02	0.71	11.4 ± 0.2	0.99
SE	-0.56	0.7 ± 0.02	-0.44	11.4 ± 0.2	0.99

481 nm Data Analysis

Again, the kinetic traces of each feature were first extracted by averaging over 5 nm windows and plotting the average amplitude over all pump-probe time delays. Figure 6.3.24 displays the extracted kinetics.

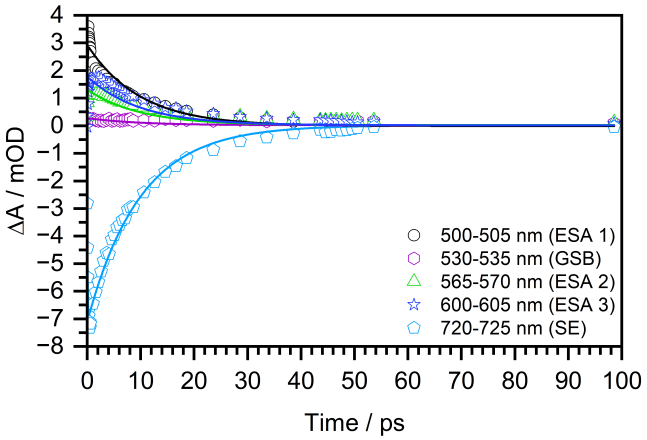

Figure 6.3.24: Kinetic traces extracted for each feature in the TA spectrum of iOL^- following photoexcitation at 481 nm. Kinetic traces were globally fit to an exponential function convoluted with the IRF of 0.24 ps. The lifetime of the exponential was found to be 8.9 ± 0.2 ps. The R^2 of the overall fit was 0.98.

As with the 551 nm analysis this is a reasonable way to initially look at the data. Again, it is clear every spectral feature decays with the same lifetime and would suggest everything involves the same electronic state. Figure 6.3.25 displays the globally fitted kinetics extracted from the KOALA software.

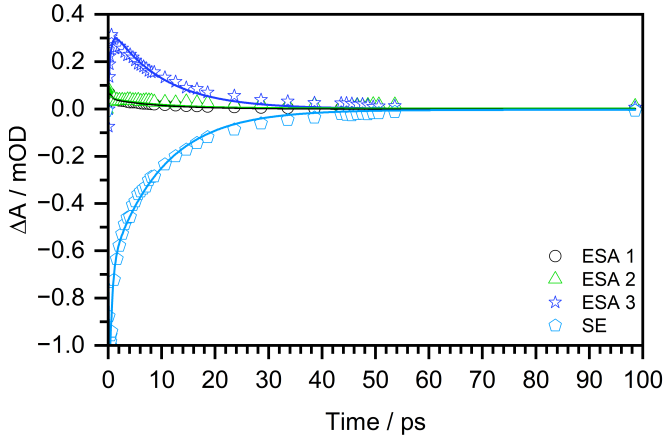

Figure 6.3.25: Kinetic traces extracted by KOALA software for each feature in the TA spectrum of iOL^- following photoexcitation at 481 nm. Kinetic traces were globally fit to an biexponential function convoluted with the IRF of 0.24 ps. The lifetimes of the biexponential were found to be 0.5 ± 0.04 ps and 9.8 ± 0.3 ps. The R^2 of the overall fit was 0.99.

Table 6.3.8 summaries the central positions and FWHM of the Gaussians fit in the KOALA software. All Gaussians widths and centres are fixed in the fitting procedure, apart from the width of the SE. This is to account for the narrowing of the SE band within the first picosecond, possibly due to ESA 3 growing in. The widths and positions are the same used to fit the 551 nm, see Table 6.3.6. There was no evidence of the GSB feature here, although it is likely hidden under the ESA. It was attempted to use the steady-state absorption spectrum as a basis function to account for the contribution in the fit, although the software does not provide a way of fixing the amplitude to be negative so the fit was poor. The fit used is reasonable as we observe the full recovery of the ground state, and hence know the GSB recovery timescales is more than likely the same timescale as every other process.

The steady-state emission spectra at a photoexcitation wavelength of 488 nm, see Figure 6.3.4, reveals an additional peak on the blue energy edge. The steady-state emission was used as a basis function and fit to the data, although this was not a good representation of the data. Due to the dependence of the emission on excitation energy it is plausible the blue-edge emission peak is emission for a higher lying electronic state. From the emission spectra we can see this blue-edge

is most prominent at 410 nm and therefore, at 488 nm the population lies low in the vibrational energy levels of the higher lying electronic state. This could suggest a possible reason why the second emission is not observed in the TA spectrum, if the lifetime is quicker than the IRF. This could be confirmed by conducting TC-SPC measurements and the TA spectrum at the higher photoexcitation energy. Due to sample limitations, this was not feasible for this thesis. There will be further discussion of this in the following section.

Figure 6.3.26 displays the fits to the experimental data of iOL^- following photoexcitation at 481 nm at four selected pump-probe delay times.

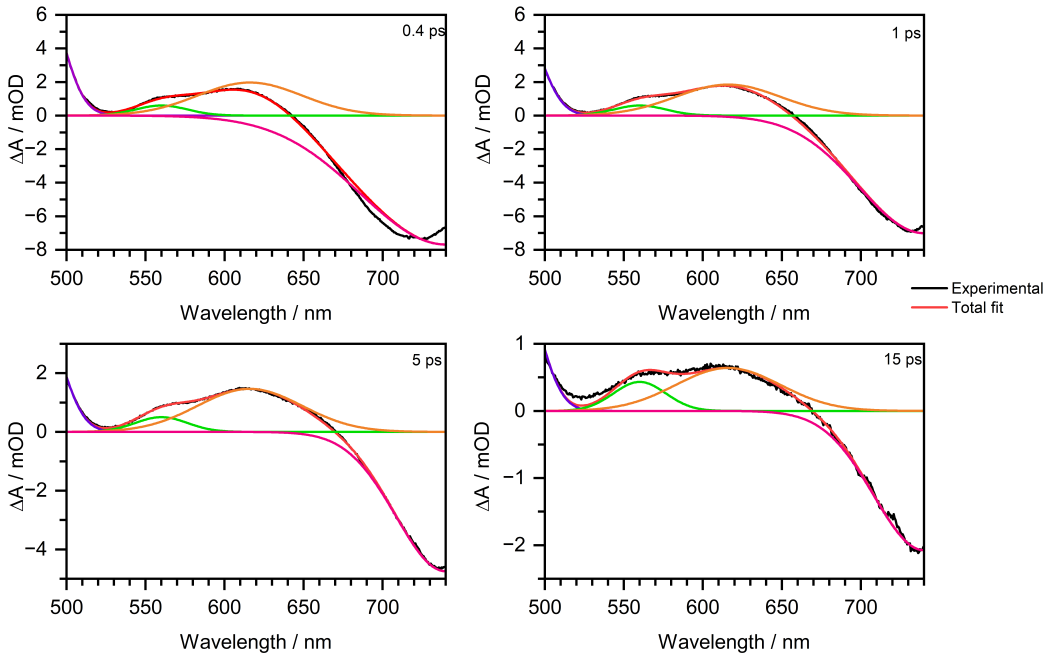

Figure 6.3.26: Spectral fitting from the KOALA software of iOL^- following photoexcitation at 481 nm at four pump-probe delay times: 0.4 ps (top left), 1 ps (top right), 5 ps (bottom left), and 15 ps (bottom right). Experimental data is shown in black and total fit is in red. The feature fitted are ESA 1 (purple), ESA 2 (green), ESA 3 (orange), and SE (pink).

Table 6.3.9 summarises the amplitudes and residuals of the global fit displayed in Figure 6.3.25. A biexponential was fit over a monoexponential due to an increase in the R^2 of each feature and the overall value. The timescales will be discussed in the following section.

Table 6.3.8: Summary of the centre positions and FWHM of the Gaussian's fit in the KOALA software of iOL^- following photoexcitation at 481 nm, shown in Figure 6.3.23. The FWHM of the SE is the starting position.

	centre / nm	FWHM / nm
ESA 1	483	33
ESA 2	567	41
ESA 3	616	78
SE	740	97

Table 6.3.9: Amplitudes and individual R^2 values for each component of the global fit of iOL^- following photoexcitation at 481 nm, displayed in Figure 6.3.22.

	A_1	τ_1 / ps	A_2	τ_2 / ps	R^2
ESA 1	0.49	0.5 ± 0.04	0.51	9.8 ± 0.3	0.99
ESA 2	0.31	0.5 ± 0.04	0.69	9.8 ± 0.3	0.77
ESA 3	-0.42	0.5 ± 0.04	0.58	9.8 ± 0.3	0.93
SE	-0.52	0.5 ± 0.04	-0.56	9.8 ± 0.3	0.99

6.3.6 Discussion of Infraoxyluciferin Results

Similar to the approach taken with the oxyluciferin data, we will first analyse the sub-picosecond spectral features. Figure 6.3.27 displays a comparison of both data sets at 0.2 ps and 10 ps. Following photoexcitation at 481 nm the spectrum at 0.2 ps differs slightly from the 551 nm spectrum. The shapes and relative amplitudes of ESA 2 (565 nm) and ESA 3 (625 nm) differ and there is no evidence of the GSB (535 nm). The SE emission of the 481 nm data is slightly broader compared to that in the 551 nm data. These slight differences could potentially be explained by the presence of the second emission peak observed in the steady-state emission spectrum (see Figure 6.3.4) following photoexcitation at 481 nm at very early pump-probe delay times. The additional negative SE feature may reduce the amplitude of ESA 3 relative to ESA 2, leading to a broader SE emission feature. Although this is a possibility there is only this minimal evidence to suggest this and this would benefit from repeating the TA experiments with smaller time steps at early pump-probe

delay times. TCSPC experiments monitoring both emissions following excitation at 481 nm would also give a further insights into the dynamics.

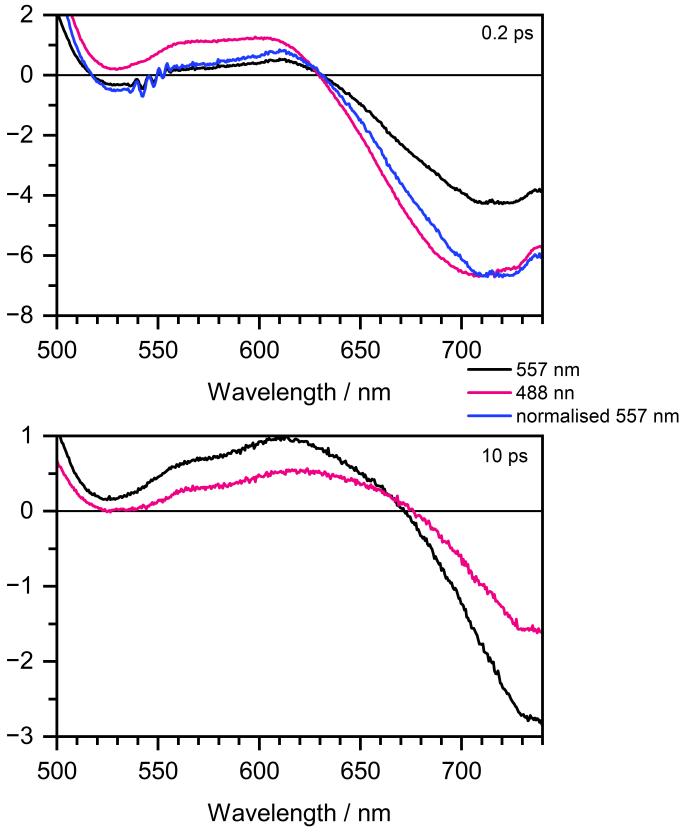

Figure 6.3.27: Top: Spectral slices at a pump-probe delay of 0.2 ps of infraoxyluciferin following photoexcitation at 551 nm (black) and 481 nm (pink) is shown. The blue trace represents the 551 nm spectrum, normalised to the maximum of the 481 nm spectrum. **Bottom:** Spectral slices at a pump-probe delay of 10 ps of infraoxyluciferin following photoexcitation at 551 nm (black) and 481 nm (pink) is shown.

Figure 6.3.28 illustrates the proposed mechanism for the photoluminescence behaviour observed in iOL^-. First, we will discuss the steady-state emission data following 488 nm excitation. Two emission peaks of equal intensity are observed: the first is centered at approximately 720 nm, and the second at approximately 640 nm. This could indicate that the energy provided by the 488 nm excitation is sufficient to photoexcite both electronic states, though likely only to fairly low-lying vibrational levels in the higher-lying electronic state. Internal conversion to the lower electronic

state occurs, leading to nearly equal contributions from both states in the observed emission spectrum. Following photoexcitation at 410 nm, the emission spectrum still displays two peaks, but the higher-energy emission is significantly more intense. The excitation scans indicate that the maximum fluorescence intensity for both emission peaks would occur around 400 nm.

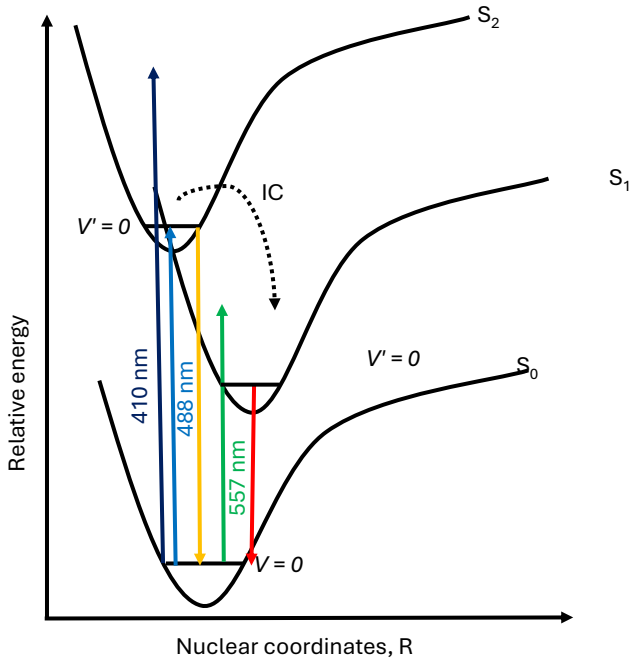

Figure 6.3.28: Schematic energy level diagram of the proposed mechanism for the photoluminescence behaviour observed in iOL^-.

Following photoexcitation at 551 nm, two timescales are observed: 0.7 ± 0.02 ps and 11.4 ± 0.2 ps. Similarly, after photoexcitation at 488 nm, two timescales are observed: $0.5pm0.04$ ps and 9.8 ± 0.3 ps. It is unclear why biexponential behavior is observed, particularly for the lower energy 551 nm photoexcitation, where only one emission feature is present. The longer timescales of 11.4 ± 0.2 ps and 9.8 ± 0.3 ps can be attributed to the full recovery of the ground state.

6.3.7 Calculations

In order to assist with the interpretation of our experimental observations, complementary gas-phase calculations of OL^- and iOL^- have been conducted by Olivia Bennett from Prof. Graham Worth's group at UCL. Calculations are performed

using ADC(2)/aug-cc-pVDZ functional.

Table 6.3.10: ADC(2)/aug-cc-pVDZ calculated VEEs of OL^-. Oscillator strengths are in brackets next to the energies.

S_1 / eV	S_2 / eV	S_3 / eV	S_4 / eV
2.20 A' (0.79)	2.65 A'' (0.00)	3.49 A'' (0.00)	3.67 (0.18) A'

Table 6.3.11: ADC(2)/aug-cc-pVDZ calculated VEEs of iOL^-. Oscillator strengths are in brackets next to the energies.

S_1 / eV	S_2 / eV	S_3 / eV
1.90 A' (1.17)	2.47 A'' (0.00)	3.38 A' (0.20)

For OL^- (see table 6.3.10) both transitions with oscillator strength (S_1 and S_4) are $\pi\pi^*$ transitions. The same can be said for iOL^- (see table 6.3.11). Figure 6.3.29 displays a scaled energy level diagram summarising the results in tables 6.3.10 and 6.3.11.

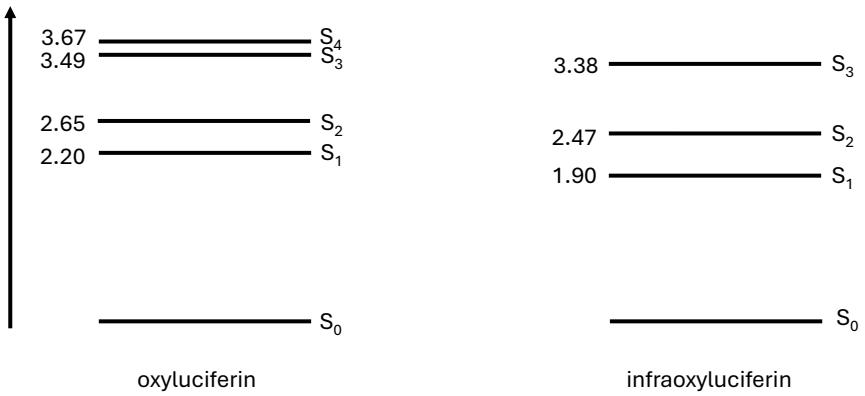

Figure 6.3.29: Scaled energy level diagram summarising the results from tables 6.3.10 and 6.3.11.

6.3.8 Comparison of Infraoxyluciferin and Oxyluciferin Results

Table 6.3.12: Summary of timescales for both iOL^- and OL^- from the global fitting of the KOALA extracted kinetics.

	τ_1 / ps	τ_2 / ps
iOL^- (488 nm)	0.7 ± 0.02	9.8 ± 0.3
iOL^- (551 nm)	0.5 ± 0.04	11.4 ± 0.2
OL^- (349 nm)	0.9 ± 0.1	600 ± 20
OL^- (476 nm)	-	400 ± 10

The best data to compare of iOL^- and OL^- is following photoexcitation with the lowest photon energy: 551 nm and 476 nm respectively. At these photon energies, there is only one emission feature contributing to the signal, therefore making it possible to compare. From the TAS measurements it was found that iOL^- recovers its ground state over 70 times faster than OL^-. The faster ground state recovery observed in iOL^- would indicate there is faster internal conversion back to ground state from the first electronic excited state this would also provide a plausible ex-

plain as to why the fluorescence quantum yield is lower. Although, comparing the gas-phase calculations of OL^- the first bright state is at 2.2 eV, while for iOL^- is at 1.9 eV. If we consider the steady-state absorption spectra (see Figure 6.3.1) for iOL^- the absorption maximum is only red-shifted from that of OL^- by less than 10 nm, although the iOL^- first absorption band is around 50 nm broader. This could indicate that the lowest-lying electronic states of both molecules do not differ significantly in energy. This observation aligns with gas-phase calculations; however, further calculations that include the aqueous environment and dynamics would be required for a more comprehensive understanding. It is plausible the fast sub-picosecond timescale observed for iOL^- could be the S_1/S_0 IC. Although, the amplitudes of the fast timescale extracted for the fit for ESA 2, ESA 3, and GSB have the opposite magnitude. There are also no corresponding timescales extracted for OL^- following photoexcitation of the 476 nm state, so it's not possible to say whether the S1/S0 internal conversion is faster in iOL^-. In summary, there are no definitive conclusions to explain why OL^- is a more efficient emitter than iOL^-. Although, the efficiency of the internal conversion could be a factor, and the much faster recovery of the ground state in iOL^- could support this. Both molecules exhibit unusual steady-state emission properties that are dependent on the excitation energy. Upon excitation with 349 nm OL^- has a second emission peak observed at higher photon energies. There is evidence of this in the very early pump-probe delay times of the TAS spectra. This emission has been previously assigned to the dianionic species [103] due to isomerisation and hydrolysis. The dianionic species has an emission maximum at 539 nm and the species observed has a emission maximum at approximately 510 nm. Therefore, it is hard to be certain that this is definitely the dianionic species. iOL^- brightest emission peak is present upon photoexcitation at higher photon energies and is blue-shifted from the emission peak that is present upon excitation with lower photon energies. The brightest emission-peak has a tail on the red-edge of the spectrum. A possible reason for the emission properties here could be competing IC between the two emissive states. Although, if the the second emitting species in OL^- is a photoproduct, then it is likely that it is also the case for

iOL^-. TCSPC experiments of each molecule at all excitation wavelengths should be conducted to attempt to understand the dual emissions of each molecule.

6.4 Conclusions

To conclude, this Chapter presented a comparison of the dynamics of OL^- and iOL^- in aqueous solution. This is the first study of the relaxation dynamics of iOL^- and aimed at understanding why iOL^- emission is less efficient than OL^-. This work is motivated by the need for new nIR emitters for use as bioluminescent probes to improve *in vivo* tissue penetration. The TAS measurements revealed OL^-, following photoexcitation at 476 nm, recovered the ground state in 400 ps. In contrast, iOL^-, following photoexcitation at 551 nm, recovered the ground state much faster with timescales of 0.5 ± 0.04 ps and 11.4 ± 0.2 ps. It was suggested the sub-picosecond timescale could be the S_1/S_0 IC and that this could be a faster process in iOL^- in comparison to OL^-. Although, there is a lack of definitive evidence to fully support this argument but it would explain why iOL^- is a less efficient emitter. There are comparable calculations for both molecules in the gas-phase and they showed the first bright state in OL^- is at 2.2 eV, while for iOL^- is at 1.9 eV. This is in line with the observation from the steady-state absorption spectra that the absorption maxima of each molecule are not significantly red-shifted. Further computational work of both molecules in aqueous solution would be required to search for any conical intersections and location on the potential energy surfaces. This would aid the observations from the transient absorption experiments and help confirm why the ground state is recovered quicker in iOL^-. The calculations also revealed that, the two bright states have a similar relative energy gap in iOL^- and in OL^-. Although, this could change in an aqueous environment. The steady-state emission properties of both molecules are also interesting. OL^-, upon photoexcitation with higher photon energies, exhibits a second emission feature that was previously attributed to the dianionic species formed *via* isomerisation and hydrolysis. Although this is plausible, it seems unlikely with the cyclopropyl group present, but we cannot rule it out. The second emission was observed at

very early pump-probe delay times in the TAS spectra, and its decay was found to have a time constant of 1.3± 0.1 ps. iOL^-'s most prominent emission feature was found to have a maximum around 600 nm, observed following photoexcitation at 410 nm. The most red-shifted emission was observed following photoexcitation at lower photon energies (551 nm) and was centered at 740 nm. Photoexcitation at photon energies between these values reveals an emission spectrum with both peaks present. One explanation for the emission properties here could be competing IC between the two coupled emissive states. Although, if the second emitting species in OL^- is a photoproduct, it is likely that this is also the case for iOL^-. TCSPC experiments of each molecule at all excitation wavelengths should be conducted to attempt to understand the dual emissions of each molecule. To determine if a photoproduct is present, the sample could be photoexcited, followed by recording an NMR spectrum to analyse and confirm the structure.

Chapter 7

Conclusions and Outlook

This thesis presents the results of the excited-state dynamics of four biologically relevant systems using time-resolved spectroscopy in aqueous solution. The studied systems include phenolate, methyl-group substituted phenolates, oxyluciferin, and infra-oxyluciferin. Phenolate serves as a building block for various biologically significant molecules, such as the green fluorescent protein, the photoactive yellow protein, and oxyluciferin. Oxyluciferin is the chemiluminescent product responsible for the emission in fireflies. The work presented employs two complementary experimental techniques: transient absorption spectroscopy (TAS) and liquid microjet time-resolved photoelectron spectroscopy (LJ-TRPES). TAS provides information about changes in absorption signatures, while LJ-TRPES measures electron binding energy both as a function of pump-probe delay time.

7.1 Transient Absorption Spectroscopy Studies of Aqueous Phenolate

Chapter 3 presents a study of the photooxidation mechanism in aqueous phenolate [80]. After photoexcitation with UV light phenolate in aqueous solutions forms a solvated electron and leaves behind the neutral radical. This study aimed to understand the implication of excitation wavelength on the photooxidation mechanism due to some existing controversy in the literature [78, 79]. Two mechanisms had previously been proposed from femtosecond TAS studies. The first, by Chen *et al.*, identified the formation of the solvated electron on two timescales: a fast

component from vibrationally hot S_1 and a slower component matching the fluorescence lifetime from vibrationally cold S_1 after photoexcitation at 266 nm. The second, by Tyson *et al.*, found after photoexcitation at 257 nm the electron was only formed on the fast timescales said to be from vibrationally hot S_1 and this out competed formation from vibrationally cold S_1 due to the higher photon energy. They suggested an inverse Marcus theory picture were the electron was formed *via* a tunneling mechanism and due to the higher photon energy they were closer/above the barrier. Due to the higher photon energy, we questioned why higher-lying electronic states, such as S_{1n} and S_2, had not been considered in the mechanism of photooxidation. This prompted us to undertake a systematic study using a range of excitation wavelengths to explore the impact of photon energy on the photooxidation mechanism. By combining femtosecond TAS with high-level quantum chemistry calculations carried out by Anton Boichenko under the supervision of Anastastia Bochenkova (Moscow State University) and LJ-PES measurements performed by William Fortune, we investigated the wavelength-dependent mechanism of phenolate photooxidation. We found that upon photoexcitation of S_1 that our observations were consistent with Chen *et al.* and the electron was formed on two timescales from vibrationally hot and cold S_1 and the corresponding neutral radical was formed in the D_0 state. After photoexcitation of S_2 we observed only one faster timescale for electron formation and the timescales for geminate recombination were also observed to be faster. Due to an additional ESA feature in the TAS spectrum and the faster electron recombination timescales we propose after photoexcitation of S_2 the electron is ejected into the continuum of the radical/electron contact pair, where the radical is in a higher lying electronic state. This conclusion was also supported by the LJ-PES experiments and quantum chemistry calculations.

Following this, Chapter 4 presented a systematic study of 2-, 3-, and 4-methylphenolate (2MP, 3MP, and 4MP) in aqueous solution using TAS. This study aimed to investigate the impact of methyl-group substitution at different positions on the aromatic ring and compares the findings to those of phenolate (P). This study

combined TAS experiments with time-correlated single photon counting (TCSPC) by Shivalee Dey under the supervision of Stephen Bradforth (University of Southern California), and high-level quantum chemistry calculations carried out by Anton Boichenko under the supervision of Anastastia Bochenkova (Moscow State University). It was found that the timescale for electron formation for 2MP and 4MP was faster due to the lower VDE of these molecules in comparison to 3MP and P. The electron recombination timescales was found to have a dependency of the methyl-groups position relative to the O^- atom, the closer the methyl-group is the faster the observed recombination is. We proposed this could be caused by the localised solvation environment. The calculations showed that 2MP in comparison to the other molecules made the least hydrogen bonds with the O^- atom. Although we can speculate that the hydrogen bonding network may trap the electron more effectively when the methyl group is closer to the O^- atom, further work is needed to substantiate this hypothesis. We propose that further calculations, such as electron transport simulations, could help trace the trajectory of the electron after its formation.

7.2 Time-Resolved Photoelectron Spectroscopy Studies of Aqueous Phenolate

Chapter 5 presented preliminary liquid microjet time-resolved photoelectron spectroscopy LJ-TRPES) data for aqueous phenolate. This dataset is the first time-resolved data recorded on a liquid microjet spectrometer within the Fielding group and serves as proof of principle that these time-resolved experiments can now be successfully conducted at UCL. Phenolate was chosen in order to compare the LJ-TRPES experiments with TAS experiments and see if the different methods reveal different dynamics due to phenolates propensity to sit on the surface of a solution. Phenolate was studied following $1+1$ resonance enhance detachment with a pump wavelength of 287 nm which is resonant with the absorption maxima of S_1 state and a probe wavelength of 267 nm. The photoelectron spectrum was observed to have two components and they were assigned to be $1^1\pi\pi^*$-D_0 detachment and the

solvated electron. It is not possible to comment on what these features do as a function of pump-probe delay time with great confidence due to a lack of data. We also observed the biexponential decay of the total photoelectron signal and the time constants were found to be 0.2±0.03 ps and 33±6 ps. These are faster than the equivalent timescales observed in our TAS experiments and could potentially indicate that the dynamics are different due to phenolate being more on the surface than in the bulk solution. In order to have a full picture of the dynamics more data would have to be recorded to understand how the electron binding energy (eBE) changes with pump-probe delay time. In order to prove the higher eBE signal is the solvated electron we propose to use the electron scavenger potassium nitrate. Although more experimental data has to be recorded the two spectral features were still able to be identified and the eBEs are consistent with literature.

7.3 Transient Absorption Spectroscopy Studies of Bioluminescent Emitters

Chapter 6 explores two derivatives of oxyluciferin, the luminescent emitter in fireflies. The first is the phenolate-keto form of oxyluciferin, referred to as OL^-, and the second is the phenolate-keto form of infra-oxyluciferin, referred to as iOL^-. Although iOL^- has a red-shifted emission maxima in comparison to OL^- they have remarkably similar steady-state absorption spectra. The Chapter aimed to understand why iOL^- is a much less efficient emitter than OL^- by studying the excited state dynamics with TAS. The motivation behind this was from this new understanding be able to help aid the rational design of new bioluminescent probes with emission maxima further in the near-infrared. These would have applications in bioluminescence imaging and could improve tissue penetration. This is the first study of the excited-state dynamics of iOL^-. OL^- in aqueous pH 11 buffer solution following photoexcitation at 476 nm, was found to have a emission lifetime and complete recovery to its ground state in approximately 400 ps. Whereas, for iOL^- following photoexcitation at 557 nm, this process was significantly faster, occurring in around 10 ps. There was also a second sub-picosecond component

associated with the ground-state recovery. The more rapid internal conversion in iOL^- provides a possible explanation as to why the quantum yield of the emission is much lower. Although, there was a lack of sufficient evidence that this was actually the case. Both molecules as exhibit the very fascinating phenomenon of dual fluorescence and the emission properties of both have wavelength dependencies. It was previously suggested that the second emission peak in oxyluciferin could be a dianionic product. We proposed an alternative explanation, suggesting the presence of two emissive states. However, more evidence is needed to confirm either assignment. This work would benefit from further quantum chemistry calculations to search for a conical intersection on the potential energy surface. Further experimental work could also be done to fully understand the emission properties of both molecules and we propose wavelength resolved TCSPC in order to fully understand the wavelength dependence of the dual emissions.

Bibliography

(1) Roberts, G. M.; Stavros, V. G. *Chemical Science* **2014**, *5*, 1698–1722.

(2) Kukura, P.; McCamant, D. W.; Yoon, S.; Wandschneider, D. B.; Mathies, R. A. *Science* **2005**, *310*, 1006–1009.

(3) Polli, D.; Altoè, P.; Weingart, O.; Spillane, K. M.; Manzoni, C.; Brida, D.; Tomasello, G.; Orlandi, G.; Kukura, P.; Mathies, R. A., et al. *Nature* **2010**, *467*, 440–443.

(4) Lee, H.; Cheng, Y.-C.; Fleming, G. R. *Science* **2007**, *316*, 1462–1465.

(5) Cisneros, C.; Thompson, T.; Baluyot, N.; Smith, A. C.; Tapavicza, E. *Physical Chemistry Chemical Physics* **2017**, *19*, 5763–5777.

(6) Mooney, C. R.; Parkes, M. A.; Iskra, A.; Fielding, H. H. *Angewandte Chemie* **2015**, *127*, 5738–5741.

(7) Parkes, M. A.; Phillips, C.; Porter, M. J.; Fielding, H. H. *Physical Chemistry Chemical Physics* **2016**, *18*, 10329–10336.

(8) Amouyal, E.; Bernas, A.; Grand, D.; Mialocq, J.-C. *Faraday Discussions of the Chemical Society* **1982**, *74*, 147–159.

(9) Snellenburg, J. J.; Laptenok, S. P.; DeSa, R. J.; Naumov, P.; Solntsev, K. M. *Journal of the American Chemical Society* **2016**, *138*, 16252–16258.

(10) Henley, A.; Patel, A. M.; Parkes, M. A.; Anderson, J. C.; Fielding, H. H. *The Journal of Physical Chemistry A* **2018**, *122*, 8222–8228.

(11) Mooney, C. R.; Parkes, M. A.; Zhang, L.; Hailes, H. C.; Simperler, A.; Bearpark, M. J.; Fielding, H. H. *The Journal of Chemical Physics* **2014**, *140*.

(12) Mooney, C. R.; Horke, D. A.; Chatterley, A. S.; Simperler, A.; Fielding, H. H.; Verlet, J. R. *Chemical science* **2013**, *4*, 921–927.

(13) Naumov, P.; Ozawa, Y.; Ohkubo, K.; Fukuzumi, S. *Journal of the American Chemical Society* **2009**, *131*, 11590–11605.

(14) Endicott, J. F. Photochemical pathways, 1983.

(15) Combes, J.; Duclos, P.; Seiler, R. Rigorous atomic and molecular physics, 1981.

(16) Butler, L. J. *Annual review of physical chemistry* **1998**, *49*, 125–171.

(17) Venkatraman, R. K.; Orr-Ewing, A. J. *Accounts of Chemical Research* **2021**, *54*, 4383–4394.

(18) Ravi Kumar, V.; Verma, C.; Umapathy, S. *The Journal of Chemical Physics* **2016**, *144*.

(19) Liptay, W. *Angewandte Chemie International Edition in English* **1969**, *8*, 177–188.

(20) Ben-Amotz, D. *Journal of the American Chemical Society* **2019**, *141*, 10569–10580.

(21) Maroncelli, M.; MacInnis, J.; Fleming, G. R. *Science* **1989**, *243*, 1674–1681.

(22) Ghosh, D.; Roy, A.; Seidel, R.; Winter, B.; Bradforth, S.; Krylov, A. I. *The Journal of Physical Chemistry B* **2012**, *116*, 7269–7280.

(23) Woodhouse, J. L.; Henley, A.; Parkes, M. A.; Fielding, H. H. *The Journal of Physical Chemistry A* **2019**, *123*, 2709–2718.

(24) Hart, E. J.; Boag, J. W. *Journal of the American Chemical Society* **1962**, *84*, 4090–4095.

(25) Lübcke, A.; Buchner, F.; Heine, N.; Hertel, I. V.; Schultz, T. *Physical Chemistry Chemical Physics* **2010**, *12*, 14629–14634.

(26) Luckhaus, D.; Yamamoto, Y.-i.; Suzuki, T.; Signorell, R. *Science advances* **2017**, *3*, e1603224.

(27) Iglev, H.; Trifonov, A.; Thaller, A.; Buchvarov, I.; Fiebig, T.; Laubereau, A. *Chemical physics letters* **2005**, *403*, 198–204.

(28) Kimura, Y.; Alfano, J. C.; Walhout, P.; Barbara, P. F. *The Journal of Physical Chemistry* **1994**, *98*, 3450–3458.

(29) Silva, C.; Walhout, P. K.; Yokoyama, K.; Barbara, P. F. *Physical review letters* **1998**, *80*, 1086.

(30) Maiuri, M.; Garavelli, M.; Cerullo, G. *Journal of the American Chemical Society* **2019**, *142*, 3–15.

(31) Berera, R.; van Grondelle, R.; Kennis, J. T. *Photosynthesis research* **2009**, *101*, 105–118.

(32) Lorenc, M.; Ziolek, M.; Naskrecki, R.; Karolczak, J.; Kubicki, J.; Maciejewski, A. *Applied Physics B* **2002**, *74*, 19–27.

(33) Atkins, P. W.; De Paula, J.; Keeler, J., *Atkins' physical chemistry*; Oxford university press: 2023.

(34) Faubel, M.; Steiner, B.; Toennies, J. P. *The Journal of chemical physics* **1997**, *106*, 9013–9031.

(35) Faubel, M.; Schlemmer, S.; Toennies, J. *Zeitschrift für Physik D Atoms, Molecules and Clusters* **1988**, *10*, 269–277.

(36) Faubel, M.; Steiner, B. *Berichte der Bunsengesellschaft für physikalische Chemie* **1992**, *96*, 1167–1172.

(37) Winter, B.; Faubel, M. *Chemical reviews* **2006**, *106*, 1176–1211.

(38) Shreve, A. T.; Yen, T. A.; Neumark, D. M. *Chemical Physics Letters* **2010**, *493*, 216–219.

(39) Perry, C. F.; Zhang, P.; Nunes, F. B.; Jordan, I.; von Conta, A.; Wörner, H. J. *The journal of physical chemistry letters* **2020**, *11*, 1789–1794.

(40) Hummert, J.; Reitsma, G.; Mayer, N.; Ikonnikov, E.; Eckstein, M.; Kornilov, O. *The Journal of Physical Chemistry Letters* **2018**, *9*, 6649–6655.

(41) Tau, O.; Henley, A.; Boichenko, A. N.; Kleshchina, N. N.; Riley, R.; Wang, B.; Winning, D.; Lewin, R.; Parkin, I. P.; Ward, J. M., et al. *Nature communications* **2022**, *13*, 507.

(42) Fortune, W. G.; Scholz, M. S.; Fielding, H. H. *Accounts of Chemical Research* **2022**, *55*, 3631–3640.

(43) Koopmans, T. *physica* **1934**, *1*, 104–113.

(44) Rosspeintner, A.; Lang, B.; Vauthey, E. *Annual review of physical chemistry* **2013**, *64*, 247–271.

(45) Bagchi, B., *Water in biological and chemical processes: from structure and dynamics to function*; Cambridge University Press: 2013.

(46) Carpenter, B. K.; Harvey, J. N.; Orr-Ewing, A. J. *Journal of the American Chemical Society* **2016**, *138*, 4695–4705.

(47) Orr-Ewing, A. J. *Chemical Society Reviews* **2017**, *46*, 7597–7614.

(48) Ottosson, N.; Faubel, M.; Bradforth, S. E.; Jungwirth, P.; Winter, B. *Journal of Electron Spectroscopy and Related Phenomena* **2010**, *177*, 60–70.

(49) Nishitani, J.; Yamamoto, Y.-i.; West, C. W.; Karashima, S.; Suzuki, T. *Science Advances* **2019**, *5*, eaaw6896.

(50) Signorell, R. *The journal of physical chemistry letters* **2020**, *11*, 1516–1519.

(51) Signorell, R.; Goldmann, M.; Yoder, B. L.; Bodi, A.; Chasovskikh, E.; Lang, L.; Luckhaus, D. *Chemical Physics Letters* **2016**, *658*, 1–6.

(52) Hara, A.; Yamamoto, Y.-i.; Suzuki, T. *The Journal of Chemical Physics* **2019**, *151*.

(53) Yamamoto, Y.-i.; Suzuki, T. *The Journal of Physical Chemistry Letters* **2020**, *11*, 5510–5516.

(54) Scholz, M. S.; Fortune, W. G.; Tau, O.; Fielding, H. H. *The Journal of Physical Chemistry Letters* **2022**, *13*, 6889–6895.

(55) Kovalenko, S. A.; Dobryakov, A. L.; Ruthmann, J.; Ernsting, N. P. *Physical review A* **1999**, *59*, 2369.

(56) Kovalenko, S. A.; Ernsting, N. P.; Ruthmann, J. *Chemical physics letters* **1996**, *258*, 445–454.

(57) Snellenburg, J. J.; Laptenok, S.; Seger, R.; Mullen, K. M.; van Stokkum, I. H. *Journal of Statistical Software* **2012**, *49*, 1–22.

(58) Van Stokkum, I. H.; Weißenborn, J.; Weigand, S.; Snellenburg, J. J. *Photochemical & Photobiological Sciences* **2023**, *22*, 2413–2431.

(59) Grubb, M. P.; Orr-Ewing, A. J.; Ashfold, M. N. *Review of Scientific Instruments* **2014**, *85*.

(60) Riley, J. W.; Wang, B.; Parkes, M. A.; Fielding, H. H. *Review of Scientific Instruments* **2019**, *90*.

(61) Nishitani, J.; Karashima, S.; West, C. W.; Suzuki, T. *The Journal of chemical physics* **2020**, *152*.

(62) Seidel, R.; Thurmer, S.; Winter, B. *The Journal of Physical Chemistry Letters* **2011**, *2*, 633–641.

(63) Jarvis, G.; Evans, M.; Ng, C.; Mitsuke, K. *The Journal of chemical physics* **1999**, *111*, 3058–3069.

(64) Sansonetti, J. E.; Martin, W. C. *Journal of physical and chemical reference data* **2005**, *34*, 1559–2259.

(65) Kurahashi, N.; Karashima, S.; Tang, Y.; Horio, T.; Abulimiti, B.; Suzuki, Y.-I.; Ogi, Y.; Oura, M.; Suzuki, T. *The Journal of chemical physics* **2014**, *140*.

(66) Preissler, N.; Buchner, F.; Schultz, T.; Lübcke, A. *The Journal of Physical Chemistry B* **2013**, *117*, 2422–2428.

(67) Mala, G. M.; Li, D.; Werner, C.; Jacobasch, H.-J.; Ning, Y. *International journal of heat and fluid flow* **1997**, *18*, 489–496.

(68) Stemer, D.; Buttersack, T.; Haak, H.; Malerz, S.; Schewe, H. C.; Trinter, F.; Mudryk, K.; Pugini, M.; Credidio, B.; Seidel, R., et al. *The Journal of Chemical Physics* **2023**, *158*.

(69) Credidio, B.; Pugini, M.; Malerz, S.; Trinter, F.; Hergenhahn, U.; Wilkinson, I.; Thürmer, S.; Winter, B. *Physical Chemistry Chemical Physics* **2022**, *24*, 1310–1325.

(70) He, Z.; Martin, C. H.; Birge, R.; Freed, K. F. *The Journal of Physical Chemistry A* **2000**, *104*, 2939–2952.

(71) Van Thor, J. J. *Chemical Society Reviews* **2009**, *38*, 2935–2950.

(72) Acharya, A.; Bogdanov, A. M.; Grigorenko, B. L.; Bravaya, K. B.; Nemukhin, A. V.; Lukyanov, K. A.; Krylov, A. I. *Chemical Reviews* **2017**, *117*, 758–795.

(73) Yamamoto, Y.-i.; Karashima, S.; Adachi, S.; Suzuki, T. *The Journal of Physical Chemistry A* **2016**, *120*, 1153–1159.

(74) Riley, J. W.; Wang, B.; Woodhouse, J. L.; Assmann, M.; Worth, G. A.; Fielding, H. H. *The Journal of Physical Chemistry Letters* **2018**, *9*, 678–682.

(75) Oliver, T. A.; Zhang, Y.; Roy, A.; Ashfold, M. N.; Bradforth, S. E. *The Journal of Physical Chemistry Letters* **2015**, *6*, 4159–4164.

(76) Rayne, S.; Forest, K.; Friesen, K. J. *Environment international* **2009**, *35*, 425–437.

(77) Mialocq, J.-C.; Sutton, J.; Goujon, P. *The Journal of Chemical Physics* **1980**, *72*, 6338–6345.

(78) Chen, X.; Larsen, D. S.; Bradforth, S. E.; van Stokkum, I. H. *The Journal of Physical Chemistry A* **2011**, *115*, 3807–3819.

(79) Tyson, A. L.; Verlet, J. R. *The Journal of Physical Chemistry B* **2019**, *123*, 2373–2379.

(80) Robertson, K.; Fortune, W. G.; Davies, J. A.; Boichenko, A. N.; Scholz, M. S.; Tau, O.; Bochenkova, A. V.; Fielding, H. H. *Chemical Science* **2023**, *14*, 3257–3264.

(81) Goldschmidt, C. R.; Stein, G. *Chemical Physics Letters* **1970**, *6*, 299–303.

(82) Boichenko, A. N.; Bochenkova, A. V. *Journal of Chemical Theory and Computation* **2023**, *19*, 4088–4099.

(83) Baylin, S. B.; Jones, P. A. *Nature Reviews Cancer* **2011**, *11*, 726–734.

(84) Martinez-Fernandez, L.; Banyasz, A.; Esposito, L.; Markovitsi, D.; Improta, R. *Signal Transduction and Targeted Therapy* **2017**, *2*, 1–7.

(85) Robertson, K. D.; A. Jones, P. *Carcinogenesis* **2000**, *21*, 461–467.

(86) Cannistraro, V. J.; Taylor, J.-S. *Journal of molecular biology* **2009**, *392*, 1145–1157.

(87) Malone, R. J.; Miller, A. M.; Kohler, B. *Photochemistry and photobiology* **2003**, *77*, 158–164.

(88) Ma, C.; Cheng, C. C.-W.; Chan, C. T.-L.; Chan, R. C.-T.; Kwok, W.-M. *Physical Chemistry Chemical Physics* **2015**, *17*, 19045–19057.

(89) Davies, A. R.; Kemp, D. J.; Wright, T. G. *AIP Advances* **2020**, *10*.

(90) Nesbitt, D. J.; Field, R. W. *The Journal of Physical Chemistry* **1996**, *100*, 12735–12756.

(91) Roberts, G.; Stavros, V.; de Balda, R.; Bañares, L. **2014**.

(92) Timbers, P. J.; Parmenter, C. S.; Moss, D. B. *The Journal of chemical physics* **1994**, *100*, 1028–1034.

(93) Feitelson, J.; Hayon, E.; Treinin, A. *Journal of the American Chemical Society* **1973**, *95*, 1025–1029.

(94) Ichino, T., *On the mechanism of unusual CIDEP*; University of Notre Dame: 2001.

(95) Alfano, J. C.; Walhout, P.; Kimura, Y.; Barbara, P. F. *The Journal of chemical physics* **1993**, *98*, 5996–5998.

(96) Jordan, C. J.; Coons, M. P.; Herbert, J. M.; Verlet, J. R. *nature communications* **2024**, *15*, 182.

(97) Jordan, C. J. Ultrafast dynamics at aqueous-air interfaces, Ph.D. Thesis, Durham University, 2023.

(98) Buchner, F.; Schultz, T.; Lübcke, A. *Physical Chemistry Chemical Physics* **2012**, *14*, 5837–5842.

(99) Tang, Y.; Shen, H.; Sekiguchi, K.; Kurahashi, N.; Mizuno, T.; Suzuki, Y.-I.; Suzuki, T. *Physical Chemistry Chemical Physics* **2010**, *12*, 3653–3655.

(100) Kumar, G.; Roy, A.; McMullen, R. S.; Kutagulla, S.; Bradforth, S. E. *Faraday discussions* **2018**, *212*, 359–381.

(101) Gosset, P.; Taupier, G.; Cregut, O.; Brazard, J.; Mely, Y.; Dorkenoo, K.-D.; Leonard, J.; Didier, P. *J. Phys. Chem. Lett.* **2020**, *11*, 3653–3659.

(102) Li, S.; Ruan, Z.; Zhang, H.; Xu, H. *European Journal of Medicinal Chemistry* **2021**, *211*, 113111.

(103) Ghose, A.; Rebarz, M.; Maltsev, O. V.; Hintermann, L.; Ruckebusch, C.; Fron, E.; Hofkens, J.; Mély, Y.; Naumov, P.; Sliwa, M., et al. *The Journal of Physical Chemistry B* **2015**, *119*, 2638–2649.

(104) Patel, A. M.; Henley, A.; Parkes, M. A.; Assmann, M.; Worth, G. A.; Anderson, J. C.; Fielding, H. H. *Physical Chemistry Chemical Physics* **2020**, *22*, 19022–19032.

(105) Ugarova, N.; Brovko, L. Y. *Luminescence: the journal of biological and chemical luminescence* **2002**, *17*, 321–330.

(106) Shimomura, O. Bioluminescence: Chemical principles and applications, 2008.

(107) Meech, S. R. *Chemical Society Reviews* **2009**, *38*, 2922–2934.

(108) Woodhouse, J. L.; Assmann, M.; Parkes, M. A.; Grounds, H.; Pacman, S. J.; Anderson, J. C.; Worth, G. A.; Fielding, H. H. *Physical Chemistry Chemical Physics* **2017**, *19*, 22711–22720.

(109) Naumov, P.; Kochunnoonny, M. *Journal of the American Chemical Society* **2010**, *132*, 11566–11579.

(110) Solntsev, K. M.; Laptenok, S. P.; Naumov, P. *Journal of the American Chemical Society* **2012**, *134*, 16452–16455.

(111) Anderson, J. C.; Grounds, H.; Jathoul, A. P.; Murray, J. A.; Pacman, S. J.; Tisi, L. *RSC advances* **2017**, *7*, 3975–3982.

(112) Weissleder, R. *Nature biotechnology* **2001**, *19*, 316–317.

(113) Rice, B. W.; Cable, M. D.; Nelson, M. B. *Journal of biomedical optics* **2001**, *6*, 432–440.

(114) Seliger, H.; McElroy, W. *Proceedings of the National Academy of Sciences* **1964**, *52*, 75–81.

(115) Ohmiya, Y. *Japanese journal of applied physics* **2005**, *44*, 6368.

(116) Podsiadły, R.; Grzelakowska, A.; Modrzejewska, J.; Siarkiewicz, P.; Słowiński, D.; Szala, M.; Świerczyńska, M. *Dyes and Pigments* **2019**, *170*, 107627.

(117) Støchkel, K.; Hansen, C. N.; Houmøller, J.; Nielsen, L. M.; Anggara, K.; Linares, M.; Norman, P.; Nogueira, F.; Maltsev, O. V.; Hintermann, L., et al. *Journal of the American Chemical Society* **2013**, *135*, 6485–6493.

(118) Presiado, I.; Erez, Y.; Simkovitch, R.; Shomer, S.; Gepshtein, R.; Pinto da Silva, L.; Esteves da Silva, J. C.; Huppert, D. *The Journal of Physical Chemistry A* **2012**, *116*, 10770–10779.

(119) Cherednikova, E. Y.; Chikishev, A. Y.; Ol'ga, V. K.; Mizuno, M.; Sakai, M.; Takahashi, H. *Chemical physics letters* **1999**, *308*, 369–372.

(120) Branchini, B. R.; Murtiashaw, M. H.; Magyar, R. A.; Portier, N. C.; Ruggiero, M. C.; Stroh, J. G. *Journal of the American Chemical Society* **2002**, *124*, 2112–2113.

(121) Navizet, I.; Liu, Y.-J.; Ferré, N.; Xiao, H.-Y.; Fang, W.-H.; Lindh, R. *Journal of the American Chemical Society* **2010**, *132*, 706–712.

(122) Veys, K.; Escudero, D. *Accounts of Chemical Research* **2022**, *55*, 2698–2707.

(123) Viswanath, G.; Kasha, M. *The Journal of Chemical Physics* **1956**, *24*, 574–577.